Neuromorphic properties of Mott materials under an electric field

Rodolfo Rocco

université
PARIS-SACLAY

Neuromoprhic properties of Mott materials under an electric field

Propriétés neuromorphiques des materiaux de Mott sous un champ électrique

Thèse de doctorat de l'Université Paris-Saclay

École doctorale n° 546, Physique en Île-de-France (PIF)
Spécialité de doctorat : Physique
Graduate School : Physique, Référent : Faculté des sciences d'Orsay

Thèse préparée dans l'unité de recherche **Laboratoire de Physique des Solides (Université Paris-Saclay, CNRS)** , sous la direction de **Prof. Marcelo Rozenberg**

Thèse présentée et soutenue à Paris-Saclay, le 16 decembre 2022, par

Rodolfo ROCCO

Composition du jury

Marino Marsi Full professor, Laboratoire de physique des solides Université Paris-Saclay, CNRS	Président de jury
María José Sánchez Principal researcher, Institute of Nanoscience and Nanotechnology National Research Council (CONICET)	Rapportrice et examinatrice
Dirk Wouters Senior Researcher, Institute of Electronic Materials RWTH Aachen University	Rapporteur et examinateur
Laurent Cario Directeur de recherche, Institut des matériaux de Nantes Jean Rouxel Université de Nantes, CNRS	Examinateur
Isao H. Inoue Chief Senior Researcher, National Institute of Advanced Industrial Science and Technology (AIST)	Examinateur
Damien Querlioz Researcher, Centre de Nanosciences et de Nanotechnologies Université Paris-Saclay, CNRS	Examinateur
Marcelo Rozenberg Professor, Laboratoire de physique des solides Université Paris-Saclay, CNRS	Directeur de thèse

Thèse de doctorat

NNT : 2022UPASP137

Aknowledgments

This work was done in collaboration with several experimental groups whose expertise and knowledge has bee invaluable in shaping the research that is presented in this thesis. In particular I would like to thank everyone who is involved in the QMEENC joint effort, and specifically the group of Ivan Schuller from the University of San Diego California, for providing the samples on which our collaborators were able to conduct their experiments. I would also like to extend my thanks to Coline Adda and Erbin Qiu, also from USD, for their experimental work on the oscillating V3O5 system, and the coupled VO2 system respectively. Finally, I would like to thank the group of Javier del Valle at the University of Geneva for their work on the switching time of the resistive collapse in the vanadates and the nickelates, which was instrumental in understanding the stochastic nature of metallic filament percolation in Mott materials under an applied voltage, which constitutes one of the main results of this work. At last, but definitely not least, I would like to warmly thank my supervisor, Marcelo, for providing me with ample opportunities to conduct research and being extremely supportive throughout the PhD, and in particular during the covid-19 pandemic.

Dedication

This work is dedicated to my parents, Federico and Daniela, who have taught me what I needed to know to get where I wanted to be.

Table des matières

Chapitre 1

Introduction

1.1 Résumé

Aujourd'hui il y a une forte demande de dispositifs intelligentes capables d'achever des tâches cognitives compliqués, comme, par exemple, la classification des images ou des signes visuelles. Depuis les premiers jours de l'informatique, les réseaux de neurones ont été établies comme le modelé mathématique de calcul le plus approprié à réaliser l'intelligence artificielle[MP43][Ros58][RJP19], une position consolidée par le succès récent des réseaux de neurones profondes («deep neural networks»)[RJP19]. D'habitude, les réseaux de neurones sont implémentés par des simulations numériques qui sont élaborés par un ordinateur [RJP19]. Cette solution a l'avantage de compter sur la très bien connue technologie CMOS («complementary metal-oxide semiconductor») ; toutefois, la consommation d'énergie est bien loin de s'approcher à l'efficience du cerveau humain[CD14]. Ce fait a instigué les développements de solutions alternatives, comme des ordinateurs qui ne suivent pas l'architecture de Von Neumann [Tha+18]et, plus récemment, des systèmes neuromorphique qui utilisent des matériaux quantiques [Del+18]. Ces matériaux pourraient atteindre un niveau de miniaturisation plus haut de celui de la technologie CMOS, ce qui leur rendrait plus efficientes du point de vue énergique. Néanmoins, la caractérisation de ces matériaux pose des difficultés importantes dues à la complexité des phénomènes physique qui sont à la base de leur propriétés neuromorphiques.

Les isolants de Mott sont une des familles des matériaux quantiques qui présentent des caractéristiques neuromorphiques[Sto+17 ; Add+18]. Elles sont rendues possibles par la transition isolant-métal (IMT) [IFT98 ; Geo+96] qui se produit sous certaines conditions, notamment l'application d'un champ électrique[Die+18]. L'application du champ électrique cause la formation de filaments métalliques dans le matériel, qui connectent les électrodes, en provocant la chute de la résistance

et en même temps l'élévation de la courent électrique. Cet incrément rapide de la courent est fondamentale pour reproduire le mécanisme de production du potentiel d'action (ou «spike» en anglais) qui permet aux neurones biologiques de communiquer. Une caractéristique notable, qui est également importante pour la production du potentiel d'action, est la volatilité du collapse de la résistance ; autrement dit, quand le champ électrique est éteint, la résistance s'élève au niveau isolant original[Jan+15]. Cette caractéristique permet de réaliser la chute du potentiel de la membrane du neurone qui suive la dépolarisation, après laquelle le neurone atteint l'état de repos et devient prêt à produire un niveau potentiel d'action. Sans cette descente du potentiel le neurone resterait dans son état excité et serait insensible à la stimulation suivante. Le neurone réalisé par les matériaux de Mott (aussi dit neurone de Mott) ne nécessite pas d'autre éléments électroniques, et notamment de condensateurs, et c'est pour ça qu'il pourrait être possible de les miniaturiser plus que les dispositifs CMOS.

Néanmoins, la IMT sous un champ électrique est un phénomène physique très compliqué, qui est causé par l'interaction entre beaucoup des électrons sous un fort champ électrique[IFT98 ; Geo+96], et il pose des difficultés à la caractérisation de ces matériaux, et donc leur application. Dans cette thèse nous attaquons ces difficultés en utilisant un modèle phénoménologique qui s'appelle Mott Resistor Network (réseau des résistors de Mott)[Sto+14 ; Sto+13]. Ce modèle nous permet d'investiguer le collapse de la résistance avec une résolution temporelle majeure de cela des instrumentes expérimentales et en même temps d'éviter la complexité de calcul des descriptions mathématiques microscopiques. En utilisant ce modèle nous arrivons à comprendre la chute de la résistance sous un champ électrique comme un phénomène intrinsèquement stochastique qui est affecté par des contributions et électrique et thermique. En plus, nous lions la nature stochastique du collapse de la résistance avec la rumeur («noise») du mécanisme de production des potentiels d'actions des certaines modèles mathématiques des neurones [Ger+14], en montrant que le deux partagent la même distribution de probabilité et peuvent être compris comme des évènements de Poisson[Roc+22]. Ce résultat est important puisqu'il démontre que la résistance de matériaux de Mott sous un champ électrique externe collapse avec la même probabilité avec laquelle le neurone biologique produit les potentiels d'actions, et donc ces matériaux pourraient être employés pour implémenter des réseaux des neurones plausibles du point de vue biologique.

Un autre résultat de notre travail c'est clarifier comment les caractéristiques physiques d'un certain matériel, comme, par exemple, la résistivité ou la conductivité thermique, peuvent affecter le période d'incubation et l'augmentation des dimensions du domaine métallique à l'intérieur du matériel isolant qui provoque le collapse de la résistance[Roc+22 ; Val+21 ; Del+21]. En particulier, nous montrons que, en augmentant la conductivité thermique et donc la dissipation vers le

substrat, nous achevons une transition plus inhomogène, caractérisée par des gradients de température plus forts, des domaines métalliques qui sont plus chaudes et mince (similaires à des filaments), et aussi une dépendance plus forte des temps d'incubation des domaines métalliques à l'intensité du champ électrique externe. Après, nous montrons que des résultats similaires peuvent être obtenues en utilisant la résistivité isolant comme paramètre de contrôle, au lieu de la conductivité thermique. Ça nous permet d'expliquer les différences observées entre le Vanadium Dioxide (VO2) et le Divanadium Trioxide (V2O3) dans les expérimentes. En fait, le V2O3 présent un rapport entre le résistivité isolant et métallique majeur que celui du VO2 et aussi une transition plus inhomogène, avec une dépendance plus forte des temps d'incubation à l'intensité du champ électrique. Nous étudions aussi l'augmentation des dimensions du domaine métallique après le collapse de la résistance, et nous trouvons qu'elle est de nature exponentielle, et qualitativement comparable aux observations expérimentales effectués à partir de la réflectivité optique du VO2[Del+21].

Le VO2 est un cas d'étude particulièrement intéressant car il présent une collapse de la résistance à températures comparables à la température ambiante, donc il est bien adapté pour les applications pratiques. La généralité du Réseau des Résistors de Mott est telle que le modèle peut être appliqué non seulement à les vanadates comme VO2 et V2O3 mais aussi à autres matériaux comme les nickelates. Par conséquence nous développons ultérieurement le MRN afin de modéliser deux matériaux qui font partie de la famille de nickelates : Samarium nickelate (SmNiO3) et neodymiumu nickelate (NdNiO3)[Val+21]. Nous trouvons que pour ces matériaux aussi il est possible provoquer une transition inhomogène si on augmente le rapport entre la résistivité isolant et métallique, comme c'était le cas pour les vanadates. Ce résultat nous permet d'expliquer pourquoi on observe une dépendance des temps d'incubation à l'intensité du champ électrique plus forte pour NdNiO3 que pour SmNiO3, similairement aux cas du V2O3 contre le VO2. En outre, nous montrons comment on peut exploiter la dépendance de la résistivité isolant à la température pour provoquer une transition plus inhomogène en abaissant la température du substrat. Ces observations sont confirmées par expérimentes conduites sur des exemplaires de NdNiO3 et SmNiO3, qui démontrent qu'une température du substrat plus bas cause une transition plus abrupt à champs électrique faibles.

Une autre questionne que nous considérons est la possibilité de provoquer des oscillations dans les neurones de Mott. Des oscillations sont observées dans les neurones singles, dans les populations de neurones et aussi au niveau macroscopique dans l'encéphalogramme[Ger+14 ; Pey+12 ; War03 ; Don+98]. Par conséquence c'est important que les neurones de Mott puissent être identifiés comme des oscillateurs neuronales. Pour cette raison nous étudions un système composé

par un exemplaire de Trivanadium Pentoxide (V3O5) en parallèle avec un condensateur. A' cette fin nous développons le MRN pour introduire la capacitance du circuit et aussi la transition de second ordre qui caractérise le V3O5, en contraste avec le VO2 et le V2O3 qui sont caractérisés par une transition de premier ordre. En étudiant la courbe IV et les mappes de la résistivité produites par le modèle sous une rampe de tension nous observons un régime oscillant, qui émerge après la chute de la résistance et disparait quand le stimulus devient trop haut, et qui dérive de l'interaction entre le V3O5 et le condensateur. Après peu le début du collapse de la résistance, le condensateur commence à décharger, le voltage s'abaisse et une courent électrique passe du condensateur au matériel, en réchauffant le domaine métallique. À fur et à mesure que le condensateur se déplète, la courent commence à s'abaisser et devient trop basse pour soutenir les filaments métalliques, qui lentement se relaxent dans l'état isolant. Pendant que la résistance du matériel s'élève, la courent électrique appliquée re-entre dans le condensateur vidé, en le chargeant et élevant le voltage. Le voltage, en s'élevant, réchauffe le matériel, qui maintenant se trouve dans l'état isolant, et cause une nouvelle chute de la résistance. Le régime oscillatoire termine quand le voltage appliqué est si haut que le condensateur charge trop vite pour que le filament ait le temp de redevenir isolant, ainsi l'état métallique se stabilise. Nous comparons nos resultats avec les images produites par la réflectivité optique d'un exemplaire expérimental de V3O5[Add+22], et aussi les mesures de curent électrique dans le régime oscillant, en trouvant que les expérimentes supportent notre analyse.

Finalement, nous considérons un système de deux exemplaires de VO2 couplés par un condensateur, chacun caractérisé par sa propre capacitance et son régime stochastique. Ce système nous permet d'investiguer d'une façon plus approfondie le régime stochastique et oscillatoire qui avait été déjà observé. En plus, exemplaires de VO2 couplés pourraient être appliqués dans le domaine du calcul oscillatoire et pourraient être utilisés pour résoudre une variété des problèmes de nature combinatoire, en consumant mois d'énergie que les solutions CMOS traditionnelles[CP20 ; Mal+20 ; Dut+21 ; Ahm+21]. Par conséquence, leur caractérisation est une étape importante vers la réalisation du calcul efficient du point de vue énergétique. Pour achever cet objective, nous développons un modèle numérique qui utilise la distribution de probabilité de percolation des filaments que nous avons dérivée avant pour prédire les temps de génération («timings») des potentiels d'action de deux oscillateurs VO2. En première lieu, nous étudions le cas dans lequel la capacité de couplage est nulle et les deux exemplaires oscillent indépendants. Après, nous connectons les oscillateurs en utilisant le condensateur de couplage, qui a l'effet de synchroniser les oscillateurs, lesquelles maintenant génèrent un potentiel d'action l'un après l'autre, à tour de rôle. Toutefois, en incrémentant la capacitance de couplage, disruptions dans la séquence des «spikes» émergent ; autrement dit, deux ou

plus «spikes» consécutives sont générés par le même oscillateur. Ces disruptions peuvent être observés dans les mesures de curent qui sort des oscillateurs et aussi dans leur distribution des intervalles entre spikes («Inter-Spike Intervals», ISI), qui est similaire à la distribution de Poisson sans le condensateur mais devient multimodale à fur et à mesure que la capacitance de couplage est augmentée. Nous expliquons les disruptions comme un effet de la décharge de voltage des oscillateurs qui se produit quand un des oscillateurs génèrent un potentiel d'action. La décharge est proportionnelle à la capacité de couplage, ainsi une haute capacitance produit une décharge complète dans les deux oscillateurs, dont le voltage devient nul. Par conséquence, l'exemplaire qui a une probabilité intrinsèque de générer le potentiel d'action plus haute reste toujours le favori dans le cas d'une décharge complet. Nous comparons nos resultats avec des expérimentés dans lesquelles un système de deux VO2 couplés a été étudié[Qiu+], en trouvant un accord qualitatif.

1.2 Summary

In today's world there is an increasing demand for smart devices capable of executing complex cognitive tasks, such as pattern recognition and classification. From the early days of digital computing, neural networks have established themselves as the computational paradigm best suited for realizing machine intelligence [MP43][Ros58][RJP19], a position consolidated by the recent success of deep neural networks[KSH12]. Traditionally, neural networks are implemented in the form of a software simulation running on a digital computer [RJP19]. While this approach has the advantage of relying on the well-known Complementary Metal Oxide Semiconductor (CMOS) technology, power consumption is far away from approaching the efficiency of the human brain [CD14], which has prompted the investigation of alternative solutions, such as computers that deviate from the Von Neumann architecture [Tha+18] and, more recently, neuromorphic systems based on quantum materials[Del+18]. These materials could be miniaturized beyond the limits of CMOS technology, resulting in improved power efficiency ; however, their characterization pose important challenges due to the complexity of the underlying physical phenomena that grant them their unique neuromorphic features.

Mott insulators are one such class of materials presenting neuromorphic characteristics [Sto+17 ; Add+18]. These are enabled by the Insulator to Metal Transition (IMT) [IFT98 ; Geo+96], which occurs in Mott materials under certain conditions, for example when an electric field [Die+18] is applied. The application of the electric field induces the formation of metallic filaments within the insulating bulk of the material, which percolate and short-circuit the electrodes, resulting in the collapse of the resistance by several orders of magnitude and an equal surge of the current through the sample. This surge in current is key to implementing the spi-

king mechanism through which biological neurons communicate with one another. One notable characteristic of the resistive collapse, which is just as important for the correct implementation of the spiking functionality, is its volatile nature, that is to say, when the applied voltage is turned off, the material cools down and the resistance resumes its original insulating value [Jan+15]. This allows to implement the decay that follows the rapid depolarization of the neuronal membrane potential, after which the neuron recovers its resting state and is ready to fire again. Without this decay, the neuron would remain in its excited state and would not be susceptible to further stimulation. The spiking functionality of Mott neurons does not rely on external circuit elements, most notably capacitors, for which reason it should be possible to miniaturize these devices beyond the limits of conventional CMOS chips.

However, the complex nature of the field driven IMT, which is a physical phenomenon that stems from the interaction of many correlated electrons under a strong electric field [IFT98 ; Geo+96], poses several challenges to the characterization of these materials, and therefore their application. In this work we tackle these challenges primarily by using a phenomenological model known as the Mott Resistor Network (MRN) [Sto+14 ; Sto+13]. This model allows us to investigate the resistive collapse with a temporal resolution greater than that of the experiments, while also avoiding the mathematical complexity of more microscopic descriptions. In doing so, we are able to understand resistive switching as an intrinsically stochastic phenomenon that is affected by both electronic and thermal contributions, thus shedding a light on the much debated topic of the nature of the field driven transition in Mott materials. Additionally, we link the stochasticity of the resistive collapse to the noisy firing of neuronal models with an exponential escape rate [Ger+14], by showing that they share the same probability distribution, and that both can be understood as Poisson processes [Roc+22]. This is an important result in that it shows that Mott materials under an applied voltage spike with the same stochastic behavior of biological neurons, and are therefore suitable for implementing biologically plausible neural networks.

Another contribution of our work is clarifying how the different characteristics of a given sample, such as its resistivity and thermal conductivity, can affect the incubation period leading up to the collapse of the resistance as well as the growth of the metallic domain after the collapse [Roc+22 ; Val+21 ; Del+21]. In particular we show that, by increasing the thermal conductivity and thus the dissipation to the substrate, we can achieve more inhomogenous transitions, characterized by stronger temperature gradients, thinner and hotter metallic domains, as well as a sharper dependence of the incubation time of the resistive collapse on the applied voltage. Then we go on to show that similar results can be achieved by using the insulating resistivity as a control parameter, instead of the thermal conductivity.

This allows us to make sense of the differences observed experimentally between Vanadium Dioxide (VO2) and Divanadium Trioxide (V2O3), the latter of which presents a higher ratio of the insulating to metallic resistivity and a comparatively inhomogenous transition, with a steeper dependence of the incubation times on the applied voltage. We also study the expansion of the metallic domain after the collapse of the resistance, finding that it is exponential in time, and qualitatively in agreement with optical reflectivity experiments conducted on VO2 [Del+21].

VO2 is a particularly interesting case study in that it presents resistive switching close to room temperature, and therefore is well suited for practical applications. The generality of the MRN makes it a good model not only of the vanadates like VO2 and V2O3, but also for other materials such as the nickelates. Therefore, we go on to expand the MRN in order to model two members of the nickelates family : Samarium Nickelate (SmNiO3) and Neodymium Nickelate (NdNiO3) [Val+21]. In these materials too we find that it is possible to induce a more inhomogenous transition by increasing the resistivity ratio, as previously observed for the vanadium oxides. This allows us to explain why we observe a stronger dependence of the incubation time on the applied voltage in NdNiO3 than SmNiO3, in analogy with the V2O3 versus VO2 comparison. Moreover, we show how a strong dependence of the insulating resistivity on the temperature can be exploited to induce a more inhomogenous transition by lowering the substrate temperature. This observation finds confirmation in experiments conducted on both NdNiO3 and SmNiO3, in which it is found that lower substrate temperatures result in a more abrupt switching mechanism at low applied voltages in both materials.

Another question that we tackle is whether it is possible to induce oscillation in Mott neurons. Oscillatory behaviours are observed in single neurons, in population dynamics and also at the macroscopic level in Electro Enecephalo Graph (EEG) recordings [Ger+14 ; Pey+12 ; War03 ; Don+98]. It is therefore of the utmost interest that Mott neurons should act as neural oscillators. For this reason we decided to study a system made of a Trivanadium Pentoxide (V3O5) sample in parallel to a capacitor. To do so we expanded the MRN model to account for the capacitance of the circuit, as well as the second order transition presented by V3O5, in contrast to VO2 and V2O3 which have a first order transition. By studying the IV curve and the resistivity maps of the model under a ramp voltage we were able to observe an oscillatory regime, which emerges after the resistive collapse and eventually dies out when the stimulus becomes too high, and were able to understand it as an effect of the interaction between V3O5 material and the capacitor. At the onset of the resistive collapse, the capacitor begins to discharge, the voltage goes down and an electric current flows from the capacitor into the sample, further heating up its metallic domain. Eventually, as the capacitor approaches depletion, this current starts decreasing and becomes insufficient to sustain the hot metallic filament,

which gradually relaxes back to the insulating state. While the resistance of the sample goes up, the applied current flows to the depleted capacitor, charging it back and raising the voltage. The increasing voltage heats up the sample, which by now is fully insulating, and triggers a new resistive collapse. The oscillatory regime ends when the applied voltage is so high that the capacitor charges too fast for the metallic domain to relax, thus stabilizing the metallic state. We compare our results with optical reflectivity images from V3O5 experiments [Add+22], as well as current measurements conducted in the oscillatory regime, finding that the experiments support and are in agreement with our analysis.

Finally, we consider a system of two VO2 samples coupled with a capacitor, each characterized by its own self capacitance and stochastic behaviour. This setup allows us to further investigate the stochasticity of Mott materials under an applied voltage and the previously observed oscillatory regime. Moreover, coupled VO2 oscillators may find application in the field of oscillatory computing [CP20 ; Mal+20 ; Dut+21 ; Ahm+21], and could be used to solve a variety of combinatorial tasks, while potentially consuming less power than traditional CMOS solutions. Therefore, their characterization is an important step towards the realization of energy-efficient computing. To this purpose, we developed a numerical model in which we use the probability distribution of filament percolation previously derived to predict the timings of the spikes generated by the two VO2 oscillators. Firstly we study the case in which the coupling capacitor is removed and the two devices oscillate independently. We then connect the oscillators using the capacitor, which has the effect of synchronizing the two devices, which now take turns in firing one after the other. However, as the coupling capacitance is increased, disruptions in the spike sequence appear, in the form of two or more consecutive spikes produced by the same device. These disruptions may be appreciated not only from the readings of the output current of the two devices, but also from the distribution of the Inter Spike Intervals (ISI) of the two devices, which is bell shaped in the absence of the capacitor, but becomes increasingly multimodal as the coupling capacitance is introduced and then increased. We understand the emergence of these disruptions as an effect of the discharge induced by the spiking device in the other device. The amount of the discharge is proportional to the coupling capacitance, thus a sufficiently big capacitance results in the almost complete discharge of the device that does not spike ; therefore, after the spike both devices begin to charge from a voltage value close to zero, and the one with the lower firing threshold will tend to win the race and fire again. We compare our findings with experiments in which a system of two coupled VO2 samples was studied [Qiu+], finding an excellent qualitative agreement.

1.3 Spiking Neurons

Biological neurons exchange information in the form of so called spikes [Maa97]. A spike is a sudden increase in the potential of the membrane of the neuronal cell, and is also known as action potential. The process of spike generation is very complex, and the resulting dynamics are very rich and varied [Ger+14] ; in the following we will only give the necessary information to understand the rest of this work. When a neuron receives a spike, its membrane depolarizes, that is, the membrane potential rises from its rest negative value. Such increase is gradual and proportional to the frequency of the input spikes ; however, once the potential has reached a certain threshold, it rapidly increases in a non-linear fashion, reaching positive values. This state is transient and thus the membrane immediately repolarizes and the potential decreases after it's reached its peak. If one looks at the graph of the potential (Figure 1.1) this transient state appears as a spike (hence its name) of the length of just a few milliseconds. At the end of the spike there is a period of hyper-polarization, called refractory period, during which the potential falls below its rest value an it is very hard or even impossible to elicit a new spike, no matter how strong the stimulus.

From a purely computational point of view, the shape of the spike and the trace of the potential are not important, since information is entirely encoded in the timing and the frequency of the emitted spikes, and the neuron is entirely characterized by the spikes history (also called spike train). In biological neurons spiking is a stochastic process, i.e. the timings of the spikes are not consistent across trials even under the same experimental conditions, a fact that can be modeled using a probabilistic threshold for firing[Jol+06 ; PG00 ; MS95]. This property can affect negatively the transmission of information, but there also cases in which stochasticity can be beneficial[MW11], for which reason it is important that it should be taken into account when implementing neuronal models.

1.4 Neuromorphic engineering

The field of neuromorphic engineering dates back to early days of modern computing, and specifically to the work of McCulloch and Pitts on Artificial Neural Network (ANN) [MP43]. Other important developments that followed were the invention of the perceptron [Ros58] (the first system capable of pattern recognition) by Rosenblatt in the fifties and of the cognitron (the first convolutional neural network) by Fukushima in the seventies [Fuk75]. After a period of declined interest, due to the recognition of certain inherent limitations of perceptron-like networks by Minsky [MP17], renewed interest arose in the 80s and 90s thanks to theoretical work of Maass [Maa94 ; Maa97], in which the computational com-

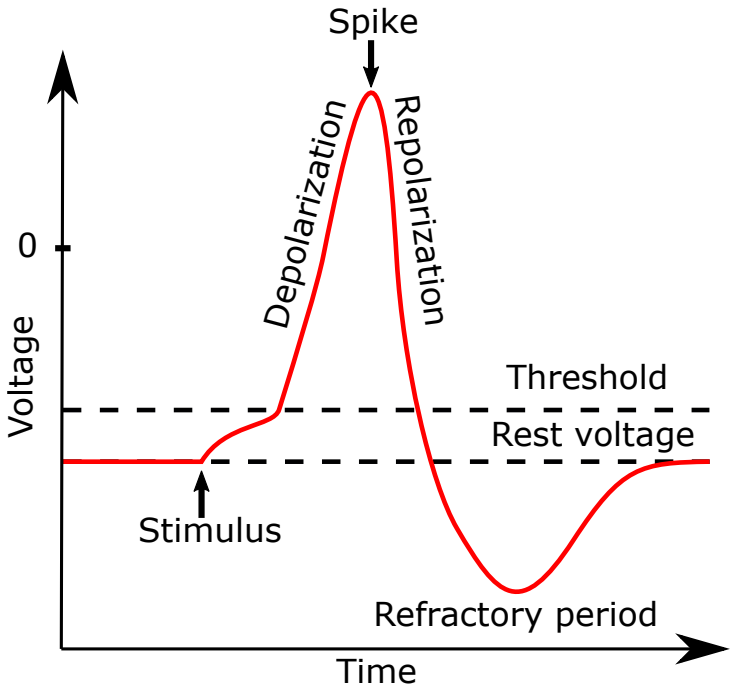

FIGURE 1.1 – Typical evolution of the potential of the membrane of a neuronal cell. If the stimulus is strong enough to push the potential above the threshold, the membrane rapidly depolarizes. The excited state does not last long, as the membrane repolarizes again, reaching its rest value after a period of hyper-polarization, known as refractory period, during which the neuron cannot be excited. Adapted from [CDt20].

plexity of spiking neurons was first established, and the engineering work of Mead, in which analog implementations of neural systems were demonstrated [Mea90 ; MM88 ; MI89]. Additionally, it was realized that the miniaturization process that had enabled the performance gains of traditional microprocessors up until that point would eventually reach its intrinsic physical limits, putting an end to Moore's law [Moo95]. Therefore, the issue of designing parallel computing systems that would break away from the architectural paradigm established by von Neumann [Von93] became ever more pressing.

The von Neumann architecture, which still is at the basis of most modern computers, is founded on the principle of the separation of memory and computation. In other words, data are first retrieved from storage and then sent for processing to the designated units. While nowadays the physical distance that separates storage and computing elements can sometimes be measured in tens of nanometers (like in the case of cache memory directly embedded in the CPU), data transfer remains a very energetically expensive operation [Mol+10]. Therefore, in order to increase energy efficiency, it is desirable that data should be stored in and manipulated by the same functional unit.

The human brain can be seen as a blueprint for a computing system where storage and computation are intertwined. The neuron is the basic unit of such system, whose main function is the integration of the incoming data, in the form of action potentials, while synapses with variable efficacy allow networks of neurons to store information [Hop82 ; Hop88].

The similarities between computers and the brain had been noticed as early as Alan Turing's essay on machine intelligence [Tur48]. However, as the field of computer engineering matured and grew apart from the early influence of neuroscience, the differences became more pronounced. On the other hand, neuromorphic engineering draws inspiration from neuroscience to design devices capable of executing complex intelligent tasks at a fraction of the energy cost of traditional Von Neumann architectures. Throughout the years neuromorphic engineering has branched into different currents with different approaches to the same issue. One such current emerged in the 90's from the work of Carver Mead in the form of analogue circuits designed to execute specific tasks, like for example visual edge detection [All+88]. Another more recent effort is dedicated to the development of digital circuits that reproduce the activity of biological neurons [Ind03 ; WD08], instead of being tailored for a certain specific task. These circuits are relatively simple (usually of the order of tens of transistors for a single neuron device), but can be combined to create neural networks. This development occurred around the same time machine learning, a field which studies how software models of ANN can be employed to execute cognitive tasks [Hop88 ; Kro08 ; Sei04], emerged. The advantage of the machine learning approach is that software models are flexible

and easier to implement, which has resulted in a vast literature of architectures and learning algorithms ; on the other hand, software simulations running on traditional computers or graphics accelerators can incur in higher energy costs than neuromorphic circuits. Recognizing the advantages of software simulations, as well as the need for more efficient hardware, semiconductor companies such as IBM and Intel [Mer+14 ; Dav+18] have begun the development of neuromorphic processors [Peh+22] which integrates neuromorphic principles, like for example event-driven processing, with more conventional design choices, such as the use of digital electronics instead of analogue components, as well as traditional CPU cores in some cases [Fur+14].

One recent development of neuromorphic computing which is of particular relevance to this work is the conceptualization of memristors [Chu71], and their succeeding discovery [Str+08]. To the purpose of this summary, memristors may be described as devices which have a bi-stable resistance whose value depends on its history. This property enables memristors to exhibit a spiking behaviour, making them ideal candidates for implementing neural circuits [Yao+20]. Nowadays there are different devices that may be classified as memristors ; among others, quantum materials that present resistive switching under an applied voltage, like for instance Mott insulators, about which more information is given in the next section.

1.5 Resistive switching in Mott materials

Resistive switching may be defined as the abrupt change of the resistance of a device that occurs under certain conditions, like for instance an applied voltage. This phenomenon is of interest to us in that the surge of current flowing through the device after the collapse of the resistance is akin to the depolarization of the membrane of a neuron when it fires [Wan+20 ; PMW13 ; KSW17]. However, resistive switching alone is not sufficient to implement spiking : it is also essential that the device should resume its high resistance state if the condition that triggered the collapse is lifted, in analogy with the repolarization of the membrane after the emission of a spike.

In Mott materials the physical mechanism behind the resistive switching phenomenon is the Insulator to Metal Transition (IMT) [Geo+96 ; IFT98 ; Lee+18]. According to conventional band theory, Mott insulators should in fact be metals, since they possess an odd number of electrons and their Fermi level should lie in the middle of the valence band ; however, this view fails to account for the strong on-site Coulomb interaction. Modern approaches such as Dynamical Mean Field Theory (DMFT) have been successful in providing a correct description of these materials by including the Coulomb repulsion. To see this one might consider the

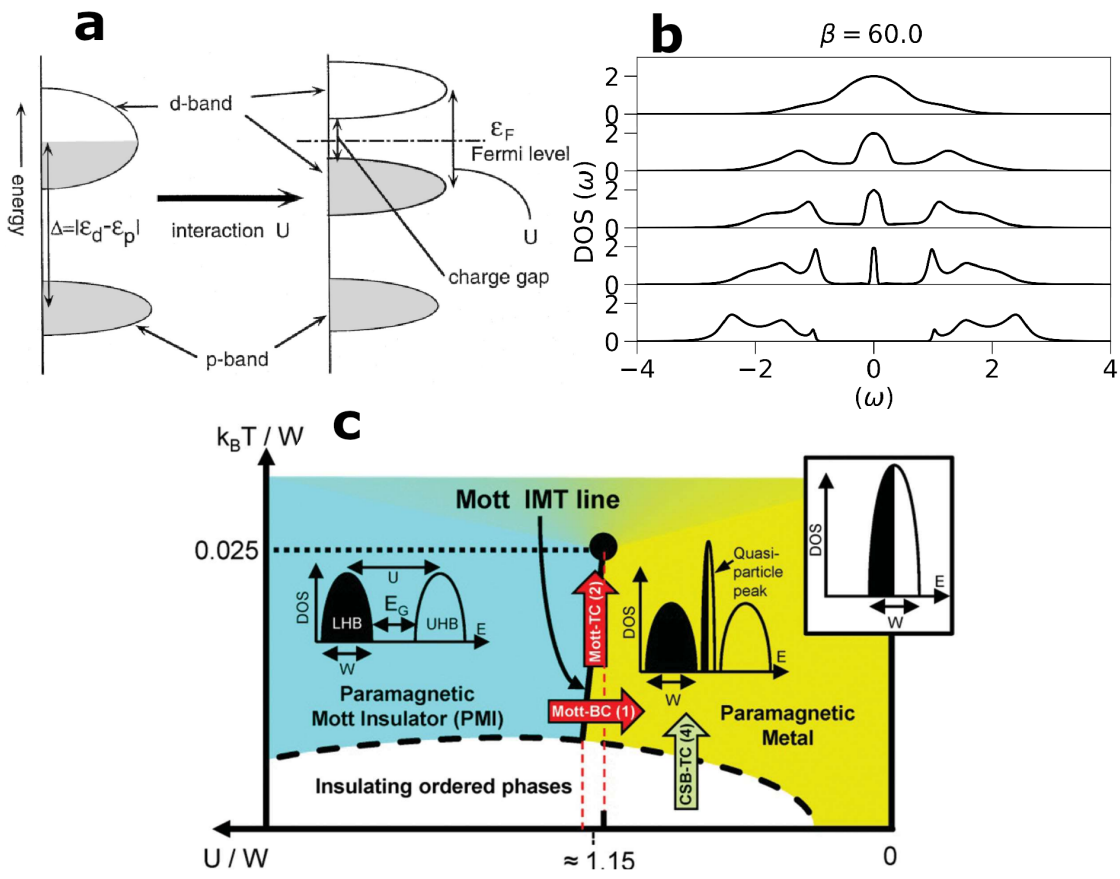

FIGURE 1.2 – Panel a) : Schematic depiction of the Mott transition as the Coulomb interaction U is increased. Adapted from [IFT98]. Panel b) : Plot of $\pi/2$WDOS against the frequency ω obtained from the DMFT solution of the half-filled Hubbard model at $\beta = 60$. Panel c) : Phase diagram of a conventional half-filled Mott compound. Adapted from [Jan+15]

Hubbard model at half-filling, which is one of the most simple models to capture the physics of Mott materials. When the Coulomb interaction U is small, the DMFT solution of the model at zero temperature predicts that the Density of States (DOS) should be finite at $\omega = 0$. As the Coulomb interaction is increased, we observe first the emergence of a quasi-particle peak, and then its narrowing and eventual disappearance ; therefore, when the Coulomb repulsion is strong, an insulating gap $E_G \approx U - W$ (where W is the bandwidth) opens at low frequency splitting the band into two. An example of DOS calculations in the framework of DMFT (using Iterated Perturbation Theory) is presented in panel b) of Figure 1.2, while the general picture of the Mott-Hubbard transition in shown in panel a). From this description we surmise that there exists a competition between the Coulomb repulsion U and the bandwidth W, and that it should be possible to observe a Mott transition by changing the bandwidth, for example by applying pressure to enhance the orbitals overlaps and increase W, and indeed this has been confirmed in experiments [SWB03 ; Hsi+14 ; Jan+15]. If we draw a schematic phase diagram of a conventional half-filled Mott compound (panel c) of Figure 1.2), we can see the bandwidth controlled Mott transition (Mott-BC, red arrow) that occurs from the metallic state to the paramagnetic Mott insulator state when the ratio U/W is increased. Moreover, we also see a temperature controlled transition (Mott-TC, red arrow) from the metallic to the Mott insulator state made possible by the fact that the Mott IMT line is tilted. Finally, in those half-filled compounds that present long-range order (for example magnetic or orbital) at low temperatures, we also see a temperature controlled IMT that, unlike the two previously described Mott transitions, involves a crystallographic symmetry breaking (CSB-TC, green arrow).

In this work we will deal with materials, such as VO2 and V2O3, that present a transition from a low temperature insulator state to a high temperature metallic one under an applied electric field. Different mechanisms have been proposed to explain this transition, such as Joule self-heating [Li+17 ; Kim+10 ; Zim+13](similarly to the CSB-TC transition described above) and charge promotion by the electric field[Sto+14 ; Gui+13 ; Roz97], which would dope and destabilize the Mott state. Since a microscopic description of the IMT is outside the scope of this work, in this section we will only give a phenomenological description of the resistive switching phenomenon as observed in experiments ; in later chapters we will study this phenomenon in more details, finding that both Joule heating and an electronic contribution, in the form of current concentration within thin metallic domains, play an important role.

For now, we focus on the case of a VO2 sample under an applied electric field. This case is of particular interest for practical applications for two reasons. Firstly, inducing the transition via an electric field is suitable for integrating the device

with other electronic components. Secondly, the transition temperature of VO2 is above room temperature, making it possible to cool the sample simply by thermal dissipation to a substrate [Del+21].

A schematic depiction of the setup for this kind of experiments is shown in panel a) of Figure 1.3 . The Mott material sits between two electrodes, which apply a constant electric field. A substrate is used to dissipate the heat produced by the sample when the electric field is turned on. By recording the current through the sample with an oscilloscope, it is possible to observe the switching from insulator to metal, which is marked by the sudden collapse of the resistance, after an initial phase in which it decreases gradually (panel b)). The transition may be further characterized by heating up the sample while a minimal voltage is applied only for the sake of probing the resistance. In this case it is possible to measure the resistance against the sample temperature, and operationally define its transition temperature as the temperature at which the resistance collapses which, for VO2, is $T = 340K$ [Del+21]. Moreover, starting from the metallic state, we can decrease the temperature to study the relaxation to the insulating one [Tes+18]. For materials like VO2, which present a first order IMT, a hysteretic behavior is observed, that is, the temperature at which the resistance resumes its high insulating value is lower than the transition temperature. The hysteretic behavior of materials like VO2 and V2O3 is fundamental to the stochastic firing behavior that has been observed experimentally and that is discussed in this work [Roc+22]. In addition to VO2 and V2O3 there are other materials, like for instance V3O5 [Add+22], which present a second order transition, which is characterized by a less abrupt change in the resistance and the absence of hysteresis.

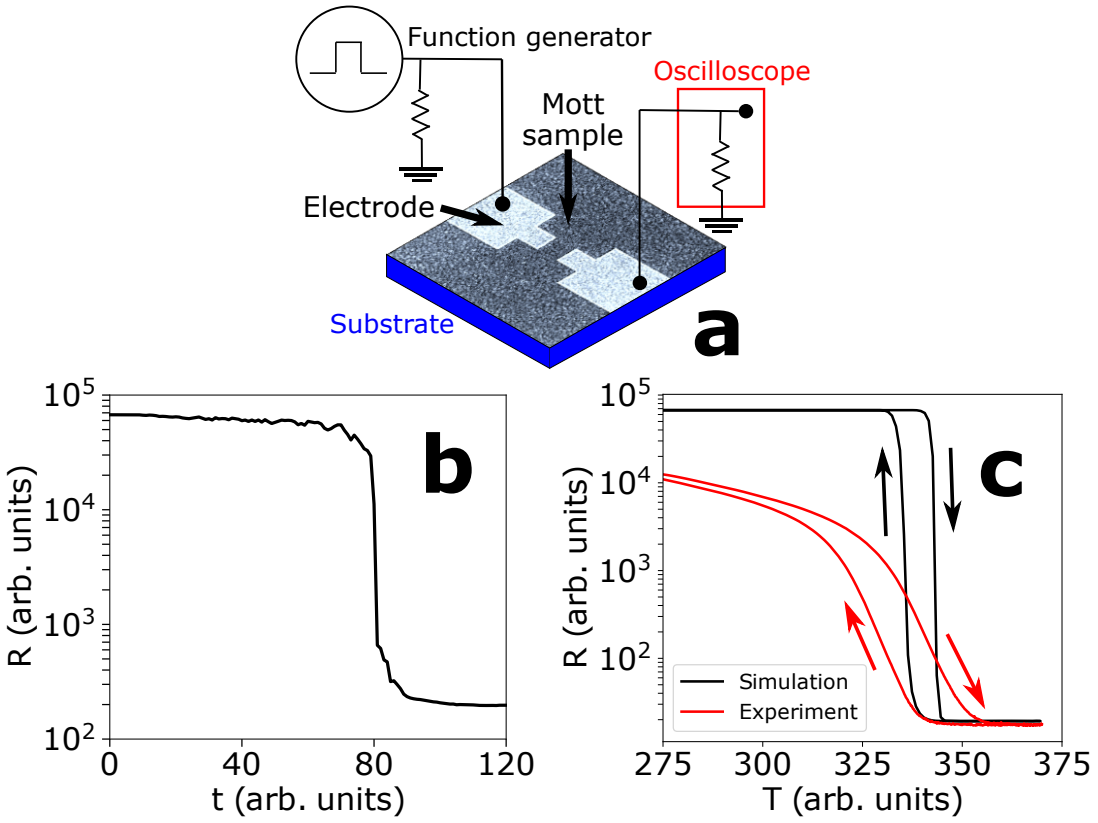

FIGURE 1.3 – Panel a) : Schematic representation of the setup of a resistive switching experiment. A function generator applies a fixed electric field across a Mott insulator that sits between two electrodes. A substrate at fixed temperature is used to dissipate the heat. Panel b) : Evolution of the resistance of a simulated Mott material under an applied voltage using the MRN model. Panel c) : Hysteretic behavior of the resistance of an experimental VO2 sample and a MRN simulation as a function of temperature. The insulating value of the resistance in this simulation has been fixed and is temperature independent for simplicity's sake. When considering the case of nickelates later on we will show that it is possible to introduce a temperature dependent insulating resistivity in the model.

Chapitre 2

The Mott resistor network model

The resistive collapse that occurs in Mott materials like VO2 and V2O3 under an applied voltage is triggered by the growth of metallic filaments within the insulating bulk of the sample, which eventually shortcircuit the electrodes thus inducing an electric breakdown [Del+21 ; Add+22 ; Roc+22 ; Gué+13]. This process can be observed through imaging experiments such as the one that is schematically depicted in panel a) of Figure 2.1[Del+21]. In this experiment a constant electric field is applied to a VO2 sample in order to induce the collapse of the resistance. Additionally, a laser beam is pointed toward the sample and a photodetector is used to measure the reflectivity of the material. By moving the laser beam in parallel to the electrode it is possible to measure how the reflectivity of the region of the sample hit by the laser changes over time (panel b), Figure 2.1) and since reflectivity is higher for the metallic phase than for the insulating one, we can also study how the resistivity changes as the material undergoes resistive collapse. From Figure 2.1 it is possible to appreciate how the resistive transition under an applied voltage is not a wholly homogeneous process in which the sample becomes uniformly metallic ; instead we see the formation of metallic regions near the edges of the electrode that gradually expand over time as the electric field is kept on. Similar optical reflectivity measurements conducted on V3O5 (Figure 2.2)[Add+22] clearly show that a metallic filament connecting the electrodes appears after the collapse of the resistance.

These imaging experiments shed a light on the physical origin of the resistive collapse ; however, the limited temporal resolution of the instrumentation does not allow to capture the state of the filament during the percolation phase, when it is only partially formed. Additionally, filament percolation itself requires further investigation, particularly in regards to whether it is a purely thermal process or one that is also affected by electronic contributions [Sto+14 ; Li+17]. For these reasons we've employed the Mott Resistor Network (MRN) model to study the resistive collapse in Mott materials. The MRN (depicted in Figure 2.3) is a mesoscopic phe-

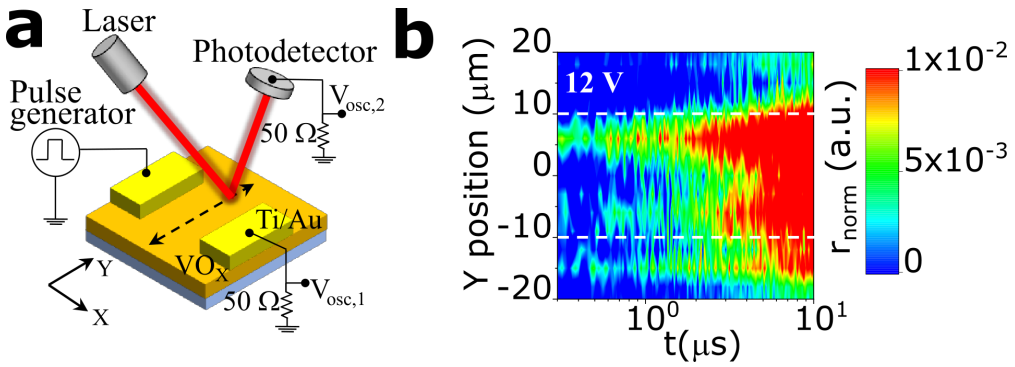

FIGURE 2.1 – Panel a) : The setup used to measure the resistivity of VO2 and V2O3 samples. A constant electric field is applied to induce the resistive switching while a laser beam is shot toward the sample. A photodector measures the reflected beam, from which the reflectivity of the material, and thus the resistivity, can be computed. Panel b) ; The evolution of the reflectivity of a horizontal patch of the sample, parallel to the electrode, as the electric field is kept on. On the y axis the position of the beam, which moves in parallel to the electrode in order to produce the figure, and on the x axis time in logarithmic scale. Dashed white lines indicate the position of the edges of the electrode. Adapted from [Del+21]

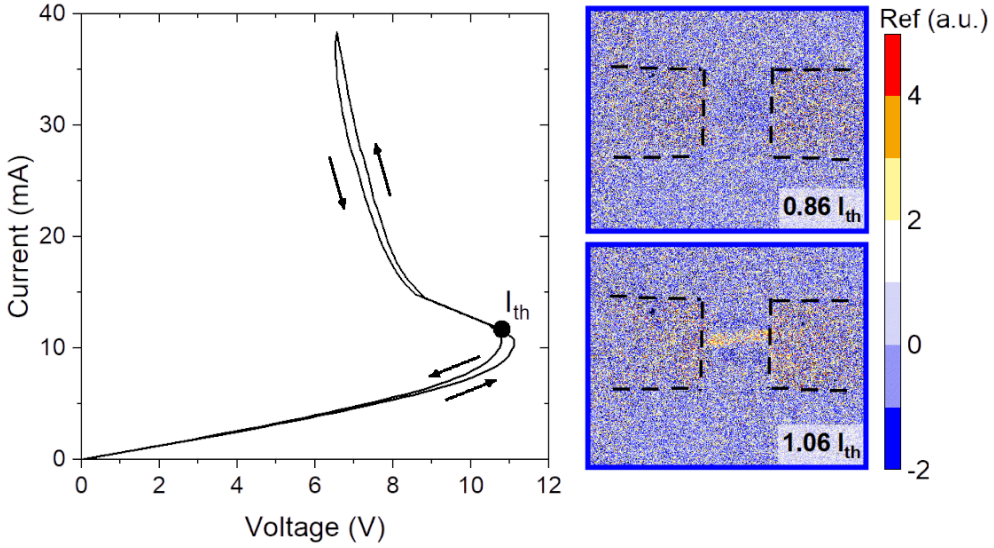

FIGURE 2.2 – On the left, IV curve of a V3O5 sample in a current-controlled experiment. The jump in the voltage corresponds to the resistive collapse. On the right, reflectivity measurements showing how the voltage jump, which occurs between the upper and the lower panel, coincides with the formation of a metallic filament that connects the electrodes. Adapted from [Add+22]

nomenological model that is capable of producing snapshots of the temperature and resistivity of the materials at any point in time, as well as providing readings for macroscopic quantity such as the sample current [Sto+13].

The model divides the sample into cells, the size of which is assumed to be large enough to define a resistivity value as well as a phase : either Mott insulator or correlated metal. Since the gap between the electrodes in the materials under examination is typically of the order of $1 - 10\ \mu m$, a length of approximately 100 cells is chosen for the MRN, which translates to a cell size of $10 - 100\ nm$, comparable to the size of the crystalline grains of the experimental films [Val+21]. In order to include the first order character of the IMT in the materials under study, such as VO2 and V2O3, we assume that the stability of the two phases depends on the local temperature of the cell via a free energy functional [Tes+18], which we will define later on.

Using as a reference Figure 2.3, we see that the model includes red cells, which are ideally metallic and represent the electrodes, white cells, which are in the insulator phase and have high resistivity values, gray cells, which are in the correlated metal phase and have a lower resitivity, and finally green cells, which are ideally insulating. Green cells are not required by the model, and only serve the purpose of reproducing the experimental geometry (also depicted in Figure 2.3, on the left) while using fewer cells than otherwise necessary. Each of the cell has four resistor, as shown by the inset of Figure 2.3, all sharing the same resistance value, which we identify with the resistivity of the cell (the cell is assumed to be of unitary size, and all the physical quantities have arbitrary units).

When a voltage is applied across the network, currents start flowing through the resistors. The first step toward the solution of the model consists in computing these currents. To do so we use Kirchhoff Voltage Law, which states that the sum of the voltage drops along a closed loop is zero. Looking at Figure 2.4, we see that for each cell a closed loop can be defined by considering its node and the three other nodes with which it forms a square. Then, using Ohm's law $IR = V$, we can write the sum of voltage drops across the resistors included in the loop, and impose that it should be zero, in accordance with KVL. As an example, considering the cells R_3, R_4, R_7, R_8 of Figure 2.4

$$\begin{aligned} &2I_3\left(R_3 + R_4 + R_8 + R_7\right) - I_0(R_3 + R_4) + \\ &- I_4(R_4 + R_8) - I_{10}(R_8 + R_7) - I_2(R_7 + R_3) = 0 \end{aligned} \tag{2.1}$$

The values of the resistive coefficients are known, since initially all the cells are in the insulator state, however the number of currents (which are the unknown variables of this equation) to be computed is too high, since at this point we only have one equation. However, a similar equation can be written for any other cell

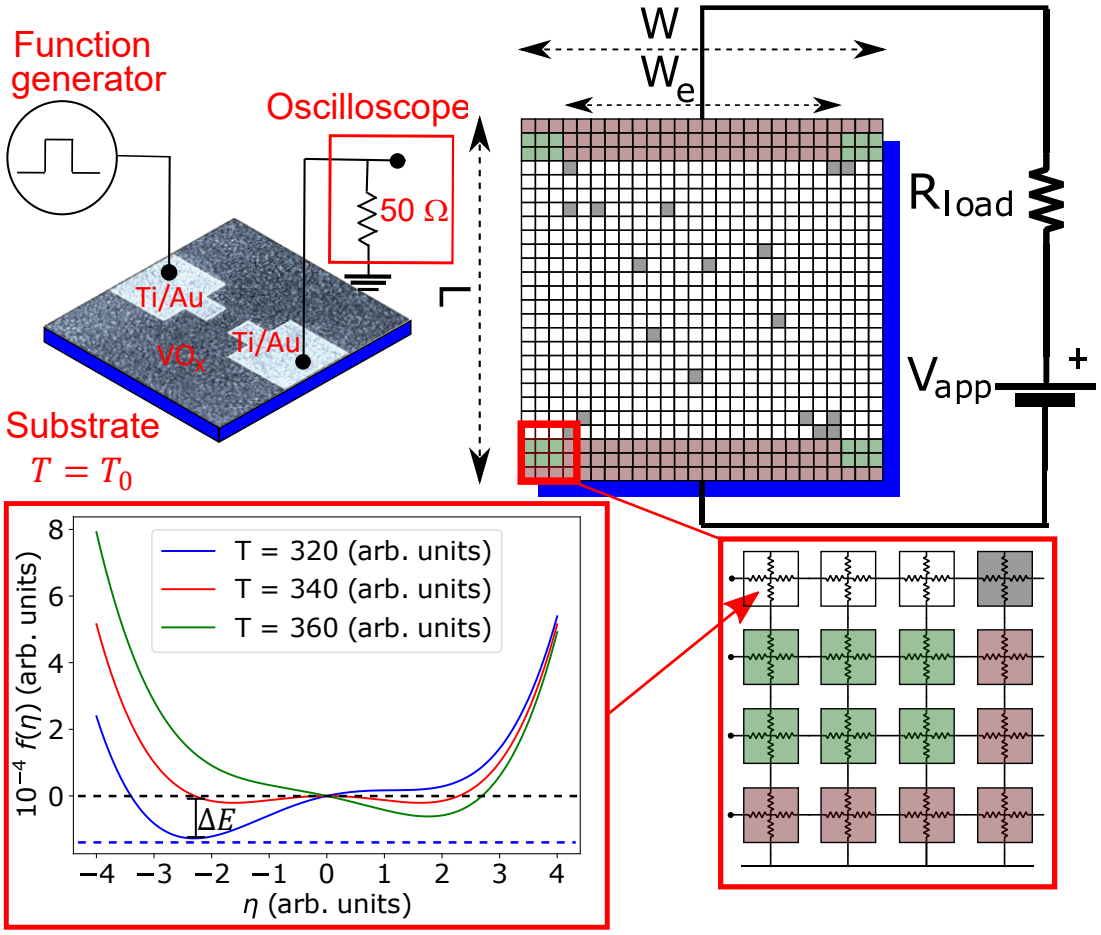

FIGURE 2.3 – Schematic diagram of the Mott Resistor Network model and the experimental setup [Val+19]. Cells in red are ideal metal with zero resistivity and represent the electrodes. Cells in white and grey represent the thin film Mott material, which is assumed in thermal contact with a perfectly insulating substrate that is at $T_0 = 300$ arb. units (in blue). These cells can be either in the insulating or metal states. Green cells are ideally insulating. Each cell is characterized by a Landau-type free energy that evolves with the temperature of the cell, as shown in the bottom inset figure. The two minima of the function correspond to the metal and insulating phase. The energy barrier ΔE of the insulating phase at three different temperatures is shown.

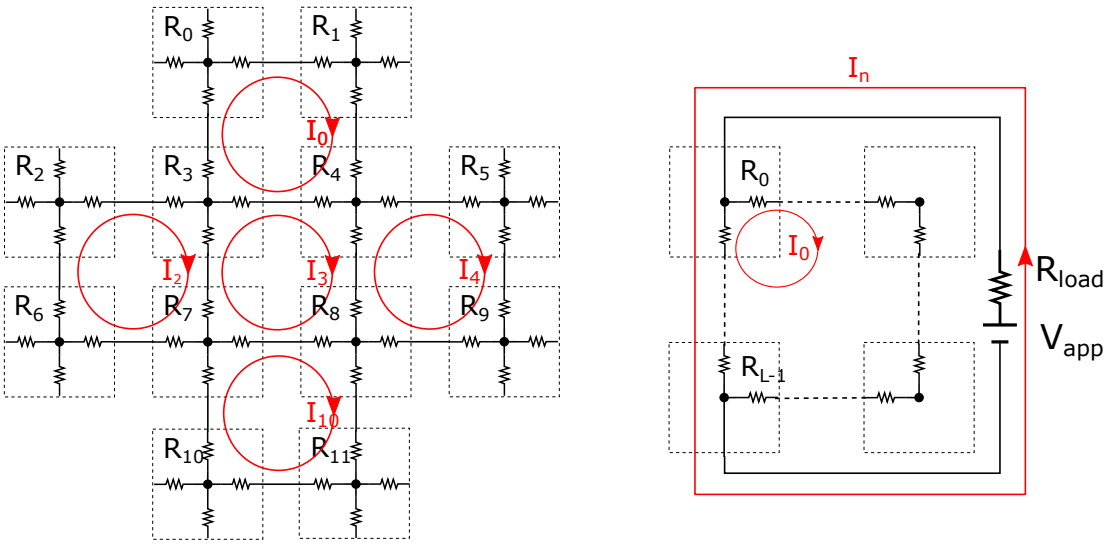

FIGURE 2.4 – Left : For each cell of the mesh it is possible to define a closed loop and a current that flows within it by considering the three other cells with which it forms a square. In our example one such loop consists of the nodes 0, 1, 3, 4. The current takes the name of the top left node Right : To include the external applied voltage and the load resistor in the computation of the currents we can consider the loop made of the leftmost column of the mesh, the load resistor and the applied voltage.

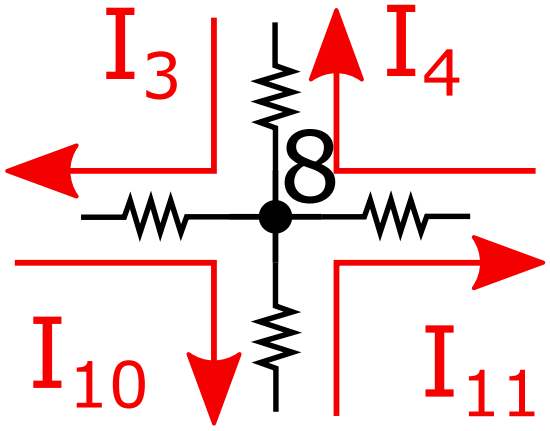

FIGURE 2.5 – Each cell contains four resistors, and for each resistor there are two currents flowing in opposite directions. Here we consider as an example node 8 of Figure 2.4

of the network, and we note that the currents are shared by closed loops adjacent to each other. Thus we end up with a system of linear equations of the form

$$I\mathbf{R} = \Delta V \tag{2.2}$$

where I is a row vector of length n, the total number of cells, containing the currents of the loops, $\mathbf{R}$ is a square matrix of size n which contains the resistive coefficients, and ΔV is a column vector which in principle should contain voltage values, but we know it to be zero according to KVL. There is one last equation left to be written, which is the one of the closed loop that contains the external load resistor, as well as the voltage generator. This equation is very important, since it allows us to introduce the external current in the network. To write it, we must consider a closed loop that contains the voltage generator and the load resistor, enters the network, runs through it and then exits the network to connect back to the voltage generator. While any path satisfying these conditions would do, we choose the one that run alongside the leftmost column of the network, as shown in Figure 2.4, as this simplifies the writing of Kirchhoff's equations (since we don't have to worry about potential currents shared with the nearest neighbours cells on the left). As a consequence, the current will enter the network through the top leftmost cell (as opposed to the center cell, as it might be expected), and this is why a row of metallic cells is needed to carry the current from that cell to the center of the sample (as shown in Figure 2.3). This last equation can be written as follows (using the naming convention of Figure 2.4)

$$\begin{aligned} &I_n(R_0 + 2R_1 + 2R_2 + \cdots + R_{L-1}) + I_n R_{load} + \\ &- I_0(R_0 + R_1) - I_1(R_1 + R_2) + \cdots - I_{L-1}(I_{L-2} + I_{L-1}) = V_{app} \end{aligned} \tag{2.3}$$

In total we have a system of linear $n + 1$ equations that has been set up by recurrent application of KVL, which we can now solve. We note that the matrix of resistive coefficients is sparse and mostly empty, since for each equation only the resistive coefficients of the cells that belong to the corresponding closed loop are considered. For this reason, we use the library umfpack to solve the system [Dav04] (here we note that the library requires that the matrix of the resistive coefficients should be provided in compressed column representation). Once umfpack has solved the system for an initial applied voltage, we have successfully computed the currents of the closed loops. Now we must turn our attention to the power that is generated by these currents as they flow through the resistors.

Heat is locally generated in each cell in accordance with Joule's first law $P = I^2R$. In particular, we can see from Figure 2.5 that for any resistor there are two currents flowing in opposite directions. Thus, taking as an example node 8, the power generated by a single cell may be written as

$$\begin{aligned} P_8 =& R_8[(I_8 - I_4)^2 + (I_8 - I_{10})^2 + \\ &+ (I_{10} - I_3)^2 + (I_3 - I_4)^2] \end{aligned} \tag{2.4}$$

The power of any given cell will be the sum of the contributions of its four resistors. Now that we know how to compute the heat generated by a cell we can study how the temperature is affected. To write the temperature equation of the cell we begin by considering Newton's law of cooling

$$\frac{dq}{dt} = -hA\nabla T \tag{2.5}$$

which states that the rate of heat transfer is equal to minus the heat transfer coefficient h multiplied the heat transfer surface A and the temperature gradient. The thermal conductivity κ is related to the heat transfer by the equation $k/dx = h$, where dx is the thickness of the medium. Therefore, the above equation can be rewritten as

$$\frac{dq}{dt} = -\frac{k}{dx}A\nabla T \tag{2.6}$$

Since in our simulations we consider thin films, we assume that the thickness dx is unitary. We also assume that the surface of the cell A is unitary as well. Finally, using the definition of the heat capacity as the amount of heat needed to raise the temperature $C = dq/dT$, we may rewrite the equation as

$$\frac{dT}{dt} = -\frac{k}{C}\nabla T \tag{2.7}$$

The resistor network is assumed in thermal contact with a perfectly insulating substrate (depicted in blue in Fig.2.3). Each cell dissipates the heat by thermal conduction to its four neighbouring cells and to the substrate, that is assumed at a fixed temperature T_0. The thermal conductivity κ determines the magnitude of the heat transfer ; for simplicity we assume the thermal conductivity to be the same for the dissipation to the substrate and to the nearest neighbours. Therefore, the temperature gradient for the cell with subscripts ij (identifying the row and column of the network the cell belongs to) can be written as

$$\nabla T = T_{ij} - T_0 + 4T_{ij} - \sum_{kl}^{nn} T_{kl} = 5T_{ij} - \sum_{kl}^{nn} T_{kl} - T_0 \tag{2.8}$$

where the subscripts kl run over the nearest neighbours of the cell. The temperature of each cell results from the action of two effects : a positive contribution,

due to Joule heating (equation 2.4), and a negative one, due to heat dissipation (equation 2.8). Putting them together, equation 2.7 becomes

$$\frac{dT_{ij}}{dt} = \frac{P_{ij}}{C} - \frac{\kappa}{C}\left(5T_{ij} - \sum_{kl}^{nn} T_{kl} - T_0\right) \tag{2.9}$$

where ij and kl are the indexes of the cell, nn denotes nearest neighbours and C is its thermal capacity. In the limit of the thermal conductivity κ going to 0 the film self-heats-up approximately homogeneously since the temperature gradients may be neglected. Then, the temperature change for the film as a whole can be written as

$$\frac{dT}{dt} = \frac{I^2 R(T)}{C} - \frac{K}{C}(T - T_0) \tag{2.10}$$

where K is the thermal conductance of the interface, and C now denotes the heat capacity of the film. In the following we will use the symbol K to denote both the thermal conductivity and the thermal conductance, for the sake of simplicity, whenever the meaning can be inferred from the context. The temperature T_0 is assumed to be below the insulator to metal transition temperature T_{IMT}, thus, initially, all cells are in the insulating phase and have a high resistivity value ρ_{high}. When the cells undergo the transition to the correlated metal phase, their resistivity value changes to $\rho_{low} \ll \rho_{high}$. For simplicity, both resistivities are assumed to be independent of T, but the model can be easily generalized to include any temperature dependence [Sto+14].

The transition of the cell is a thermally activated process that may occur even for temperatures lower than T_{IMT}, in accordance with the following transition rate

$$\nu(T) = \nu_0 \exp\left(-\frac{\Delta E(T)}{T}\right) \tag{2.11}$$

where T is the local temperature of the cell, $\Delta E(T)$ is the energy barrier of the cell free energy when it is in the insulating state, and ν_0 is the attempt rate [Sto+13]. The free energy is assumed to follow Landau's theory and to be of the shape :

$$f(T, \eta) = h(T)\eta + p(T)\eta^2 + c\eta^4 \tag{2.12}$$

$$h(T) = h_1 \frac{T - T_C}{T_C} + h_2 \tag{2.13}$$

$$p(T) = p_1 \frac{T - T_C}{T_C} \tag{2.14}$$

where η is the order parameter and h_1, h_2, p_1, c and T_C are constants (T_C, which is the critical temperature of the free energy, should not be confused with T_{IMT}, which is the insulator to metal transition temperature). Here we do not make any explicit connection between η and the physical quantities, however we may notice that a mapping between it and the resistivity of the cell is, in principle, possible. The parameters of the free energy are tuned as to reproduce the experimental curves of resistance versus temperature (see insets of Figure 2.6), from which one can gauge the temperature range within which the system presents meta-stability, which manifests in the hysteresis.

The model can be simulated both in equilibrium and out of equilibrium, for small and large applied voltages, and also for arbitrary applied voltage protocols. In a simulation in equilibrium conditions, a minimal voltage, needed to probe the resistance, is applied. Then the temperature of the substrate is slowly raised. Under these conditions the system heats up in an approximately homogeneous fashion. As the system crosses T_{IMT}, the cells independently and randomly undergo local transitions and relaxations and no filamentary structure forms. As the temperature is raised beyond the transition temperature eventually all cells are in the metallic phase. After the resistive collapse, we gradually decrease the temperature of the substrate to the initial value, and from the computed $R(T)$ we obtain the hysteretic behaviour of the resistance. This is shown in the insets of Fig.2.6, where we compare the numerical results with experimental data on a VO_2 thin film sample.

When a strong voltage is applied, the system is driven out of equilibrium and the resistive collapse is qualitatively different. The metallic phase takes a filamentary percolation form as is observed in the simulation data of Fig.2.6. The formation of metallic filaments is a highly non-linear process that originates in a local thermal imbalance at large current densities. When a voltage is applied to the electrodes, a current begins to circulate through the Mott resistor network, and the cells start to generate heat, in accordance with Joule's law. At first, the rate at which the heat is generated is comparable to that at which it is dissipated to the substrate, which is in thermal contact with all cells and is kept at a fixed T_0. However, if the applied voltage is increased, the injected power eventually overcomes the ability of the substrate to absorb heat. In this situation, a local increase in the current (such as at the edges of the electrodes due to the point effect) leads to a local increase in temperature. Then, the probability that a hot cell becomes metallic also increases, since the transition is a thermally activated process. When a cell becomes metallic, its resistance decreases dramatically, since $\rho_{low} << \rho_{high}$. This draws more current from the neighboring cells to the metallic one, increasing its current density. This *current focusing* effect translates into further local heating, along with a dramatic increase of the transition probability of the neighboring cells that also heat up by Joule heating and by thermal conduction. Eventually, this

process leads to the formation of conductive filaments that connect the electrodes. It is important to realize that for the resistive collapse to take place the device as a whole does not need to homogeneously reach the T_{IMT}. It is merely necessary that T_{IMT} is reached *locally* and that the ρ_{high}/ρ_{low} ratio [Del+21] is significant enough to create the current focusing effect.

The previous qualitative discussion of the filamentary formation process is confirmed by the numerical simulations that we show in Fig.2.6. There we observe that, initially, the filaments emerge from the edges of the electrodes and grow in approximately symmetric fashion, until they eventually connect. This is a manifestation of the familiar point-effect, namely, the enhancement of the electric fields near sharp angles. It is in these regions that the current density is initially stronger, even though the device cells are originally all identical and in the insulating state. The current gradients of geometrical origin act as seeds for the filamentary growth and have recently been directly imaged (Figure 2.1) [Del+21]. The growth of the filaments is correlated with the resistance of the device, as shown by the right hand side panel of Fig.2.6 and the respective points indicated along the collapse of the $R(t)$ in the main panel.

When the applied voltage is terminated, there is no more power input and the temperature of the cells relaxes back to $T_0 < T_{IMT}$, thus the device recovers the high resistance state. This *relaxation* of the filamentary structures has been studied in recent works [Tes+18 ; Val+19] and may be seen as the inverse of the filament incubation and growth that we consider here.

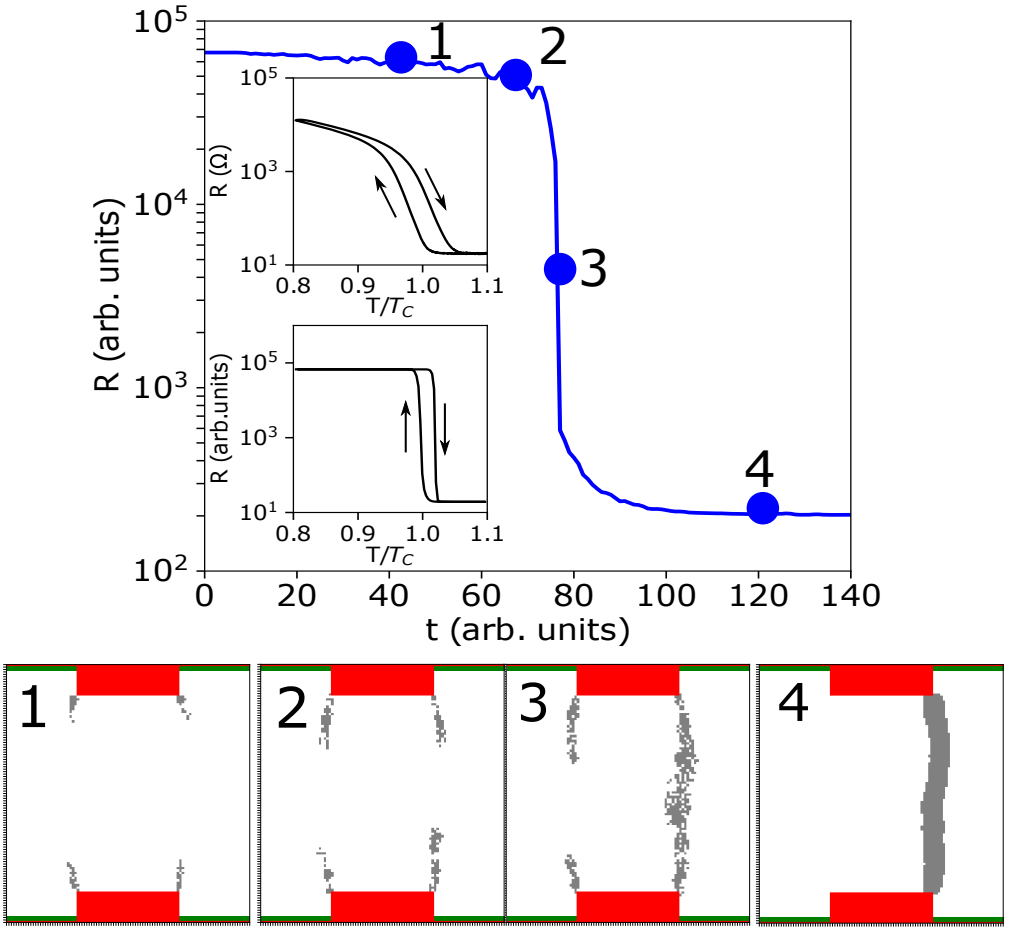

FIGURE 2.6 – The top panel shows the drop of the resistance of the simulated MRN when driven out of equilibrium by an applied voltage (blue curve, $V_{app} = 10^5$ arb. units, $K = 0.1$ arb. units). The top inset shows the experimental hysteresis curve for a VO_2 thin-film sample, the bottom one shows the curve produced by the model simulations in equilibrium conditions. The panels on the bottom show the resistivity map of the simulated system as it undergoes the resistive switching. The maps are ordered chronologically and, similarly to Fig.2.3, the electrodes are in red, the cells in the insulating phase in white and the metallic cells in grey ; green cells are ideally insulating. We see that the first cells to switch to the metal state are those near the edges of the electrodes, since the electric field is stronger due to the point effect. As we keep applying the voltage, the filaments grow, until one of them shortcircuits the electrodes.

Chapitre 3

Noisy firing in Mott neurons

The first question that we tackle using the MRN is the stochastic nature of the field driven resistive collapse in VO2 and V2O3 [Roc+22]. It has been observed that the collapse of the resistance can occur at different times when experiments are repeated using the same sample and the same applied voltage [Del+21]. If we define the incubation time as the time between the application of the voltage and the collapse of the resistance, one can describe quantitatively the stochastic behavior in terms of variability of the incubation times. It is then possible to plot the incubation times, and their standard deviation for a certain number of trials, against the applied voltage. This plot summarizes the stochastic behavior of VO2 and V2O3, and it is the starting point of our analysis. Using the MRN we were able to understand filament percolation as an intrinsically stochastic process, to which both thermal and electronic effects, in the form of Joule heating and current density concentration respectively, contribute. By controlling one of the parameters of our simulations, the thermal conductivity of the sample, we were able to tune the stocasticity of the resistive collapse, thus reproducing the experimental incubation times of VO2 and V2O3.

Stochasticity is an important feature of the spiking behaviour of biological neurons. As expected of biological systems, neurons are not completely deterministic, and the timings of the spikes of any given neuron will present a certain variability [Ger+14]. In other words, spiking is a noisy a process, a fact that is captured in neuronal models by the use of a probabilistic threshold of firing, which often takes the form of an exponential escape rate [Jol+06 ; PG00 ; Ger+14]. A noisy output can negatively impact the performance of neuronal networks as computing systems ; however, there are instances in which noise can actually enhance performance, a phenomenon that is referred to as stochastic resonance [SGJ05]. For these reasons, it is desirable that memristive neurons should also possess stochasticity.

In this work we go beyond the qualitative description of filament percolation as a stochastic process to show that the probability distribution of resistive col-

lapse is the same as that of firing in neuronal models with an exponential escape rate. In doing so we establish a quantitative connection between conventional mathematical descriptions of noisy firing and stochastic spiking as implemented by Mott materials ; this allows us also to show that filament percolation is a Poisson process, in analogy with neuronal firing.

3.1 Stochastic filament percolation

A useful quantity to characterize the formation of filaments is the delay time between the application of the external voltage and the observation of the resistive collapse, which we call the incubation time τ_{inc}. This quantity is directly accessible in experiments, which show that τ_{inc} depends strongly on the applied voltage, spanning several orders of magnitude. The lowest voltage that is required to observe a finite τ_{inc} is denoted the threshold voltage V_θ. As we shall discuss below, the determination of the threshold voltage may be more subtle than naively expected.

In the right panel of Fig.3.1 we show experimental data for the incubation times of VO_2 and V_2O_3 devices (see Fig.2.3 for the experimental setup). We notice that, for a relatively small variation of the applied voltage, τ_{inc} may change by orders of magnitude. Upon a closer look, we observe two qualitative features : one is a steep increase of τ_{inc} as the threshold voltage for resistive collapse, V_θ, is approached ; the second is that the variability (i.e. the experimental error bars) of τ_{inc} also grows when decreasing the voltage. Moreover, in VO_2 the error bars are large and of the same order of magnitude as their respective mean τ_{inc}, and in the case of V_2O_3, they grow at an even higher rate approaching V_θ. This behavior indicates that the more the applied voltage approaches the threshold value, the more *unpredictable* the filamentary formation becomes, which questions the very notion of a well defined threshold voltage value.

To understand these experimental findings we turn our attention to the study of the MRN model. Since it has several parameters, we need to choose a convenient way to explore the behavior of the resistive collapse. It has been experimentally observed that a relevant parameter is the ratio of the insulating and metallic resistivities ρ_{high}/ρ_{low} across the IMT [Del+21]. However, for the time being, we find it convenient to keep the values ρ_{high}, ρ_{low} and T_0 fixed and explore the different resistive collapse modes with the variation of a single parameter, the thermal conductivity K. A summary of the parameters of the model used in this chapter is presented in Table 3.1. In the succeeding chapters we will also explore how the resistive collapse is affected by the resistivity ratio and the substrate temperature, but for now focus only on the thermal conductivity.

In the limit $K \to 0$ even a very low applied voltage produces self-heating as the cells do not dissipate the incoming power. The local self-heating is more intense

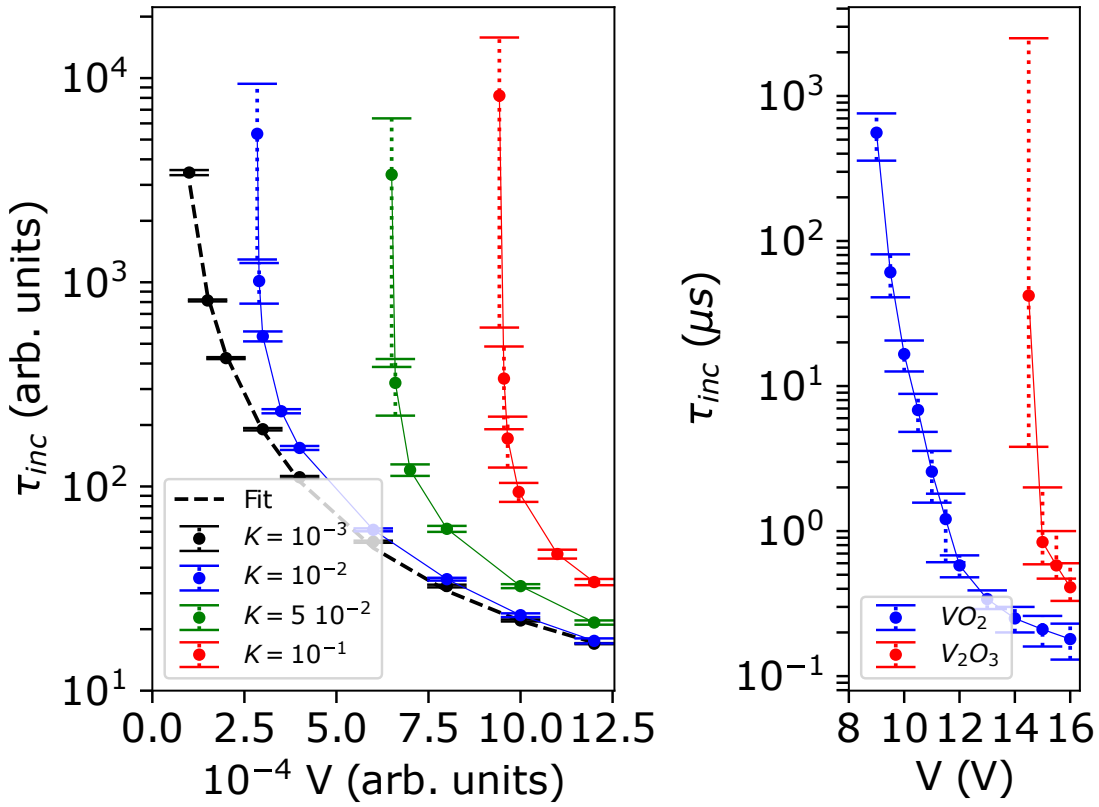

FIGURE 3.1 – In the left panel the incubation times produced by numerical simulations of the MRN model at different K values. The dashed black line is a fit using the expression Eq.3.3, while the other lines are simple guides to the eyes. Error bars represent the standard deviation of the incubation times. In the right panel the incubation times measured for a VO_2 and a V_2O_3 device, in contact with substrates at $T = 334.9$K and 132K, respectively. The substrates were made of Al_2O_3, which has a thermal conductivity of $25W/mK$. The experimental data are the same as in [Del+21]

Parameter	Value	Meaning
h_1	$71.25\ 10^3$	Free energy constant
h_2	$7.5\ 10^3$	Free energy constant
p_1	$15.0\ 10^3$	Free energy constant
c	$3.0\ 10^2$	Free energy constant
T_C	380.0	Free energy constant
T_{IMT}	340.0	Insulator to metal transition temperature
T_0	300.0	Substrate temperature
ρ_{ins}	$3.5\ 10^4$	Cell insulating resistivity
ρ_{met}	10	Cell metallic resistivity
R_L	$5\ 10^3$	Load resistance
C	10	Heat capacity
W	100	Network width
W_e	42	Electrodes width
L	100	Network length
K	$[0.001, 0.1]\ C$	Thermal conductivity

TABLE 3.1 – Values of the parameters used in the simulations presented in this chapter.

at the edges of the electrodes, where the electric field and the current density are larger, due to the point effect. Then it spreads out rather homogeneously in the bulk of the device. The self-heating continues at a rate set by the applied voltage, and since there is little dissipation, eventually the temperature of the bulk reaches T_{IMT} and the resistance collapses.

In contrast, in the limit of large K, a stronger voltage must be applied to induce the resistive collapse, since the dissipation to the substrate brings thermal equilibrium at low injected power. Therefore, one expects stronger temperature gradients and, consequently, stronger gradients of current density, which may lead to a less predictable resistive collapse. As we shall see below, in such a case, filamentary structures grow as in a sudden avalanche-like process, especially close to the threshold voltage.

The results of the simulations are shown in the left panel of Fig.3.1 where we plot the incubation time τ_{inc} as a function of the applied voltage for various values of the parameter K. We observe that several features of the experimental data shown in the right panel are present. Firstly, the range of τ_{inc} spans several decades for relatively small variations in the applied voltage. Additionally, there are two different regimes in $\tau_{inc}(V)$: The first one is at higher voltages, where $\tau_{inc}(V)$ shows a relatively weaker V-dependence and smaller error bars. The second regime is at lower voltages, close to the threshold, showing a steeper increase in τ_{inc} with

V and larger error bars. We thus call the first regime deterministic, and the second one stochastic. We will now explore the origin of the stochastic behavior.

A first insight comes from the observation that, in the limit of $K \to 0$, the resistive switching becomes deterministic. This feature can be observed in Fig.3.1 where, in the limit of vanishing thermal conductivity, the variability of the incubation times remains small even close to the threshold voltage. The deterministic nature of the resistive collapse in this case is further underlined by the fact that we can obtain an approximate analytic expression for $\tau_{inc}(V)$ by solving Eq.2.10 under the assumption of an homogeneous system and that the resistance of the sample stays constant and equal to R_{ins} before the collapse. Choosing as boundary conditions for the solution $T(0) = T_0$ and $T(\tau_{inc})$=T_{IMT} and inverting the relation between temperature and time, we get the thermal incubation time τ_{inc}^{th} :

$$\tau_{inc}^{th} = -\frac{C}{K} \ln \left(1 - \frac{K R_{ins}}{V^2} (T_{IMT} - T_0) \right) + \tau_0 \tag{3.1}$$

The small constant τ_0 is the minimal time that it may take the system to switch in the infinite V limit. We may define the thermal threshold voltage, V_θ, as the value of the applied voltage for which incubation times diverge :

$$V_\theta = \sqrt{K R_{ins} (T_{IMT} - T_0)} \tag{3.2}$$

Thus, equation (3.1) can be rewritten as

$$\tau_{inc}^{th}(V) = -\frac{C}{K} \ln \left(1 - \frac{V_\theta^2}{V^2} \right) + \tau_0 \tag{3.3}$$

As shown in the left panel of Fig.3.1, this analytic expression provides an excellent fitting form for the numerical simulation data obtained at the smallest K. Thus, we may consider this behavior as the reference for a purely thermal resistive collapse due to self-heating alone.

We can now examine the dynamical evolution of the system as it evolves towards the resistive collapse at τ_{inc} by taking snapshots of the temperature and resistive maps of the MRN model. We find three different characteristic regimes (Fig.3.2). The panels of the top row depict the evolution when K is small, i.e. in the prototypical thermal case. We observe that the temperature gradients are relatively small, except at the edges of the electrodes. The heating in the central part of the system is gradual and homogeneous. The color code shows that the temperature in the center reaches $T \approx T_{IMT}$ just before the resistive collapse (last panel).

The second row of panels of Fig.3.2 shows the temperature and resistance maps in the deterministic regime of large K. This occurs at voltages that are high compared to the threshold, where the error bars of τ_{inc} are relatively small (cf

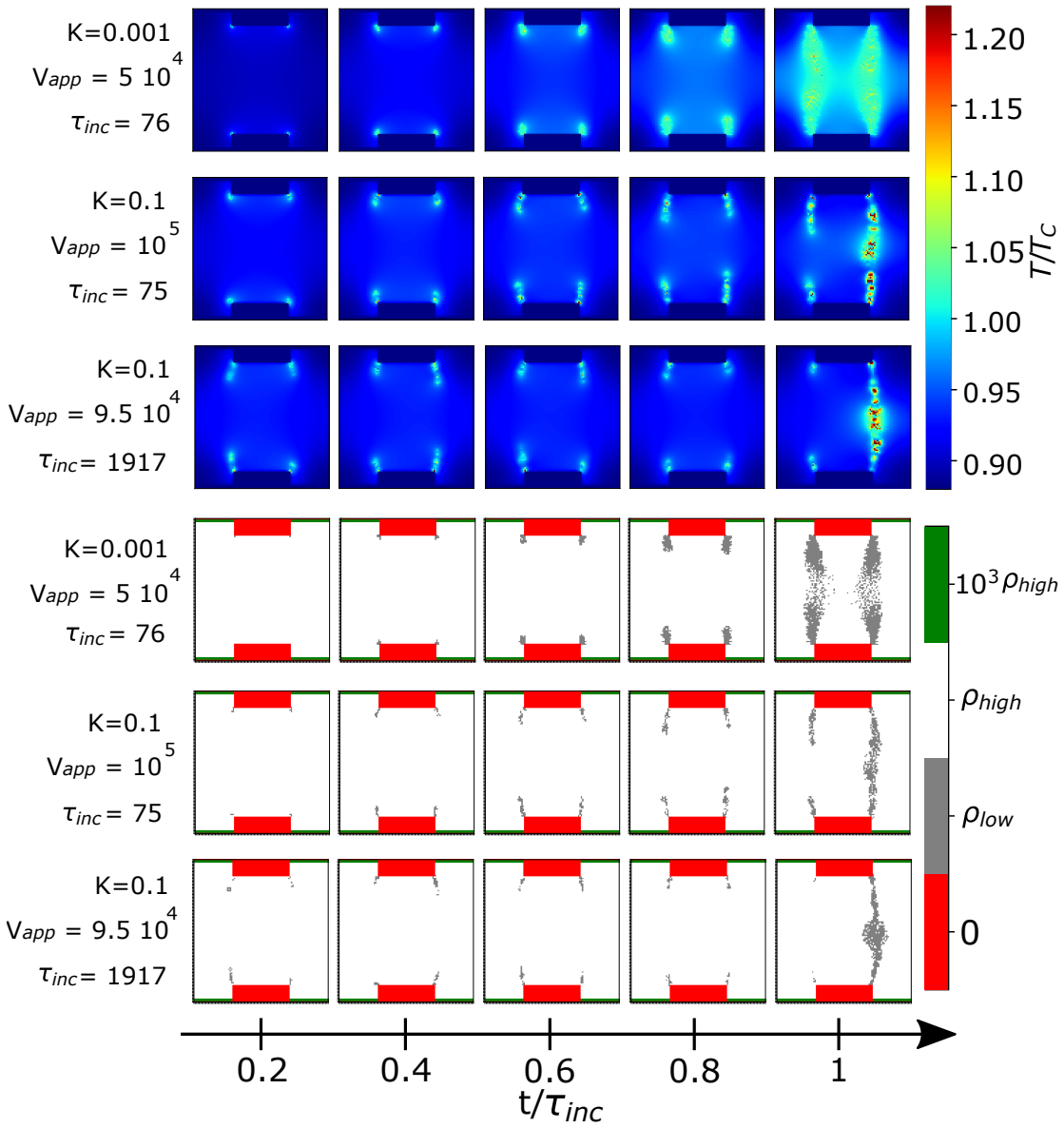

FIGURE 3.2 – Evolution of the temperature and resistivity maps of three different systems, one with small K in the thermal limit (top row, $\tau_{inc} = 76$ arb. units), and two with a large K in the electro-thermal limit (middle and bottom rows, with $\tau_{inc} = 75$ arb. units and $\tau_{inc} = 1917$ arb. units, respectively). The cases with high K differ in the value of the applied voltage : the bottom row is close to V_θ ($V_{app} = 9.5 \cdot 10^4$ arb.units), where the incubation times are highly stochastic, whereas the middle row is in the deterministic regime ($V_{app} = 10^5$ arb. units), which can be observed for high applied voltage in the incubation times curve of Fig.3.1. The panels capture snapshots of the state of the system as it progresses from the beginning of the filamentary formation up to the percolation, which corresponds to the resistive collapse of the system.

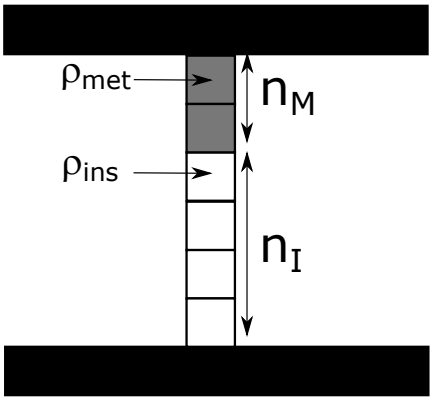

FIGURE 3.3 – Schematic one-dimensional representation of the formation of a metallic filament within the insulating bulk. If we assume that the formation may be described as a one-dimensional process, then the total resistance of the one-dimensional sample will be given by $R_{tot} = \rho_{met} n_M + \rho_{ins} n_I$, where n_M and n_I are the number of metallic and insulating cells, respectively. The voltage across gap is $V_{app}\rho_{ins} n_I / R_{tot}$ and since $\rho_{ins} n_I \gg \rho_{met} n_M$ it is approximately equal to the total applied voltage. In that case, the local voltage drop of the insulator cells will be V_{app}/n_I and will increase as the filament grows and the gap shrinks.

Fig.3.1). In this case we observe that, contrary to the previous case, the central part of the system remains relatively cold, since the thermal conductivity to the substrate is better. From the maps we also observe the symmetrical and continuous growth of thin filamentary structures that originate at the sharp edges of the electrodes. The narrow metallic filaments result from the current focusing effect, since a large current density needs to develop to maintain the temperature of the cells above T_{IMT} when K is sizable. We note that the length of those filamentary structure grows rather linearly with time. This linear progression is indicative of the deterministic behavior, that translates into the relatively small error bars in the respective incubation times (cf Fig.3.1).

In contrast to both previous cases, the third row of the panels of Fig.3.2 shows the stochastic behavior. Here K is relatively large and unchanged from the second row of panels, but the applied voltage is reduced to approach the threshold value. Consequently, the incubation time is now much longer. A significant difference, in sharp contrast with the previous case, is that the filaments do not grow lineraly with time but remain short stubs most of the time. Eventually, one of them breaks the symmetry and short-circuits the electrodes. This avalanche-like sudden percolation, which cannot be consistently predicted and is the source of the stochastic behavior, can be understood as follows. At low applied voltage the transition rate of the cell is relatively small, since most of the input power is dissipated to the sub-

strate. However, since a cell can switch to the metallic state even if its temperature is lower than the transition temperature (although with a very low probability) it may happen that the cell closest to the tip of the stub, where the temperature is hotter, will switch. It is important to stress that this is a chance event that might occur immediately after the application of the voltage, after a long time, or not occur at all, due to the very low probability of switching. However, if the cell does become metallic, the stub will get longer, and the insulating gap between the tip and the lower electrode smaller. If we assume that the applied voltage will mostly fall across such gap, due to the much higher value of the insulating resistivity, when the gap becomes smaller, the local voltage of the insulating cells will increase, thus raising the temperature and the probability of switching (see Figure 3.3 for more details). In this way a positive feeback loop is established, in which a hotter tip results in a longer filament, and thus a smaller gap and an even hotter tip. This positive feedback loop, which is initiated by a chance event, culminates in the avalanche-like percolation phenomenon, hence the stochastic nature of the resistive collapse.

In summary, the transition can have both a thermal and an electronic component. When heat dissipation is poor, the sample heats up homogeneously and gradually to the transition temperature, currents are not densely concentrated and the transition may be attributed mostly to Joule self-heating. On the other hand, better heat dissipation promotes the concentration of the electronic currents into thin metallic domains, resulting in stronger temperature gradients. In this case, if the applied voltage is big compared to the threshold, the input power overcomes the dissipation and the filaments grow linearly with time. However, at applied voltages close to threshold, the generated heat is comparable to dissipation, leading to long incubation times that have a strong stochastic behavior.

With these insights, we can look back at the incubation time data of VO_2 and V_2O_3 samples (right panel of Fig.3.1). We note that V_2O_3 has a larger voltage threshold and larger error bars. This is consistent with our simulations, and specifically the high thermal conductivity limit, in which stronger dissipation requires a higher applied voltage and can result in a more stochastic behavior. Therefore, V_2O_3 can be described as having a resistive collapse with a stronger electric component. In contrast, VO_2, with smaller threshold voltage and smaller error bars is relatively closer to the thermal paradigm, consistently with previous experimental reports [Kal+20 ; Zim+13 ; Val+18]. Nevertheless, the VO_2 data near the threshold still show a steep increase of incubation times and error bars that remain of the same order of τ_{inc}. This indicates that the electro-thermal effects also play a non-negligible role in the resistive collapse, as has been also reported in other previous experimental studies [GRR09 ; SPS00]. Thus, our present work sheds light on the long lasting debate on the nature of the electrically triggered resistive transition

in these materials, classifying VO_2 as a weak electro-thermal and V_2O_3 as a strong electro-thermal compound.

One might wonder if the experimental compounds have different thermal conductivities that could explain the different behaviors of the incubation times and, if not, what is the physical explanation for such difference. While in the simulations we have chosen the thermal conductivity as our control parameter, the two factors that determine whether the resistive collapse will be stochastic or not are Joule heating and current density concentration, the latter of which is not exclusively achieved through higher thermal conductivity. For example, in the case of the compounds used in our experiments, the thermal conductivity of the two samples was comparable, however V_2O_3 presented a ratio between the insulator and metal resistance two orders of magnitude greater than VO_2. A higher ratio results in a stronger concentration of current within the metallic domain, which can explain the more stochastic behavior, in accordance with our analysis. In the next chapter we will explore this possibility in more detail, showing how our theoretical results can be reproduced using the resistivity ratio as the control parameter instead of the thermal conductivity.

3.2 Probability distribution of resistive collapse

We now turn to another main result of our work, where we shall demonstrate that vanadium oxide Mott neurons are capable of stochastic spike emission as observed in biological neurons. This is a remarkable feature that constitutes an unexpected *neuromorphic functionality* of these quantum materials.

Biological neurons emit spikes with an intrinsic stochastic component even under constant stimulation [Ger+14]. This feature is commonly described in mathematical models of neurons by an Arrhenius-like instantaneous probability of firing or exponential escape rate [Ger+14 ; PG00 ; Jol+06] :

$$f(u-\theta) = \frac{1}{\tau_s} \exp\left[(u-\theta)/\delta u\right] \tag{3.4}$$

where u is the neuron's membrane potential, θ is the membrane threshold, δu is the width of the membrane potential spike emission zone and τ_s is the mean time to spike emission at threshold [Jol+06]. From this mathematical expression, we can derive the probability $P(u, \Delta t)$ for the emission of a spike within a time window of duration Δt, when the potential is kept fixed at u. We shall show that the resulting probability also describes the probability of resistive collapse both in our Mott Resistor Network model and also in experiments done on a vanadium dioxide device.

The probability may be derived using the formalism of the survivor function and renewal theory [Ger+14]. Renewal theory describes the probability $P(t|\tilde{t})$ that an event, characterized by a stochastic intensity $\rho(t|\tilde{t})$ (also known as hazard function), will occur at time t given that the last occurrence was at time $\tilde{t}$. The firing of a neuron can be described as a renewal process if we assume that the probability of firing does not depend on the spike train but only on the time since the last spike. We notice that we cannot simply compute the probability that the neuron should fire in a time interval Δt by integrating $\rho(t|\tilde{t})$ in said interval :

$$P(\Delta t) = \int_0^{\Delta t} \rho(t|0)dt \tag{3.5}$$

since $P(\Delta t)$ is not bounded by one. The proper approach to obtain this probability is to recur to the survivor function [Ger+14]. We define the survivor function $S(\Delta t)$ as the probability that the neuron will survive for a time Δt without firing :

$$S(\Delta t) = 1 - P(\Delta t) \tag{3.6}$$

We know for sure that, at time zero, the survivor function is equal to 1, and as time goes to infinity, since the probability of firing inevitably goes to 1, the survivor function goes to 0. Consequently, the survivor function decays proportionally to the rate at which the neuron attempts to fire, which defines the stochastic intensity :

$$\rho(t|0) = -\frac{dS(t)/dt}{S(t)} \tag{3.7}$$

Integration of this equation yields :

$$S(\Delta t) = \exp\left[-\int_0^{\Delta t} \rho(t|0)dt\right] \tag{3.8}$$

The survivor function can be put back into equation (3.6) to obtain the probability that the stochastic event will occur in a finite time interval. In our case the event is the firing of a noisy neuron, therefore the stochastic intensity takes the form of the instantaneous firing probability $f(u(t) - \theta)$:

$$\begin{aligned} P(\Delta t) &= 1 - \exp\left[-\int_0^{\Delta t} f(u(t) - \theta)dt\right] = \\ &= 1 - \frac{1}{\exp\left[\int_0^{\Delta t} f(u(t) - \theta)dt\right]} \end{aligned} \tag{3.9}$$

If we assume that $u(t)$ stays constant in the interval Δt, which is the case if $u(t)$ represents the voltage applied to the Mott device before the resistive transition

occurs, then the integral may be approximated as the product of the integrand times the interval, i.e., $\Delta t\ f(u-\theta)$

$$P(u,\Delta t) = 1 - \frac{1}{\exp\left[\Delta t f(u-\theta)\right]} \tag{3.10}$$

To simplify this expression, we may expand the exponential to the first since we know already that, for $\Delta t \gg 0$ or $u \gg \theta$, where the expansion would not be justified, the probability approaches unity anyway. Thus, we get :

$$P(u,\Delta t) \approx 1 - \frac{1}{1+\Delta t f(u-\theta)} \tag{3.11}$$

Finally, substituting the instantaneous firing probability $f(V-V_\theta) = \frac{1}{\tau_s}\exp[(u-\theta)/\delta u]$ in the equation yields the functional form :

$$P(u,\Delta t) \approx 1 - \frac{1}{1+\frac{\Delta t}{\tau_s}\exp[(u-\theta)/\delta u]} \tag{3.12}$$

A connection with the MRN model and with experiments in Mott devices can be established by identifying the parameters of $P(u,\Delta t)$ as follows : The membrane potential u can be associated with the applied voltage V. The parameters δu and θ respectively become the fitting parameters δV and V_0. Finally, we take the microscopic time τ_s as equal to the time-step, which is the unit of time for the model simulations. Thus, we shall adopt as the fitting functional for the probability of filament formation within a time window Δt at applied voltage V the expression :

$$P(V,\Delta t) \approx 1 - \frac{1}{1+\Delta t\exp[(V-V_0)/\delta V]}. \tag{3.13}$$

From this expression we may provide a proper definition of the firing voltage threshold, for a given arbitrary time window Δt. We call this quantity the stochastic threshold $V_S(\Delta t)$, which we define as the voltage value where the probability of incubating a filament is $1/2$, i.e. $P(V_S,\Delta t) = 0.5$. Then, from Equation (3.13) we obtain :

$$V_S(\Delta t) = V_0 - \ln(\Delta t)\delta V \tag{3.14}$$

Since Δt is in units of time-step, it can't be smaller than $\Delta t = 1$ and thus the logarithm is always greater than zero. In Fig.(3.4), we show $P(V)$ for both the numerical simulations of the MRN model and experiments on a VO_2 device at room temperature. In this figure, $P(V)$ is the probability of observing the resistive collapse as a function of a constant applied voltage V, for different time windows Δt. The figure also shows how, in both cases, the probability expression derived

above provides an excellent fit for the data. Interestingly, we also observe in the small panel of the figure that the behavior of $V_S(\Delta t)$ and δV closely track each other. We note that the latter is two orders of magnitude larger than the threshold voltage. This follows from the fact that δV characterizes the voltage transition range of a single cell, while V_S is the voltage applied between the electrodes. Since the distance between electrodes is L=100, the voltage drop on a single cell is of the order of V_S/L. We may further argue that since $V_S(\Delta t)$ characterizes the typical voltage value that induces a firing event in the time window T and δV the range of its stochastic behavior, then the underlying reason for the codependency is that the filamentary percolation, just like the firing event of spiking neurons, is a stochastic point process described by a Poisson distribution, which has the property of the mean being equal to its variance.

One final important observation is that our results also clarify the debated issue of the threshold voltage. In fact, in previous experimental work the problem of precisely determining the threshold voltage was already evident [Val+19]. This lack of precision was assumed to be caused by some source of experimental uncertainty. However, we now see that the dramatic enhancement of the error bars in the determination of the long incubation times at threshold is not an artifact but an intrinsic feature of the stochastic physical process of filamentary formation in Mott systems.

3.3 Conclusion

In this chapter we have shown that the field-driven resistive transition in Mott insulators is triggered by the formation of metallic filaments within the insulating bulk, to which both thermal and electronic effects, in the form of Joule self-heating and electronic currents concentration, contribute. We have also shown that this process is highly stochastic and is affected by the magnitude of the applied voltage, and therefore the Joule heating effect, and by the density of electronic currents, which in our simulation we control via the thermal conductivity. In particular, a small thermal conductivity results in a comparatively homogenous and deterministic transition, whereas a higher thermal conductivity produces stronger temperature gradients and increasingly stochastic incubation times as the applied voltage is lowered.

Our Mott Resistor Network model simulations are validated by comparison to data from experiments on devices based on the Mott compounds VO_2 and V_2O_3. The analysis of the behaviour of the incubation times allowed us to characterize the resistive collapse in VO_2 and V_2O_3 as weak and strong electro-thermal, respectively, clarifying a longstanding debate.

Another significant result of the present work was to go beyond the qualitative

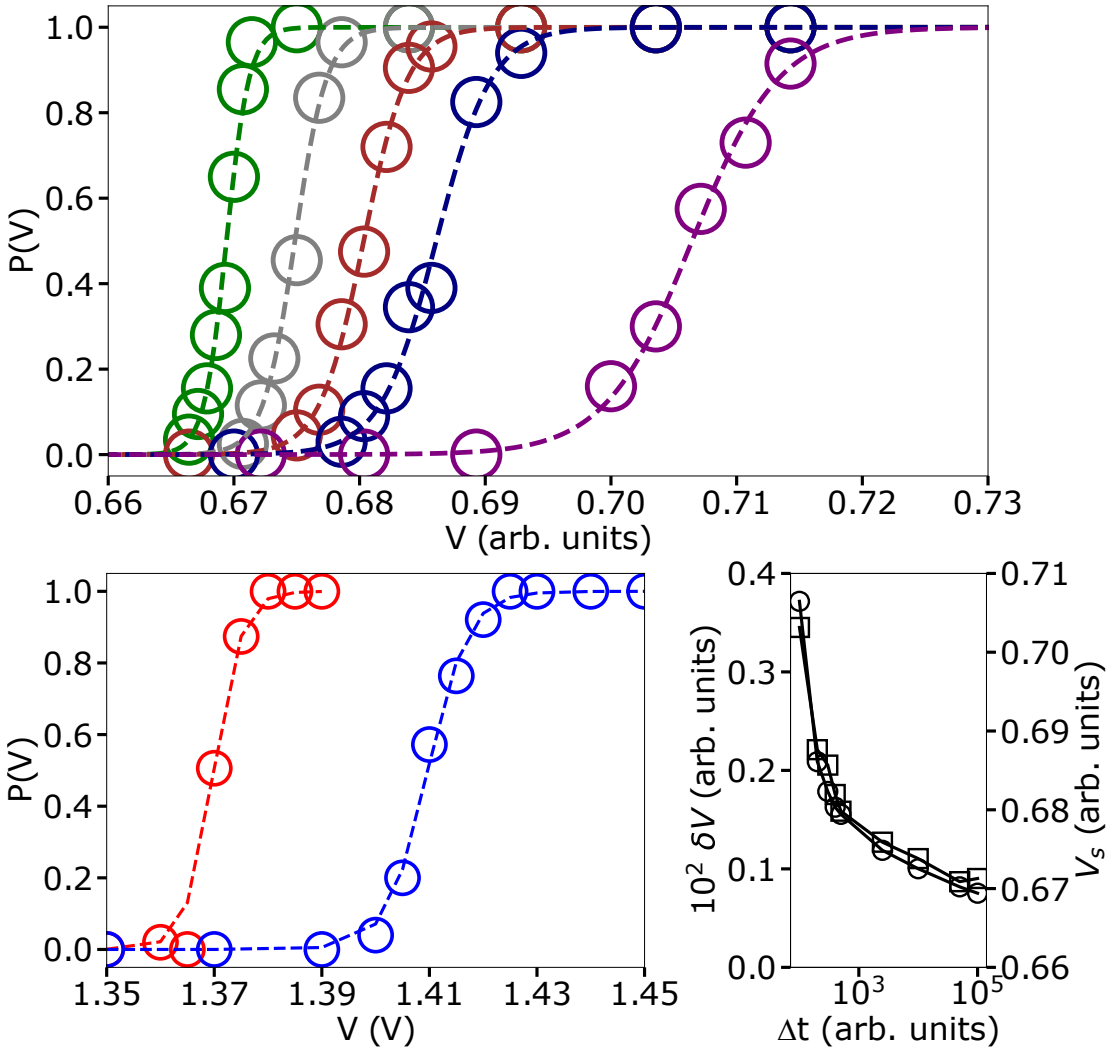

FIGURE 3.4 – The top panel shows the simulation results for the probability distribution of filament percolation for $K = 0.1$ arb. units and different values of the pulse width $\Delta t = 10^5$, $5 \cdot 10^4$, 2500, 400 and 100 arb. units from left to right. Voltage values are normalized by $V = 1.4 \cdot 10^5$ arb. units and for each point the total number of trials was 200. The fits were done using Eq. (3.13). The bottom left panel is the probability distribution obtained experimentally from a VO_2 sample, for two different pulse widths of $\Delta t = 10\ \mu s$ (red curve) and $\Delta t = 1\ \mu s$ (blue curve) and a substrate temperature of $T = 300$K. For the experimental details of the setup see Fig.2.3. The bottom right panel shows δV and V_S, the parameters of the fit to the simulation data in the top panel, evolve for different pulse widths. The fits to the experimental data were also done with Eq. (3.13) and the parameters are : $V_0(10\mu s) = 1.375$, $V_0(1\mu s) = 1.409$, $\delta V(10\mu s) = 0.002$ and $\delta V(1\mu s) = 0.003$. The size of the circles is comparable to the estimated binomial confidence intervals. When measuring the experimental probability of resistive transition, a resistive termination of 50Ω was added to the function generator of Figure 2.3

description of the filamentary formation, to demonstrate that its stochastic behavior is characterized as a Poisson process. This is a remarkable finding, since spike emission in biological neurons can also be described as Poisson process. In fact, the probability distribution of the filament formation that we obtained and observed follows the same stochastic form as the spike emission in models of neurons with an exponential escape rate.

Chapitre 4

Tuning stochasticity with the resistivity ratio

In the previous chapter we explored the stochastic percolation of metallic filaments within Mott insulators such as VO2 and V2O3 under a constant applied electric field. The MRN model allowed us to study the percolation with greater temporal resolution than that achievable in experiments. In so doing we were able to conclude that both thermal and electronic contributions, in the form of Joule heating and current density concentration, affect the resistive switching phenomenon. In particular we established that the stochastic character of the resistive transition emerges whenever the currents are densely concentrated in thin metallic domains and the input power is comparable to the thermal dissipation of the substrate. In our theoretical study such conditions could be achieved by increasing the thermal conductivity of the sample K.

Next, we explore another way of controlling current density concentration, and thus the stochastic nature of the transition, by tuning the ratio between the resistivity of the insulating and metallic phase. A high resistivity ratio leads to high current density within the filamentary metallic domains and an inhomogenous resistive transition. This result finds confirmation in experiments conducted on VO2 and V2O3, showing that the latter, which has a higher resistitivity ratio by a factor of 10^2, also present a more stochastic resistive switching, as evidenced by the incubation times curve[Del+21].

We also explore the growth of the metallic domains after the resistive collapse. The resistive collapse produces a surge in the current, which is now confined within the thin metallic domains ; this lead to a substantial production of heat and the exponential growth of the metallic domains [Del+21]. We show that the results of our simulations are in qualitative agreement with optical reflectivity measurements done on a VO2 sample

Finally, we extend our modelling work to the nickelates, introucing a tempera-

ture dependent insulating resistivity. By changing the temperature of the sample it is thus possible to also change the initial resistivity. Therefore, we show that a more inhomogenous transition, characterized by stronger current concentration and temperature gradients, can be achieved in our MRN simulations not only by changing the resistivity ratio, but also by changing the initial temperature of the sample, while keeping the base insulating resistivity fixed. This results is confirmed by experiments conducted on two members of the nickelates family, SmNiO3 and NdNiO3, in which the resistive collapse is triggered by application of a constant electric field and for different initial temperatures [Val+21]. By measuring the current that flows through the sample, we establish that decreasing the temperature results in a more abrupt switching behaviour as the applied voltage is lowered, which is consistent with our model predictions, and with our previous study of the incubation times in V2O3 and VO2.

4.1 Variability of incubation times

In the previous chapter we explored the stochastic behaviour of the incubation times for different values of the thermal conductivity K. This allowed us to control in our simulations the character of the metallic domains formation : more homogenous and thermal-like for vanishing K, which resulted in incubation times that could be predicted consistently even for an applied voltage approaching the theshold value (as demonstrated by our analytic fit) ; filamentary at higher K values, which produced highly variable incubation times when the input power was comparable to the dissipation. These predictions can be put to test by engineering different substrates. Two most common substrates for growing VO2 thin films are Al_2O_3 and TiO_2. Thermal conductivity of Al_2O_3 is ≈ 25 W/(mK), which is much larger compared to the thermal conductivity of TiO_2 (≈ 5 W/(mK)). Therefore, according to our model, the switching of VO2 grown on Al_2O_3 should display much more prominent stochastic behavior compared to the VO2 prepared on TiO_2. We note that with the recent progress of synthesis and transfer of nano-membranes [Lee+21], high quality VO2 films could be integrated with virtually any substrate. Using such nano-membrane approach, it is possible to test our model at extremes, for example, synthesizing VO2 on a sulfur crystal (thermal conductivity ≈ 0.2 W/(mK) resulting in deterministic switching) or on diamond (thermal conductivity ≈ 2000 W/(mK) resulting in stochastic switching). From the practical point of view, the switching in VO2 integrated with a pure silicon substrate, thermal conductivity ≈ 100 W/(mK), should be rather stochastic, while the switching in VO2 on SiO_2, thermal conductivity ≈ 1 W/(mK), should be nearly deterministic.

The topic of substrate engineering being outside of the scope of this work, we put to test the predictions of our model by exploring the nature of the resistive

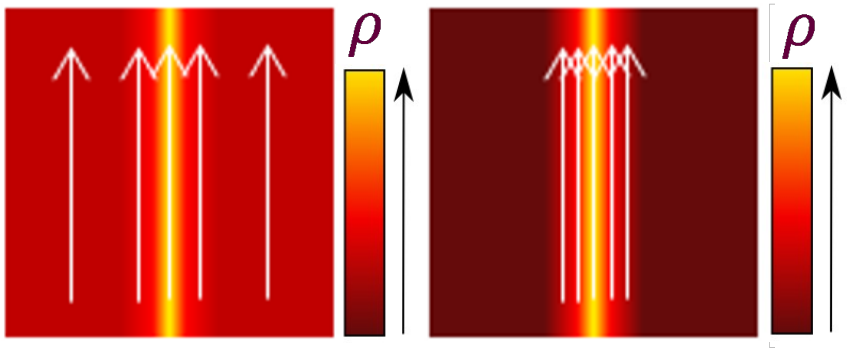

FIGURE 4.1 – Schematic representation of the effect of different resistivity ratio on the concentration of electronic currents. Left : the ratio between the resistivity of the insulator and correlated metal states is smaller. This allows the current to fan out from the injection point and disperse rather homogeneously in the bulk. Right : the higher resistivity ratio confines the current within smaller domains. Adapted from [Val+21]

collapse in materials that present different ratios of the insulating and metallic resistivity. Indeed, from our previous study of the effect of the thermal conductivity on the transition, we know that the difference between a transition that presents variable incubation times and one that is deterministic lies in how densely the electronic currents are concentrated, i.e. whether the sample will reach the transition temperature homogeneously or it will develop thin filamentary structures. Our working hypothesis will be that, for bigger ratios of the resistivity of the insulator and correlated metal state, the currents will be more strongly concentrated (see Figure 4.1 for a schematic representation) and will produce a more stochastic transition, characterized by greater variability in the incubation times as the applied voltage is lowered ; for smaller resistivity ratios, the currents will fan out from the cell at the edge of the electrode, the transition will be comparatively homogeneous and the incubation times not as variable as before. We test our hypothesis first in our MRN simulations and then in experiments conducted on V2O3 and VO2, the former having a resistivity ratio two orders of magnitude greater than the latter ($\approx 10^5$ vs $\approx 10^3$, see Figure 4.2).

To study the effect of the resistivity ratio on the variability of the incubation times, we may look at Figure 4.3, in which the incubation times are plotted against the normalized applied voltage for two resistivity ratios.

From this figure we can see how the red curve, obtained for a resistivity ratio of $\rho_{ins}/\rho_{met} = 2.7\ 10^5$ (for all the other parameters, see Table 4.1), is steeper and presents incubation times with bigger standard deviation than the blue curve,

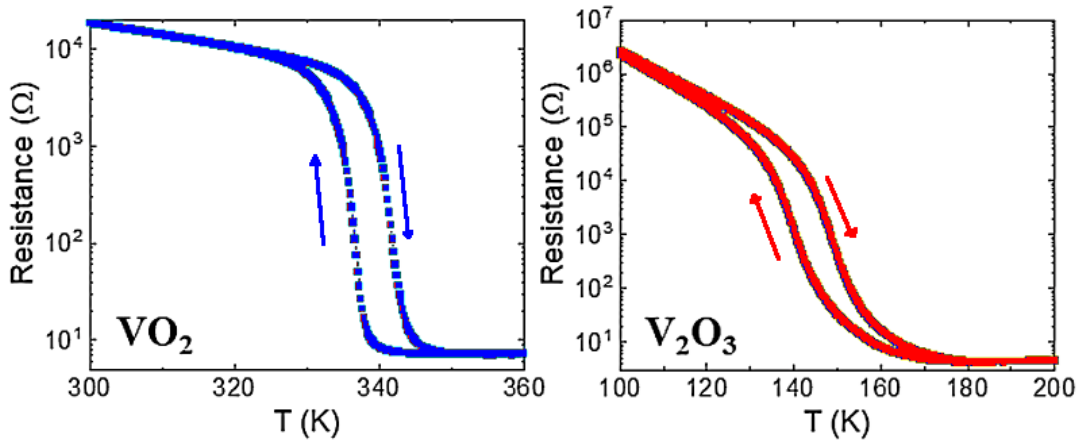

FIGURE 4.2 – Experimental resistive collapse and subsequent relaxation to the initial insulating state of a VO2 and a V2O3 sample, obtain by changing the temperature of the sample. A minimal electric field was applied to probe the resistance. Adapted from [Del+21]

Parameter	Value
h_1	71.25 10^3
h_2	7.5 10^3
p_1	15.0 10^3
c	3.0 10^2
T_C	380.0
T_{IMT}	340.0
T_0	300.0
ρ_{ins}	$[10^3, 2.7\ 10^5]$
ρ_{met}	1
R_L	5 10^2
C	1
W	100
W_e	20
L	106
K	0.01

TABLE 4.1 – Values of the parameters used in the simulations of the incubation times and temperature maps for different values of ρ_{high}

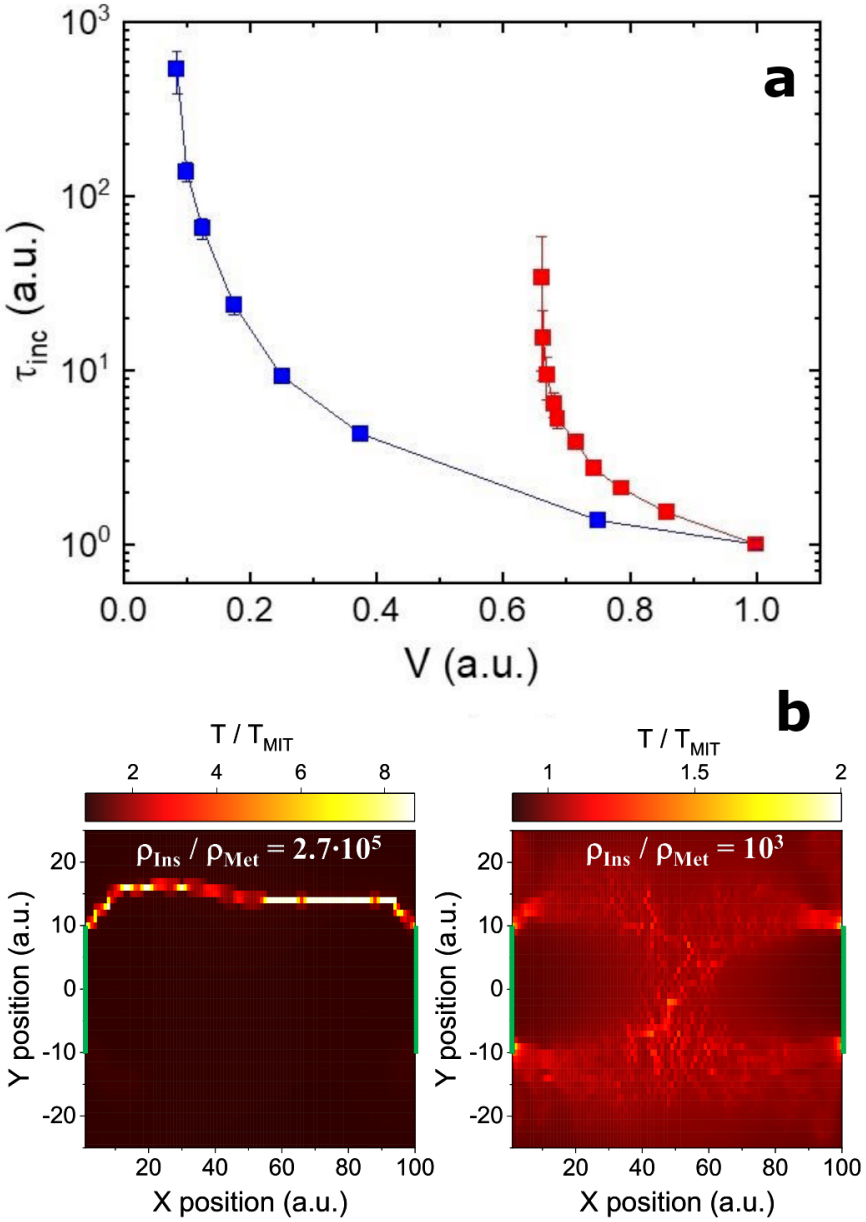

FIGURE 4.3 – Simulation results for different resistivity ratios. Panel a) : incubation times against applied voltage, $\rho_{ins}/\rho_{met} = 2.7\ 10^5$ for the red curve and $\rho_{ins}/\rho_{met} = 10^3$ for the blue one. The applied voltage in both cases has been normalized by the highest value in the respective curve to allow for direct comparison. Panel b) : temperature maps when the resistance collapses for $\rho_{ins}/\rho_{met} = 10^3$ (right) and for $\rho_{ins}/\rho_{met} = 2.7\ 10^5$ (left). Adapted from [Del+21]

which was obtained for a resistivity ratio of $\rho_{ins}/\rho_{met} = 10^3$. These numerical results are consistent with the experimental findings (right panel of Figure 3.1), in which VO2, which has a resistivity ratio $\approx 10^3$, is characterized by a less pronounced stochastic behaviour and a smother dependence on the applied voltage than V2O3, which has a resistivity ratio $\approx 10^5$. Moreover, they are also consistent with the incubation times curves obtained previously by changing the thermal conductivity K (left panel of Figure 3.1), indicating that current density concentration, and thus stochastic filament percolation at low applied voltage, may be achieved either by a strong ratio of the insulator to metal resistivity, or strong dissipation to the substrate. Finally, we also notice that the temperature map produced by the simulations for a high resistivity ratio is much more inhomogenous than that obtained at a lower ratio, and is characterized by the presence of a thin metallic filament (Figure 4.3). This is in complete analogy with the temperature maps obtained when increasing the thermal conductivity, which go from being relatively homogeneous to having strong temperature gradients due to the presence of filamentary metallic structures (see Figure 3.2).

In the next section we turn our attention to the growth of the metallic domains after the resistive collapse, to see how it is affected by different resistivity ratios in both experiments and simulations.

4.2 Filament growth after the resistive collapse

In the preceding sections we have studied how the resistivity of the sample can affect the incubation times and the temperature gradients leading up to the collapse of the resistance. Now we turn our attention to the expansion of the metallic domains after the resistance has collapsed. We start with the experimental results shown in the top panels of Figure 4.4. Here a map of the reflectivity of the sample is presented, in which the x-axis represents the duration of the applied voltage pulse and the y-axis the spatial coordinate that runs parallel to the electrode (the dashed white lines indicate the edges of the electrodes). The map has been obtained as follows [Del+21] : a beam laser with a wavelength of 660 nm was pointed at the VO2 sample and focused down to a spot of 3 μm. The power of the laser is around 1 mW, most of which is lost when the beam is focused. Hence, we can exclude the possibility that the temperature of the sample might be affected by the laser. A photodiode is used to capture the reflected beam. Additionally, a system of computer controlled deflecting mirrors allows to translate the laser along the y-axis (for a schematic repesentation of the setup see Figure 2.1). As before, the resistive collapse is induced by applying a constant electric field. The normalized reflectivity which is used in the figure has been computed as

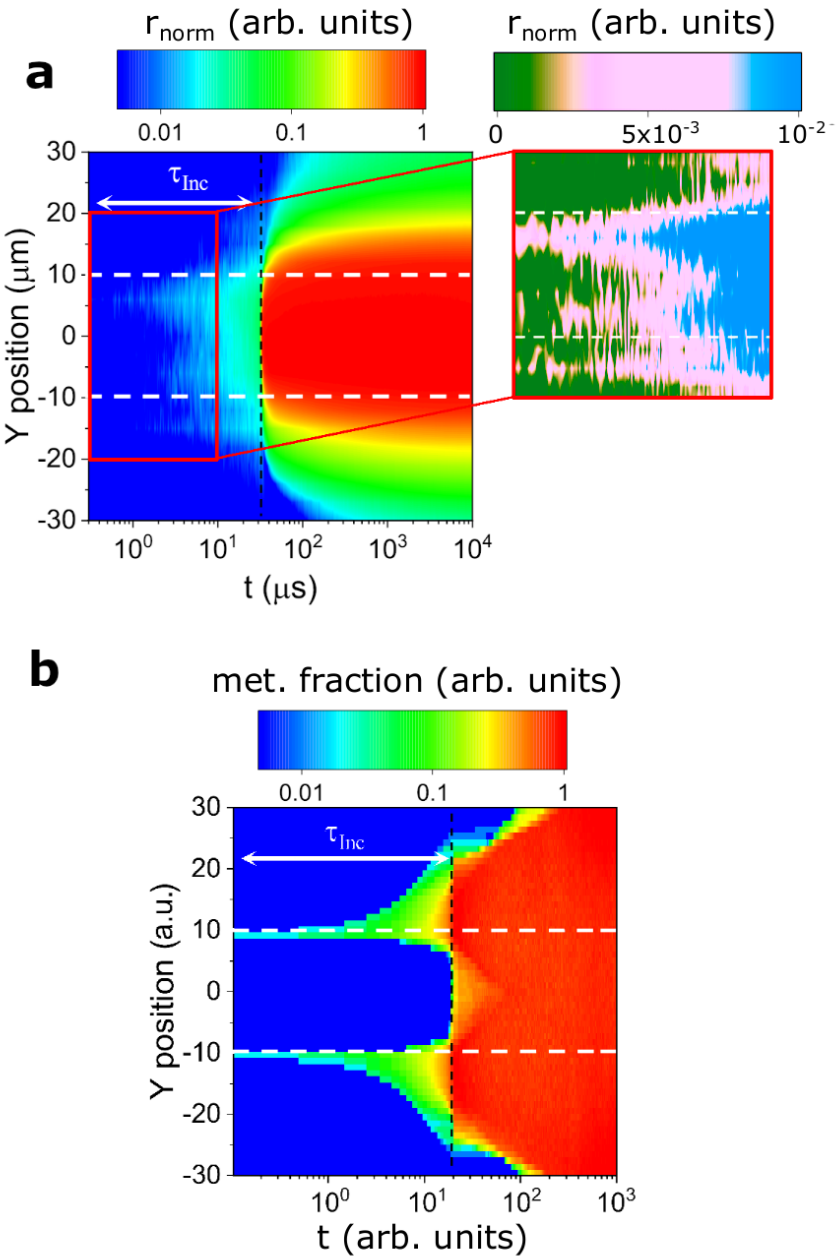

FIGURE 4.4 – Panel a) : Temporal evolution of the reflectivity of a VO2 sample. A voltage of 12 V is applied to the sample, which is in contact with a substrate at a temperature of 335 K, and a laser beam with a wavelength of 660 nm is pointed at the sample. While the voltage is kept on, the laser is translated along the y direction, and the reflected beam is measured by a photodiode. The reflectivity is normalized according to Equation 4.1. The white dashed lines indicate the edges of the electrode, the black dashed line the moment when the collapse of the resistance occurs. Inset : Zoomed in reflectivity map. Panel b) : Temporal evolution of the metallic fraction of a simulated sample. The metallic fraction for a given y coordinate is defined as the fraction of cells with that coordinate which are in the metallic state. Time scales in all panels are logarithmic. We notice that the simulations do not include metallic defects. Adapted from [Del+21]

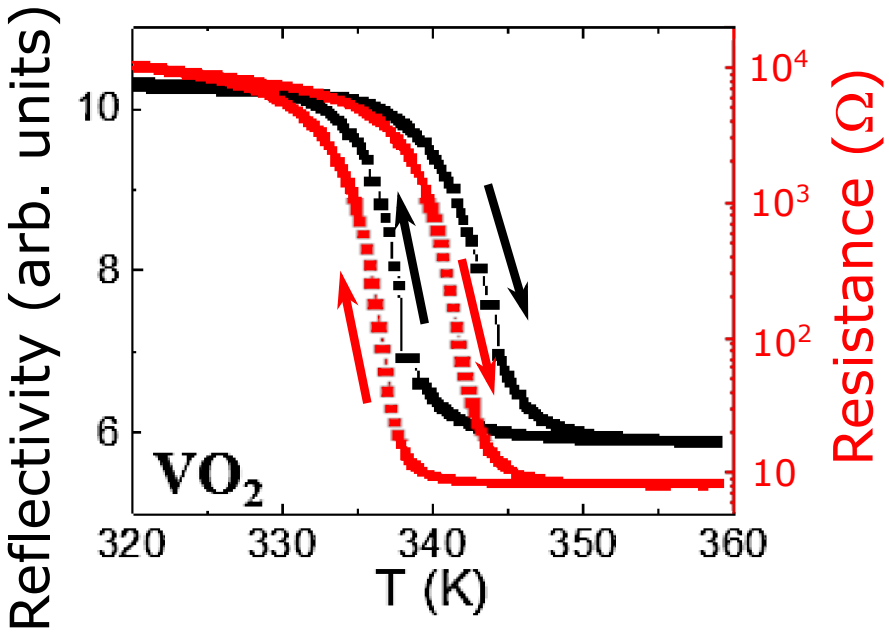

FIGURE 4.5 – Comparison of the resistance (red) and the reflectivity (black) of a VO2 sample (defined in Equation 4.1) as it's being heated up via thermal contact with the substrate. A minimal voltage is applied to probe the resistance. Adapted from [Del+21]

$$r_{norm} = \frac{r - r_{ins}}{r_{met} - r_{ins}} \tag{4.1}$$

where r is reflectivity, measured as the square of the ratio of the amplitude of the reflected beam and the incident beam, and r_{ins} and r_{met} are the reflectivity of the low temperature insulator state and the high temperature metal state, respectively (see Figure 4.5 for a measure of these two quantities in VO2). Since the measured reflectivity correlates to the resistivity of the region of the sample where the beam was focused, as evident from Figure 4.5, it is possible to study how the metallic domains grow by looking at the reflectivity map of Figure 4.4.

We notice that, at first, the normalized reflectivity is higher near the edges of the electrode (which in the figure are indicated by dashed white lines), meaning that in that region the sample is becoming hotter and more metallic. This is particular evident in the top right panel, in which we present a zoomed in section of the reflectivity map. This observation is consistent with our previous findings, i.e. that the increased electric field near the edges of the electrodes, due to the point effect, results in higher temperatures and thus a higher transition rate of the insulating cells. After 30 μs approximately, the resistive collapse occurs, as

indicated by the black dashed line, and with it a surge in the current that flows through the sample. The increased current is confined within the thin metallic domains, which leads to very high temperatures due to the Joule heating effect. The heat cannot be efficiently dissipated to the substrate, and therefore spreads to the insulating bulk, thus promoting the expansion of the metallic domain that can be appreciated from the reflectivity measurements.

These observations find confirmation in the map of the metallic fraction produced by our simulations, which is presented in the bottom panel of Figure (4.4). The metallic fraction for a given y coordinate is defined as the fraction of cells with that coordinate which are in the metallic state. It is therefore a measure of the degree to which a given slice of the sample has become metallic, in analogy with the experimental normalized reflectivity as described above. In our simulated map we see once again that the sample at first becomes metallic near the edges of the electrodes. Until the collapse of the resistance the metallic fraction does not increase substantially, nor do the metallic domains grow in width. Eventually though the metallic domain short-circuits the electrode, triggering the collapse of the resistance and a sudden surge in the current. In turn, the increased current further raises the temperature of the metallic domains, promoting the transition of the neighbouring insulating cells and thus the observed exponential growth.

4.3 The nickelates case

So far we have focused our attention on vanadium oxides, particularly VO2 and V2O3, which are among the most studied materials in the literature [SPS00; Kim+04; Bro+14; Del+21]. However, it is worth asking oneself if the generality of the MRN model allows to cover other cases, what modifications to the model might be required and, most importantly, if the results that have been found so far are applicable to these new materials. This is exactly what we do in this section, examining two members of the nickelates family : NdNiO3 and SmNiO3 [Tor+92; Med97; Cat+18]. Like before we induce the resistive switching by applying an electric field, and we use the MRN model to study the phenomenon. In particular, we study the effects of a change in the resistivity of the material and in its starting temperature, and we find that bigger resistivity ratios focus the current into thinner metallic domains and produce stronger temperature gradients, as was the case for the vanadium oxides [Val+21].

We begin by studying the experimental resistivity versus temperature curve of the two materials under consideration (Figure 4.6), and observing that they both present a strong dependence of the resistivity of the insulator state on the temperature. For this reason we decide to modify our model so that the insulating resistivity of a given cell should change with the temperature of the cell, according

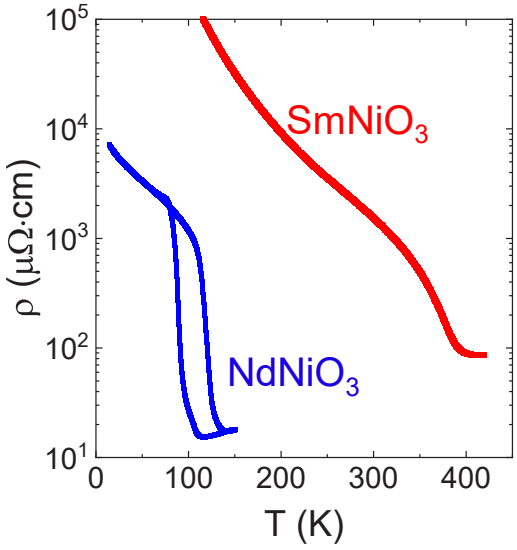

FIGURE 4.6 – Comparison of the resistivity of SmNiO3 and NdNiO3. Adapted from [Val+21]

to the following activation law [CBG00] :

$$\rho_{ins}(T) = \rho_0 e^{\Delta\left(\frac{1}{T}-\frac{1}{T_C}\right)} \tag{4.2}$$

where ρ_0 is a constant equal to the insulating resistivity at the transition temperature, T_C the transition temperature of the material and Δ is also constant. Experimental measurements of the resistivity in NdNiO3 and SmNiO3, such as the ones presented in Figure 4.6 (we notice here that the resistivity scale is logarithmic), allow us to appreciate the temperature dependence of the insulating resistivity. We should stress that the transition of the cell to the metallic state remains a thermally activated process with an Arrhenius-like probability, as per Equation 2.11, regardless of the fact that now the insulating resistivity is temperature dependent.

We begin by examining the effect of different resistivity ratios on the temperature and resistivity maps produced by our simulations. Since the insulating resistivity is temperature dependant, there are two ways of increasing the resistivity ratio : either by changing the substrate temperature, and thus the initial temperature of the simulated sample, or by changing the base value of the insulating resistivity, i.e. ρ_0. The metallic resistivity, as well as the Δ parameter of Eq. 4.2, are always kept constant ; all the parameters used for the simulations presented in this section are summarized in Table 4.2. We start by examining the case in which the substrate temperature is kept constant and ρ_0 is changed. From our

Parameter	Value
h_1	$71.25\ 10^3$
h_2	$7.5\ 10^3$
p_1	$15.0\ 10^3$
c	$3.0\ 10^2$
T_C	380.0
T_{IMT}	340.0
T_0	$[64, 120, 300]$
ρ_0	$[10^1, 10^2, 10^3]$
ρ_{met}	1
Δ	650
R_L	$5\ 5\ 10^2$
C	1
W	100
W_e	20
L	103
K	0.01

TABLE 4.2 – Values of the parameters used to obtain the temperature and resistivity maps presented in this section. In the comparison of the maps for different ρ_0, the substrate temperature was kept fixed at $T_0 = 64$. In the comparison in which the substrate temperature changes, ρ_0 was kept fixed at $\rho_0 = 10^2$

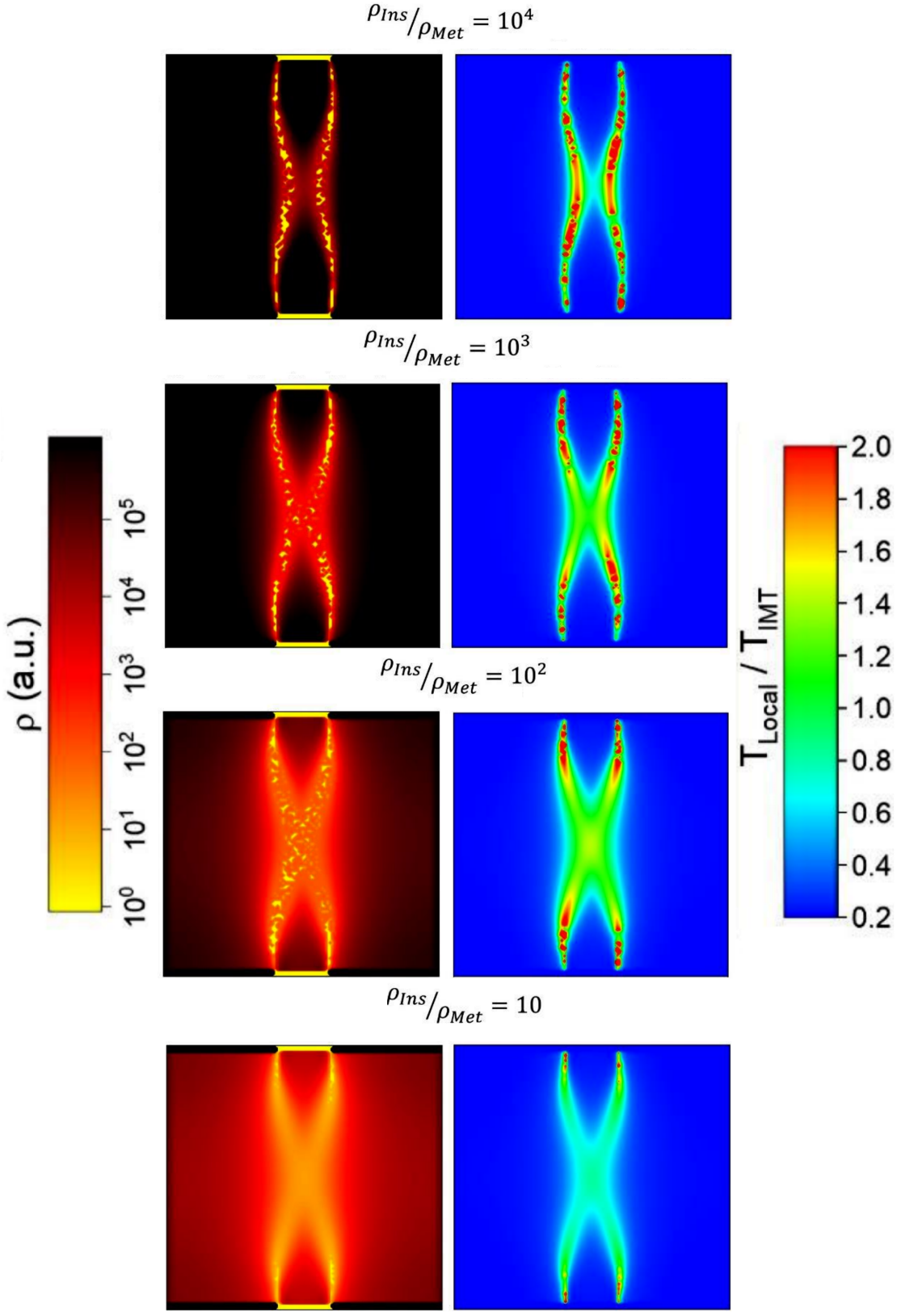

FIGURE 4.7 – Temperature and resistivity maps produced by the simulations for different values of the resistivity ratio. Here the ratio is to be intended between the base insulating resistivity ρ_0 of equation 4.2 and the metallic resistivity, which is independent of the temperature. All simulations were done keeping the substrate temperature constant at $T_0 = 64$. Adapted from [Val+21].

previous study of the resistive switching phenomenon in vanadium oxides, we'd expect higher resistivity ratios to result in stronger temperature gradients and more filamentary metallic structures. This is precisely the case, as shown by Figure 4.7. Here we notice that the resistivity maps present smooth gradients, unlike before when were simulating the vanadium oxides, due the temperature dependence of the insulating resistivity that we introduced. As the resistivity ratio is increased, we see that both the temperature and resistivity maps become less homogeneous, as expected, and that the metallic domains become thinner and hotter as well, due to the increase in current density.

Up to now the substrate temperature has been kept constant. However, it should be possible to reproduce the results obtained above, for a fixed value of ρ_0, by changing the temperature substrate from trial to trial. Indeed we know that both SmNiO3 and NdNiO3 present a strong temperature dependence of the resistivity in the insulating state. Since the materials are in thermal equilibrium with the substrate at the beginning of the simulations, by changing the substrate temperature we also change the temperature of the materials, and thus their starting resistivity. Therefore, we expect that, as the substrate temperature is decreased, we should obtain increasingly inhomogenous temperature maps and filamentary metallic structures. This is precisely the case, as shown in Figure 4.8.

We now turn our attention to the experimental results, to check consistency with our simulations. From our previous study of the vanadium oxides we know that materials which present a more inhomogenous resistive transition, like for instance V2O3 with respect to VO2, also feature a curve of the incubation times against the applied voltage that look steeper. Therefore, to verify that lower temperatures induce a more inhomogenous transition in the nickelates, we measured the electric current that flows through the sample at different values of the applied voltage and for the same initial temperature. From these measurements we computed the incubation time as the delay between the application of the voltage and the moment the current sharply increases (as an effect of the collapse of the resistance). We then repeated the same experiments for a different starting temperature. The data for NdNiO3 is shown in Figure 4.9, that for SmNiO3 in Figure 4.10. In both materials we observe that, for a given temperature, incubation times become longer when the applied voltage is decreased, since less power is being produced and thus more time is required to heat up the sample. We also see that, if the starting temperature is increased, the samples exhibit a resistive collapse even for applied voltages that had failed to induce it at lower temperatures. This can be easily explained as an effect of the temperature dependence of the insulating resistivity. If the starting temperature is higher, the resistance of the sample in the insulating state will be lower, and thus a smaller applied voltage is required to heat up the sample and make the resistance collapse. Finally, we also notice that

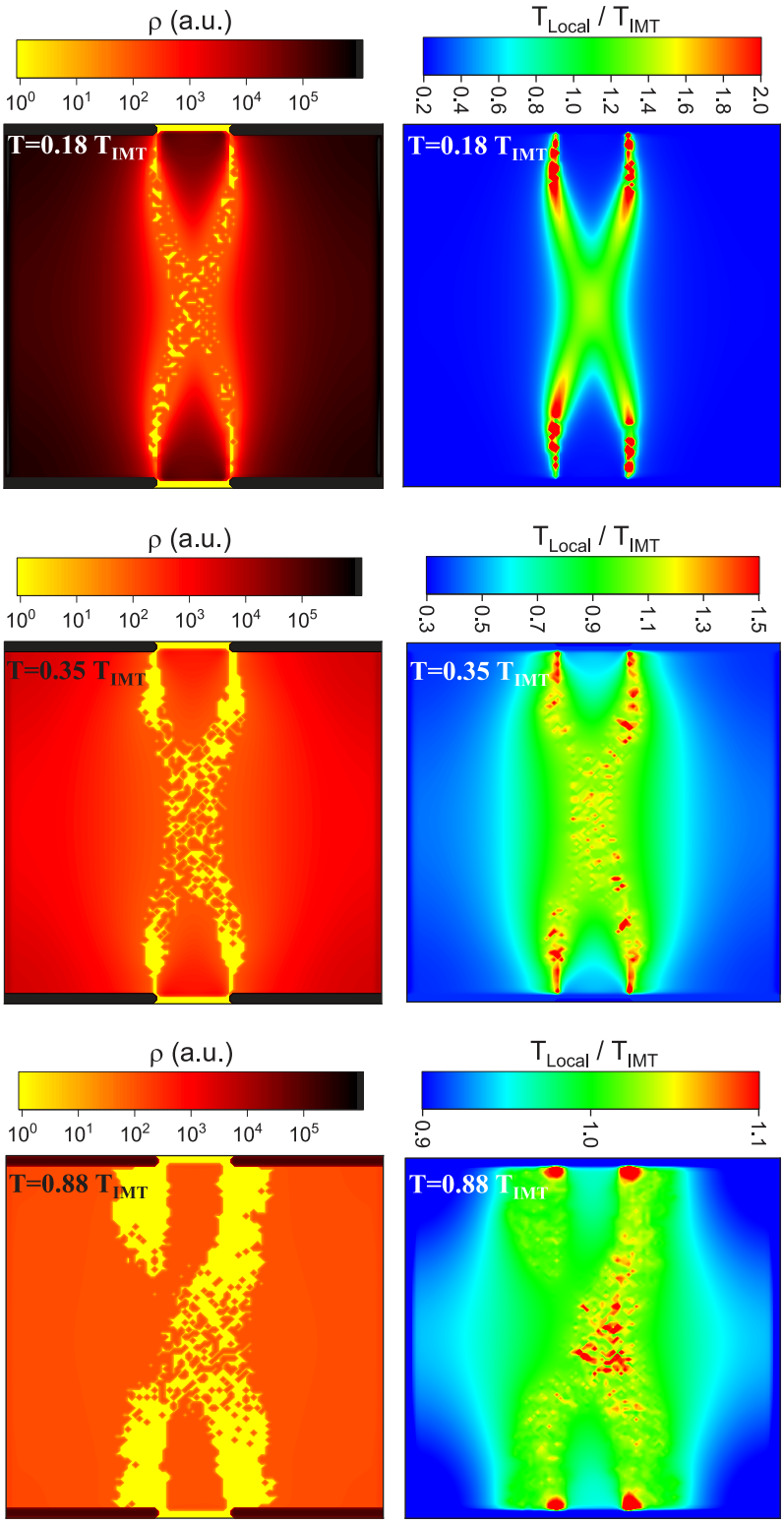

FIGURE 4.8 – Temperature and resistivity maps produced by the simulations for different values of the substrate temperature, keeping the base insulating resistivity fixed at $\rho_0 = 10^2$. Adapted from [Val+21].

for higher temperatures, the materials present a less abrupt switching behaviour as the applied voltage is increased, which is consistent with our prediction that at a higher temperatures the transition will be comparatively homogeneous, and the dependence of the incubation times on the applied voltage less steep.

It is also possible to compare the behaviour of the two materials for different applied voltages and different temperatures. This can be done by looking at the incubation times versus applied voltage curves of Figure 4.11. Different colors are used to represent different temperatures, and the time scale is logarithmic. Once again we see that the material which has the higher resistivity ratio, namely NdNiO3, present steeper incubation times curve, characterized by increasing error bars, as was the case for V2O3. On the other hand the incubation time curves of SmNiO3 look smoother, and are characterized by the absence of any variability whatsoever. This can be explained in light of the fact that SmNiO3, unlike NdNiO3, present a second order transition characterized by a lack of hysteretic behaviour (as evident from Figure 4.6) and thus metastability. The behaviour of materials presenting a second order transition will be investigated thoroughly in the next chapter.

4.4 Conclusion

In conclusion, we have used the MRN model to show that higher resistivity ratios lead to a comparatively inhomogenous resistive switching, characterized by stronger temperature gradients and the concentration of electric currents into thin metallic domains. The dependence of the incubation times on the applied voltage also becomes steeper, and the incubation times more difficult to predict as the applied voltage is lowered. These results are in analogy to those obtained in the previous chapter by using the thermal conductivity as the control parameter. We then show that our findings are consistent with VO2 and V2O3 experiments, in which it is found that V2O3, which presents a higher resistivity ratio, is characterized by a more abrupt switching behaviour and more variable incubation times as the applied voltage is lowered. We also study the growth of the metallic domain after the resistive collapse, finding that the increased power after the collapse of the resistance promotes an exponential growth. Our MRN simulations well capture this feature and are in qualitative agreement with the experimental results.

We then showed that it is possible to extend the MRN model to include a temperature dependent insulating resistivity. This feature is responsible for a more inhomogenous resistive transition at lower starting temperatures, since the starting resistivity is higher an so is the ratio between it and the metallic resistivity. This finding is consistent with the results obtained for the vanadium oxides, and in particular with the fact that V2O3 has more inhomogenous transition that VO2,

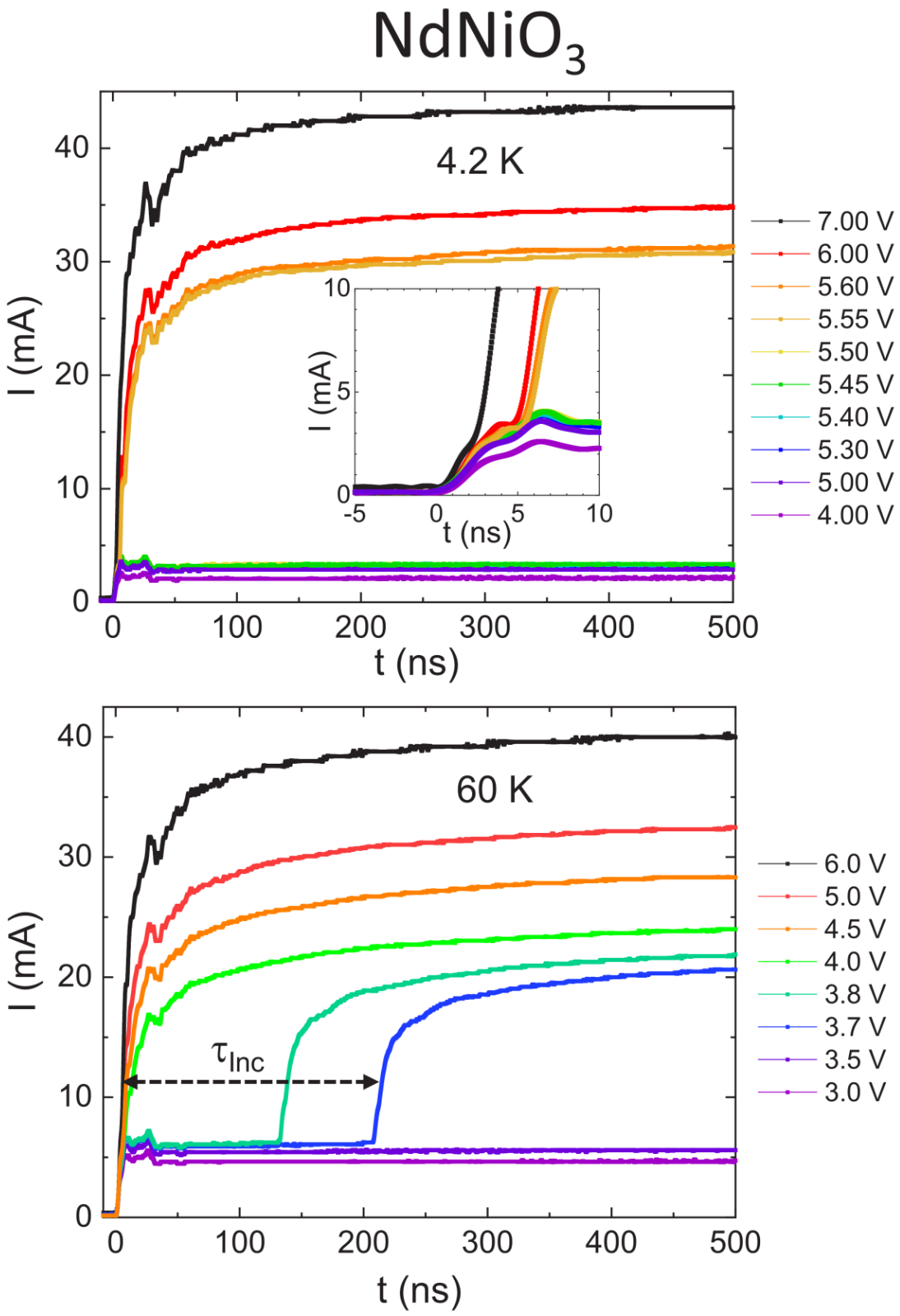

FIGURE 4.9 – Current flowing through a NdNiO3 sample versus time for different applied voltage. In the top panel initial temperature of the sample is at 4.2 K, in the bottom one it is a 60 K. The inset of the top panel shows a zoomed in view of the figure during the first 10 ns. Adapted from [Val+21].

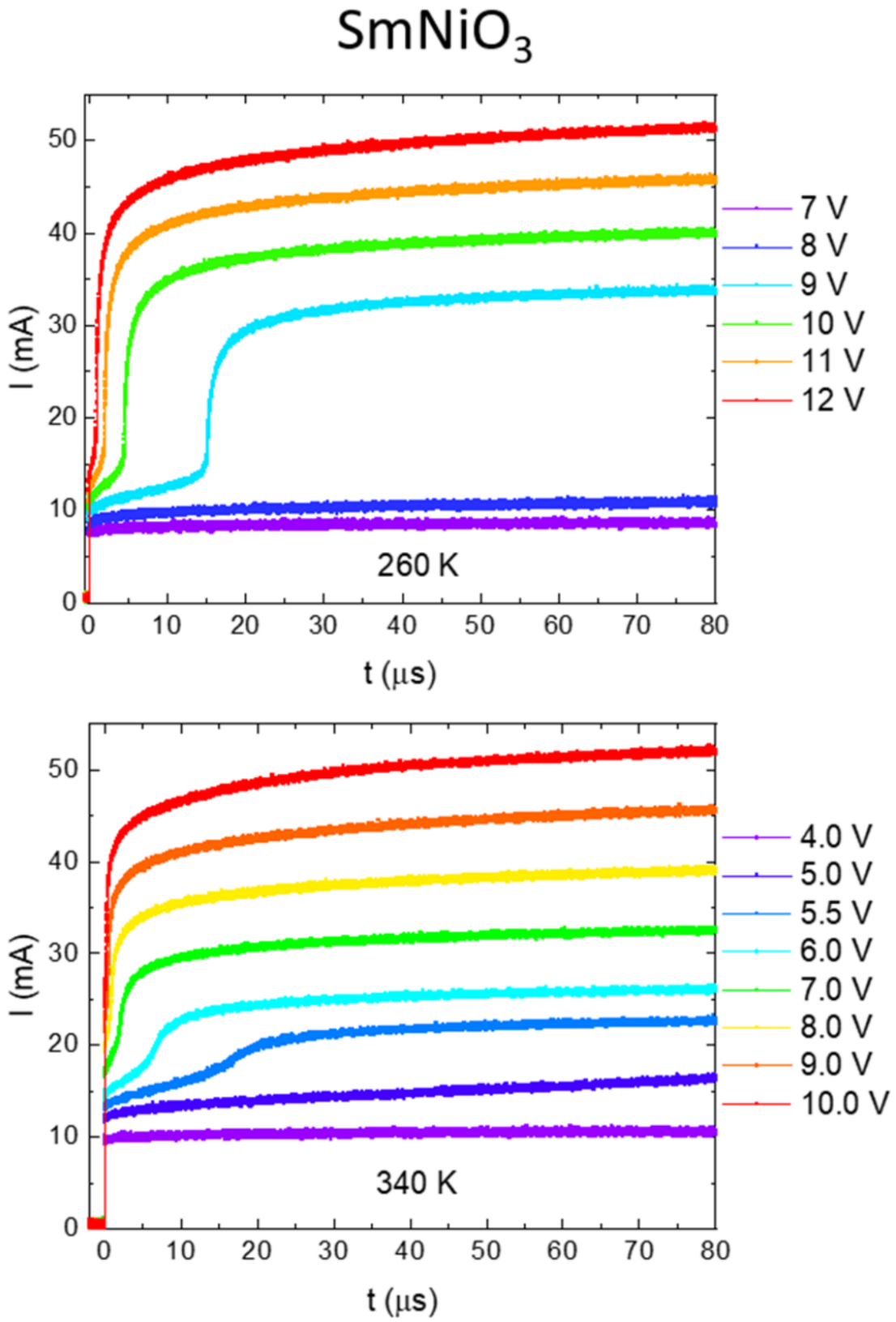

FIGURE 4.10 – Current flowing through a SmNiO3 sample versus time for different applied voltage. In the top panel initial temperature of the sample is at 260 K, in the bottom one it is a 340 K. Adapted from [Val+21].

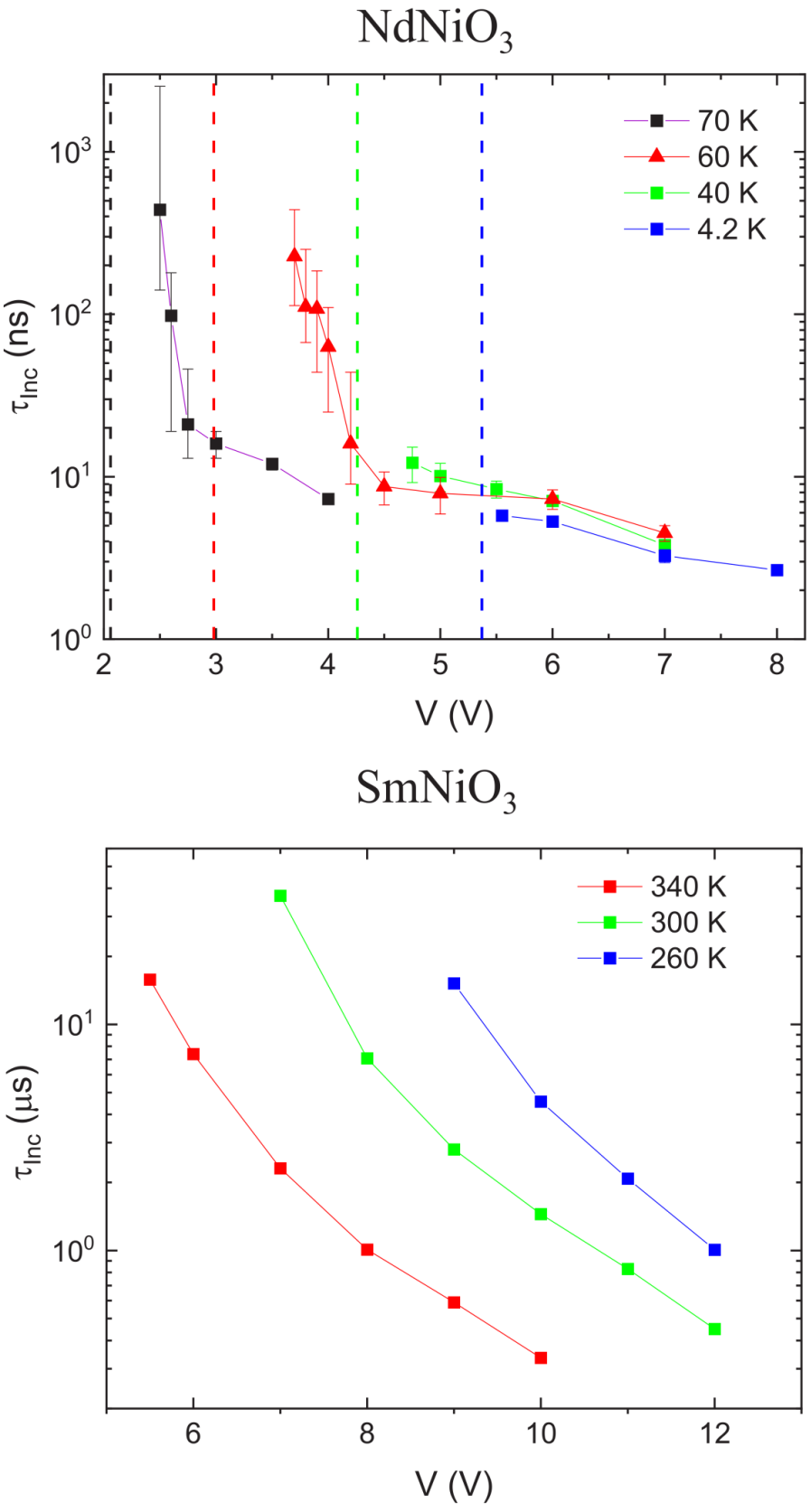

FIGURE 4.11 – Incubation times, in logarithmic scale, against voltage for a NdNiO3 sample in the top panel and a SmNiO3 sample in th bottom one ; each curve was obtained for a different initial temperature. Adapted from [Val+21].

having a higher resistivity ratio. We then showed that our simulations correctly predict the experimental behaviour : as the temperature of the substrate is lowered, the switching of the experimental sample to the metallic state becomes more abrupt. This is equally true for SmNiO3 and NdNiO3 samples. However, when the two materials are directly compared, it is found that the former generally has a more homogeneous behaviour, characterized by a less steep dependence of the incubation times on the applied voltage, and the absence of any variability in the incubation times. These features can be explained in light of the smaller resistivity ratio of SmNiO3, for any of the initial temperatures that have been chosen, and by the second order nature of its IMT, about which we will have more to say in the next chapter.

Chapitre 5

Oscillations in Mott neurons

Oscillatory patterns are typical of neurophysiology and are observed at different systems levels : single neuron, population dynamics and also Electro Enecephalo Graph (EEG) recordings (Figure 5.1) [Ger+14 ; Pey+12 ; War03 ; Don+98]. They can serve many different purposes, such as neuronal communication [Fri05] and motor coordination [SG05], just to give two examples. It is therefore of the utmost interest to study the possibility of inducing an oscillatory regime in a Mott neuron. Such regime may emerge in the presence of a capacitor that is put in parallel to the Mott sample, but might also arise spontaneously if the self capacitance of the material is high enough. Being able to induce an oscillatory regime in Mott materials, without the need for an external capacitor, would represent an advantage over traditional CMOS technology, since capacitors are particularly challenging to miniaturize [Hoe16 ; Par15 ; Mue+05].

In this section we extend the MRN model to describe the oscillatory regime which emerges in a V3O5 sample when a voltage ramp is applied. We do so by introducing a capacitor in parallel to the resistor network, which we use to model any capacitance the experimental system might have : self capacitance, external, parasitic or a combination thereof. We should stress that, experimentally, a capacitor might not be needed to observe an oscillatory regime, as it will be the case in the experiments presented in the next chapter. Since V3O5 presents a second order transition, characterized by a smooth resistance versus temperature curve and the lack of a hysteresis loop, we modify the MRN model to also account for these differences. Finally, we round off the edges of the simulated electrodes to induce the formation of the metallic filament in the middle of the sample, rather than at the edges, in analogy with the V3O5 optical imaging experiments presented in this chapter.

Using the MRN we find that, by applying a voltage ramp, it is possible to induce an oscillatory regime, which emerges after the collapse of the resistance, and eventually dies out as the voltage is increased. We produce resistivity maps,

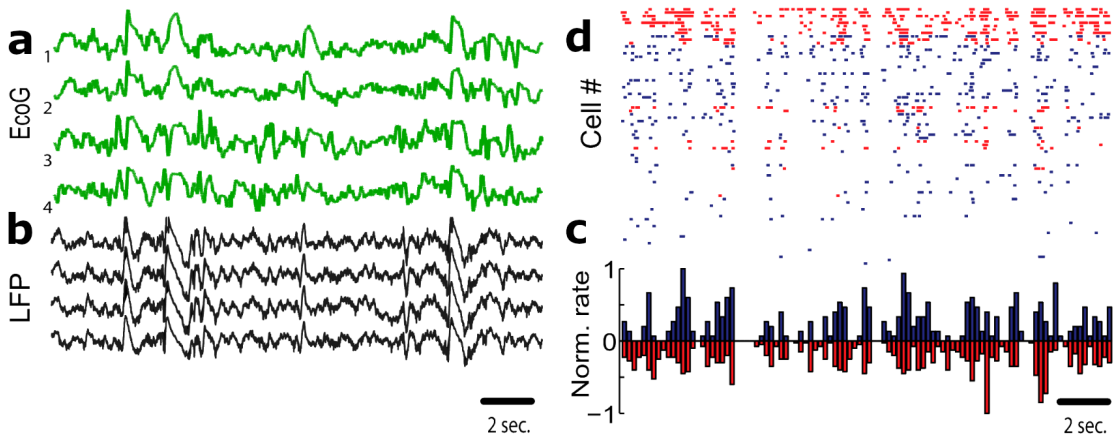

FIGURE 5.1 – Neural oscillations in the brain from the macroscopic to the single cell levle. a) EEG traces b) Local field potential recordings c) Raster graph : the dots represent spiking events (each vertical coordinate corresponds to a different neuron), red dots are spikes from inhibitory connections and blue ones from excitation connections. Oscillatory patterns may be identified in the succession of periods of activity, when multiple neurons fire at the same time, and of silence. d) Firing rate histograms normalized by the number of neurons. Adapted from [Pey+12].

from which we are able to understand the oscillatory regime as an effect of the coupling of the Mott sample with the capacitor. In particular, we see that the resistive collapse provokes a discharge of the capacitor. The Mott material then cools down and relaxes back to the insulating state, while the capacitor gradually charges back. When the capacitor is charged, the Mott sample will heat up and metallize once again. This cycle continues until the applied bias is so high that the capacitor charges too fast for the sample to cool down, and the metallic filament stabilizes, thus interrupting the oscillatory regime. We also study the effect of different capacitance values on the amplitude and frequency of the oscillations, finding that a bigger capacitance results in a higher amplitude and a lower frequency, as expected.

We finally turn our attention to the results of the V3O5 experiments. We find that the predictions of our simulations are validated by the experiments and allow to better understand the growth and subsequent shrinking of the metallic filament which is observed in the oscillatory regime.

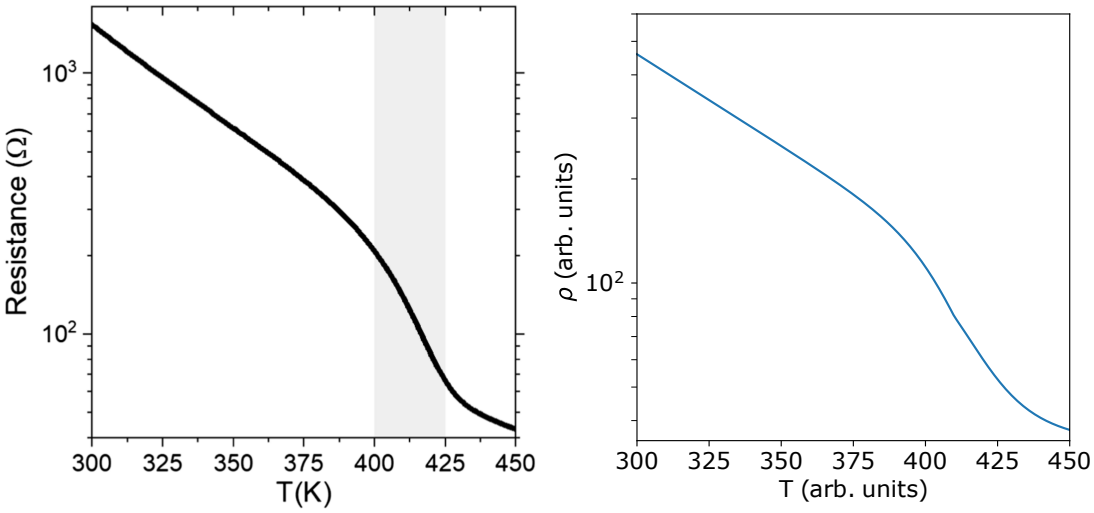

FIGURE 5.2 – Left panel : experimental resistance versus temperature curve of a V3O5 sample. Gray color indicates the crossover region around the transition temperature. Right panel : resistivity versus temperature curve adopted in the simulations presented in this chapter. Adapted from [Add+22]

5.1 Expanding the MRN

In this section we extend the MRN model in order to describe materials, such as V3O5, which present a second order IMT, characterized by a resistance versus temperature curve which lacks the abrupt resistive collapse and hysteresis loop that could be found in materials with a first order transition like VO2. We also round the edges of the electrodes in order to reduce the point effect, decrease the temperature near the edges and induce the formation of the metallic filament in the middle of the sample. Finally, we introduce a capacitor in parallel to the sample, in order to model the capacitance of the experimental setup which gives rise to the oscillatory behaviour which is studied in depth in the next section.

We begin by looking at the left panel of Figure 5.2, in which the resistance of an experimental V3O5 sample is plotted against the temperature. We see that, as the temperature is increased, the resistance decreases exponentially. Unlike VO2 and V2O3, V3O5 does not present a sudden jump of the resistance when the transition temperature $T_{IMT} = 415$ K is reached, but rather a smooth crossover region (colored in gray in the figure) in which the resistance decreases at a faster rate than before. We also notice that the curve lacks an hysteresis loop, meaning that the resistance of the material, and therefore of the cells of the MRN, is univocally determined by the temperature. All of these considerations lead us to implement the following changes to the MRN. The cells of the MRN do not undergo anymore

Parameter	Value
ρ_0	400
a	0.1
b	0.2
c	5
T_{IMT}	410

TABLE 5.1 – Constants used in the phenomenological expression of the temperature dependent resistivity (Equation 5.1)

a transition from an insulating to a metallic state according to an Arrhenius like probability law. Instead, the resistivity of a cell is determined by its temperature according to the following phenomenological equations, which are written as to reproduce the experimental resistance versus temperature curve (see right panel of Figure 5.2)

$$\rho(T) = \rho_0 \ \alpha(T) \ \ (a + b \ \sigma(T)) \tag{5.1}$$

$$\alpha(T) = \exp\left[c\left(\frac{T_{IMT} - T}{T_{IMT}}\right)\right] \tag{5.2}$$

$$\sigma(T) = \left(1 + \exp\left[\Delta(T)(T - T_{IMT})\right]\right)^{-1} \tag{5.3}$$

$$\Delta(T) = d \ \theta(T_{IMT} - T) + \frac{d}{5} \ \theta(T - T_{IMT}) \tag{5.4}$$

where ρ_0, a, b and c are constants that are chosen in order to approximate as much as possible the $R(T)$ experimental curve (the values used in the simulations of this chapter are presented in Table 5.1 ; the other simulation parameters are listed in Table 5.2). This set of equations can be understood as follows : $\rho(T)$, which is the temperature dependent resistivity of a given cell of the MRN, has a crossover region around the transition temperature T_{IMT} which, in logarithmic scale, approximately looks like a sigmoid. Therefore, we use Equation 5.3 to describe this contribution, which we call $\sigma(T)$. However, since the shape is approximately sigmoidal only in logarithmic scale, $\sigma(T)$ needs to be multiplied by an exponential, $\alpha(T)$ (Equation 5.2), similarly to how we multiply the constant a by the same exponential to reproduce the linear decrease that occurs before the crossover region. Different exponents $\Delta(T)$ are used for the exponential contribution, depending on whether the temperature is lower or higher than the transition temperature (here we note that the $\theta(T)$ of Equation 5.4 are Heaviside functions).

We now move on to the issue of inducing the filament formation in the middle of the sample. Up until now all the simulations that we have presented have featured electrodes with sharp 90 degrees angles. This has resulted in a strong point effect

and, as a consequence, strong electric fields and temperature gradients around the edges ; this is the reason why filaments always protrude from the edges of the electrodes in our simulations. To remedy this, in order to bring the simulations closer to the optical imaging experiments presented in this chapter, we make the edges of the electrodes rounded. In this way the point effect is not as strong as before, and the filament will form in the middle of the sample, which is now the region of the materials that warms up the fastest.

In order to better appreciate the effects of these changes on the simulations, we present an IV curve obtained using a current ramp, as well as temperature maps that show the growth of the metallic filament (Figure 5.3). We would like to stress that, in these simulations, we haven't introduced the capacitor yet. These results are to be compared with the experimental V3O5 IV curve and optical reflectivity maps that are shown in Figure 5.4. The optical reflectivity measurements were done using the setup that is schematically shown in the left panel of Figure 5.5. A white LED illuminates the sample through a 100x objective and a Charged-Coupled Device (CCD) camera images the device as shown in the right panel of Figure 5.5. The exposure time is 55ms, so every image is effectively a time-average of the state of the sample within the exposure window. The optical reflectivity images of Figure 5.4 are produced by subtracting the image taken at the corresponding point of the IV curve to an image taken before the current was turned on.

From the comparison we can appreciate how the IV curve produced by the simulations is qualitatively comparable to that of the experiments. We also notice that the simulations predict the formation of the metallic filament in the middle of the sample and its subsequent growth that is observed in the optical reflectivity maps.

We now turn to the problem of modelling the capacitance of the circuit. The source of this capacitance might be a physical capacitor that is put in parallel to the sample, as it will be the case in the next section, or the sample itself, which could potentially have a self capacitance. Finally, a parasitic capacitance, due to the cables and the instrumentation used, might also be present. Regardless, our solution is to put a capacitor in parallel to the MRN, as shown in the right panel Figure 5.6. Then, using Ohm's and Kirchhoff's laws, we compute its current and voltage, $I_C(t)$ and $V_C(t)$. Since the capacitor and the sample are in parallel, we can easily compute the sample voltage as $V_S(t) = V_C(t) + I_C(t)R_C$, where R_C is a resistor that could potentially be put in series to the capacitor, to faithfully reproduce the experimental setup ; the voltage just computed is then applied to the MRN and the simulation proceeds as usual, following the steps described in Chapter 2.

Here we illustrate in detail the mathematical derivation that allows us to write the equation for the sample voltage, $V_S(t)$, exclusively in terms of known quantities.

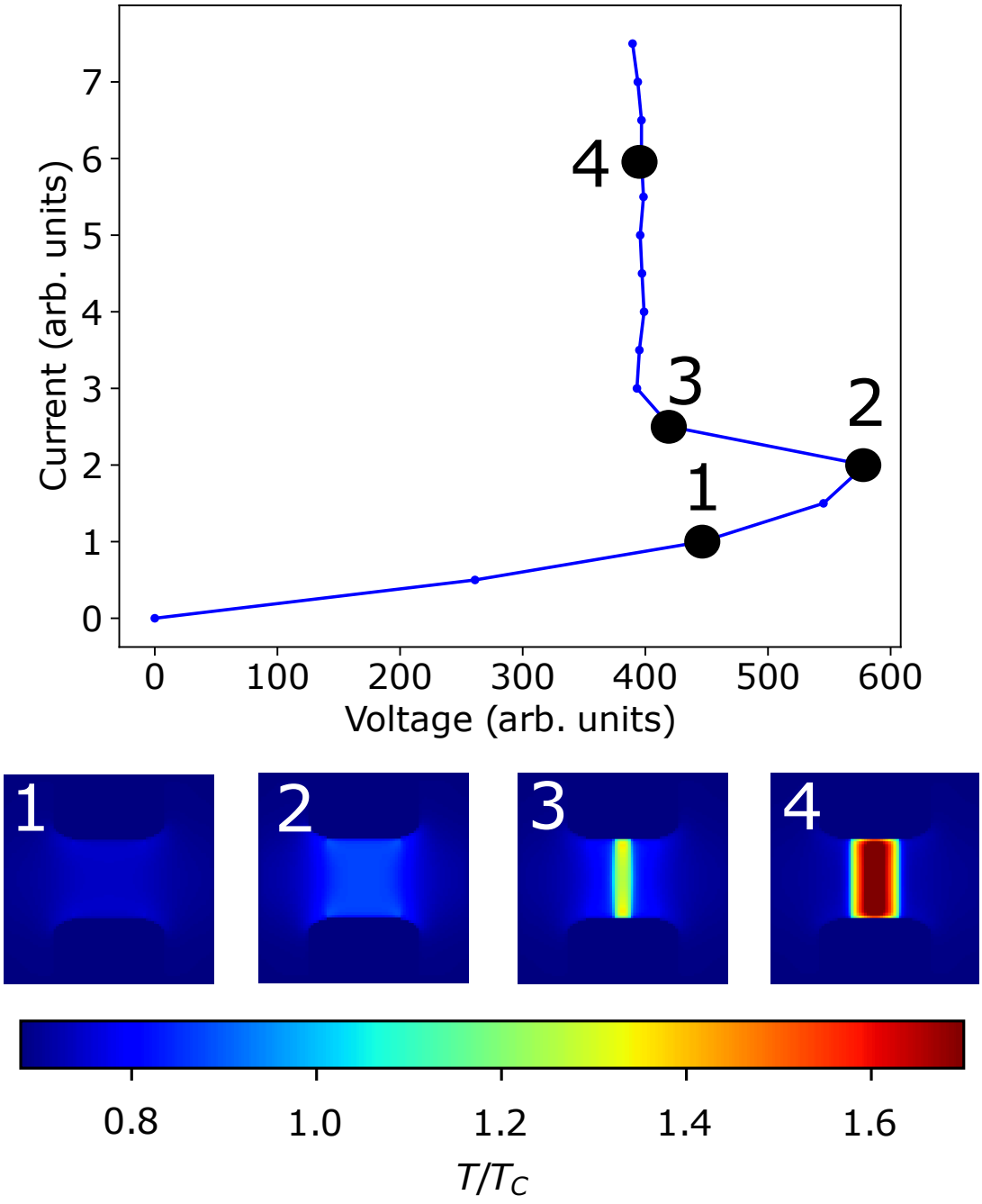

FIGURE 5.3 – IV curve of a MRN simulation, implementing the temperature dependent resistivity described by Equation 5.1. A current ramp was applied to produce the curve. In the simulations, the current control regime is actually achieved by controlling the applied voltage and choosing a load resistance which is high (i.e. comparable to the insulating value of the resistivity). In this way the current through the sample will remain approximately equal to V_{app}/R_{load}. The bottom panels show temperature maps produced at 4 different times during the application of the current ramp.

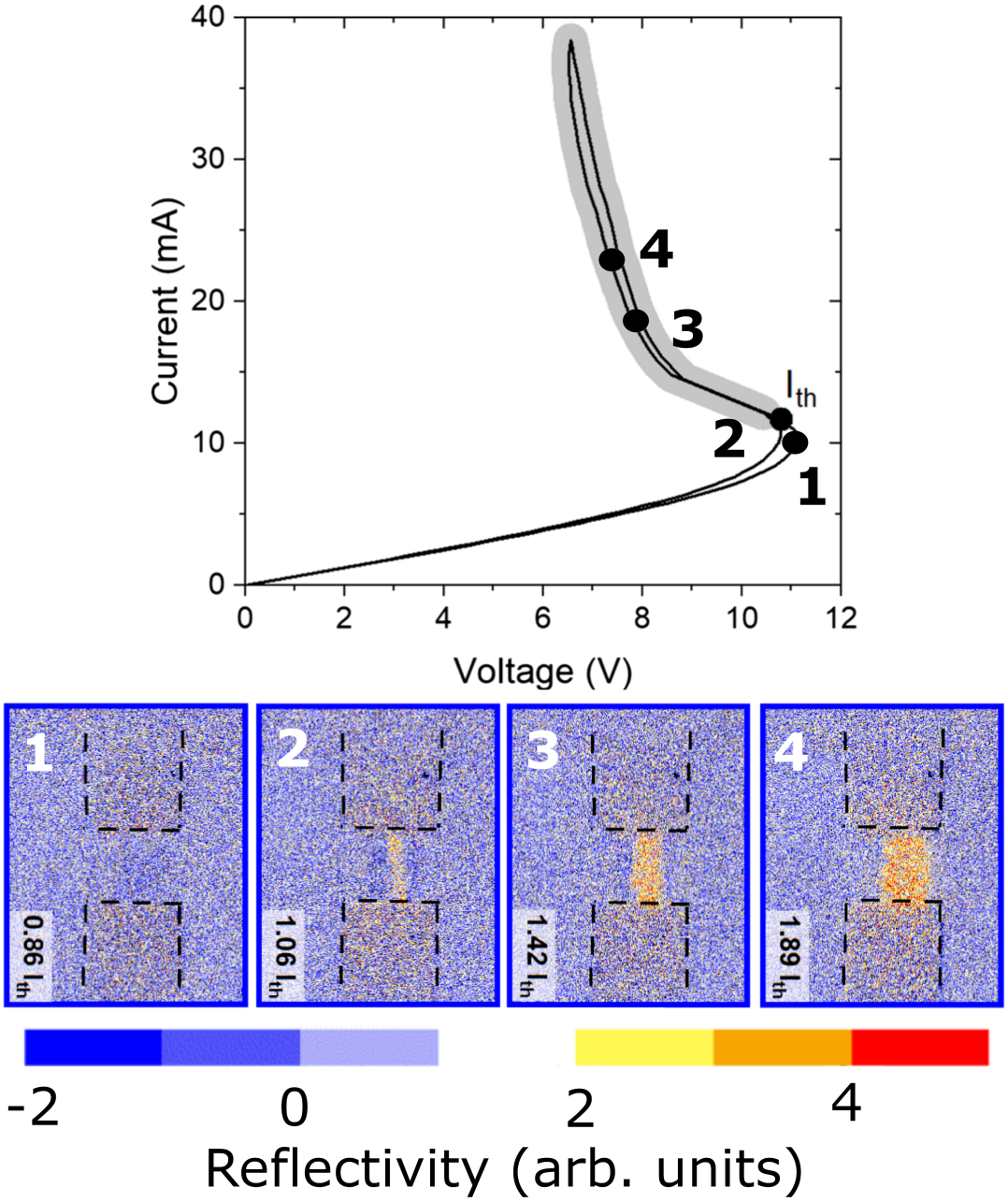

FIGURE 5.4 – Top panel : IV curve of the V3O5 sample used in the experiments mentioned in this chapter. A current sweep was applied to produce the curve. Bottom panels : differential reflectivity maps, obtained by shining a light on the sample using a white led and capturing the reflected beam using a CCD camera (see Figure 5.5). Each map has been subtracted from an image capture before the current was turned on in order to enhance its features. Adapted from [Add+22]

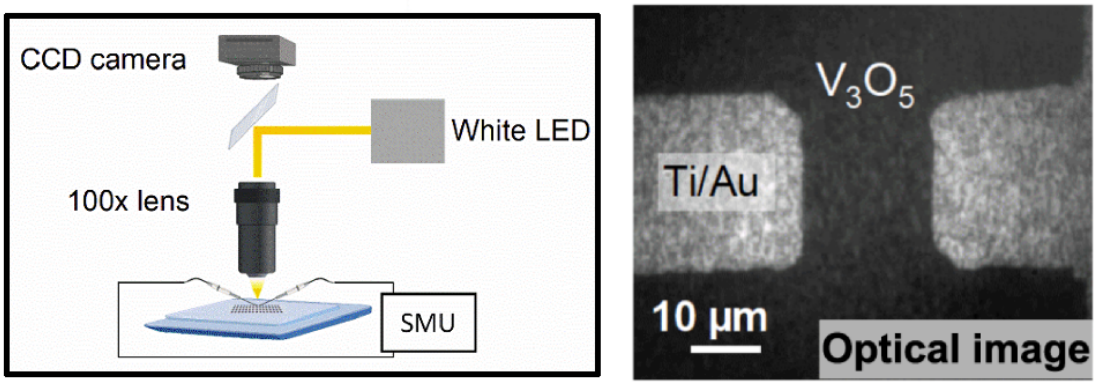

FIGURE 5.5 – Left panel : experimental setup used to capture the optical reflectivity images shown in this chapter. Right panel : example of an optical reflectivity image captured before the current was turned on. Adapted from [Add+22]

Firstly, we must must compute I_C (t is omitted for the sake simplicity). We begin by writing the voltage of the sample by considering the closed loop made of the voltage generator and the sample itself and applying Kirchhoff Voltage Law (KVL) :

$$V_S = I_S R_S = V_{app} - I R_L \tag{5.5}$$

Where I_S is the current that flows through the sample and $I = I_C + I_S$ the total current. The current of the sample can then be written as :

$$I_S = \frac{V_{app} - I R_L}{R_S} \tag{5.6}$$

If we are in the voltage controlled regime, as will be the case in the following, I is the only unknown among the quantities that appear in the equation. V_{app} and R_L are parameters that can be chosen at will ; the initial value of the sample resistance R_S depends on the chosen resistivity and the geometry of the sample, and can be measured by probing the MRN with a small voltage after having momentarily disconnected the capacitor. Kirchhoff Current Law (KCL) gives us :

$$I = I_S + I_C \tag{5.7}$$

Therefore we can rewrite Equation 5.6 as :

$$I_S = \frac{V_{app} - (I_S + I_C) R_L}{R_S} \tag{5.8}$$

Solving for I_S we obtain :

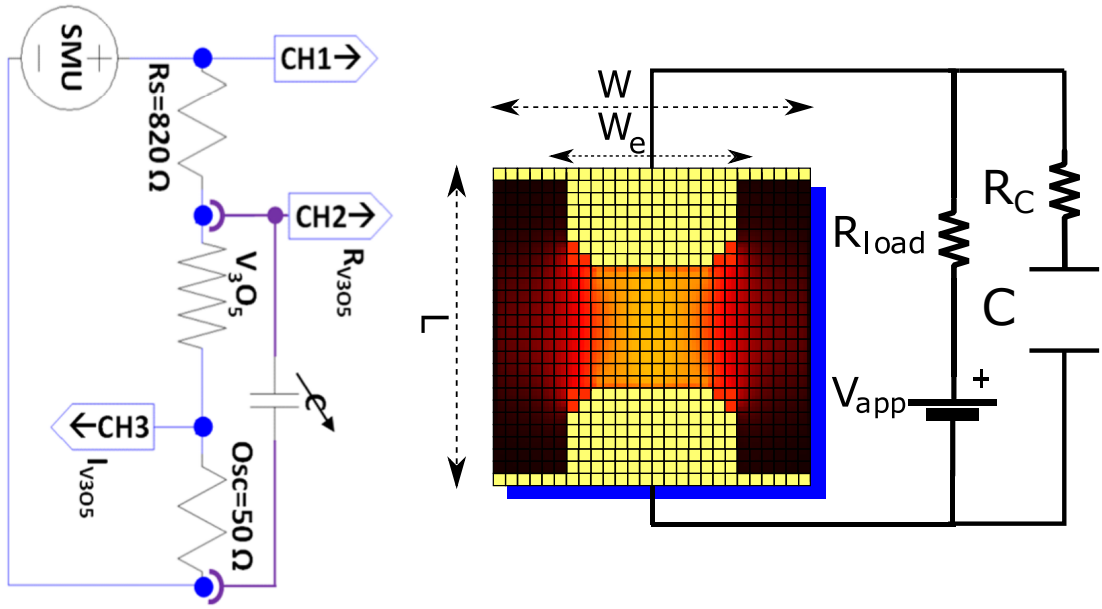

FIGURE 5.6 – Left : Experimental circuit. SMU is the source meter unit. CH1 allows a measurement of the current through the series resistor, R_S, which gives an oscillatory behavior for a certain voltage range, used to measure the frequency of oscillations (see [Add+22]). CH2 provides the voltage across the capacitor, which allows for the determination of the resistance of the device. CH3 gives a measurement of the current going through the V_3O_5 device, which gives the spiking behavior. Right : Circuit that is adopted in our simulations. The MRN is now in parallel with a capacitor which is itself in series with resistor R_C. This resistance is included in our calculation for the sake of generality, however it was put to 0 in our simulations. We also notice that the resistivity of the cells depends smoothly on the temperature.

$$I_S = \frac{V_{app} - I_C R_L}{R_S + R_L} \tag{5.9}$$

We still don't know I_C, so the above equation can not be solved yet. Therefore we move on on to the capacitor branch, and once again we apply KVL, this time to the closed loop made of the sample, the capacitor and the resistor R_C, to obtain :

$$\begin{aligned} I_C R_C &= -V_C + I_S R_S \\ I_C &= \frac{-V_C + I_S R_S}{R_C} \end{aligned} \tag{5.10}$$

Plugging in Equation 5.9 we get :

$$I_C = \frac{1}{R_C}\left(-V_C + R_S \frac{V_{app} - I_C R_L}{R_S + R_L}\right) \tag{5.11}$$

Finally we solve for I_C :

$$I_C = \frac{R_S V_{app} - V_C(R_S + R_L)}{R_C(R_S + R_L) + R_S R_L} \tag{5.12}$$

In the above equation the only unknown quantity is V_C. However, starting from the definition of the capacitance $C = dQ/dV$ we have :

$$C = \frac{dQ}{dV} = \frac{dQ}{dt}\frac{dt}{dV} = I_C \frac{dt}{dV} \tag{5.13}$$

Since we are considering simulations with a finite time-step, the increments are also finite, and the above equation can be written as :

$$\begin{aligned} C &= I_C \frac{\Delta t}{\Delta V} \\ V_C(t) &= V_C(t-1) + \frac{I_C(t)\Delta t}{C} \end{aligned} \tag{5.14}$$

We have re-introduced the variable t, which is discrete in our simulations ; additionally, we decide to keep the time-step Δt even if in our simulations $\Delta t = 1$, as a reminder of the physical dimensions of the equations. At any point in time t the quantities computed at time $t-1$, i.e. the previous iteration of the simulation, are known. Therefore, we can take Equation 5.14 and put it in 5.12, and after solving for I_C we obtain :

$$I_C(t) = C \frac{R_S(t) V_{app}(t) - V_C(t-1)(R_S(t) + R_L)}{C[R_C(R_S(t) + R_L) + R_S(t) R_L] + \Delta t(R_S(t) + R_L)} \tag{5.15}$$

Parameter	Value	Meaning
T_{IMT}	410.0	Insulator to metal transition temperature
T_0	280	Substrate temperature
R_L	5 10^2	Load resistance
R_C	0	Resistance in series with capacitor
C	1	Capacitance
W	80	Network width
W_e	42	Electrode width
L	80	Network length
K	0.01	Thermal conductivity
ρ_0	400	Resistivity at T_{IMT}
a	0.1	Resistivity curve constant
b	0.2	Resistivity curve constant
c	5	Resistivity curve constant

TABLE 5.2 – Parameters used in the simulations of this chapter. Since we model a second order transition, some of the parameters of the previous simulations are not applicable. The constants that concern the phenomenological resistivity curve are reported here for convenience's sake and can also be found in Table 5.1

Now that the current of the capacitor has been computed, we ca use Equation 5.14 to derive the voltage of the capacitor and from it that of the sample. We then apply this voltage to solve the MRN model, which yields the new values of the sample resistance R_S and current I_S, which will be used at the next step to solve equation 5.15. Thus the loop is closed and the simulation can continue.

5.2 The oscillatory regime

We now study the oscillatory regime that is observed in MRN simulations when a voltage ramp is applied to a sample and a capacitor in parallel (a current ramp may also be applied to achieve similar results). More specifically, the voltage protocol is defined as follows : starting from zero applied voltage, the voltage is increased up to a value of $V_{app} = 6000$ (arb. units) in steps of 10 (arb. units) for a total of 600 steps. Each step has a length of 100 simulation loops, during which a fixed voltage is applied to the circuit, before it is increased by 10 (arb. units) at the 101-th loop, when the next voltage step begins. A visualization of a subset of the voltage protocol (up until $V_{app} = 200$ (arb. units)) is provided in the inset of Figure 5.7.

We begin by taking a look at the IV curve and the resistivity maps of the simulated sample that are shown in Figure 5.7. While the ramp voltage applied

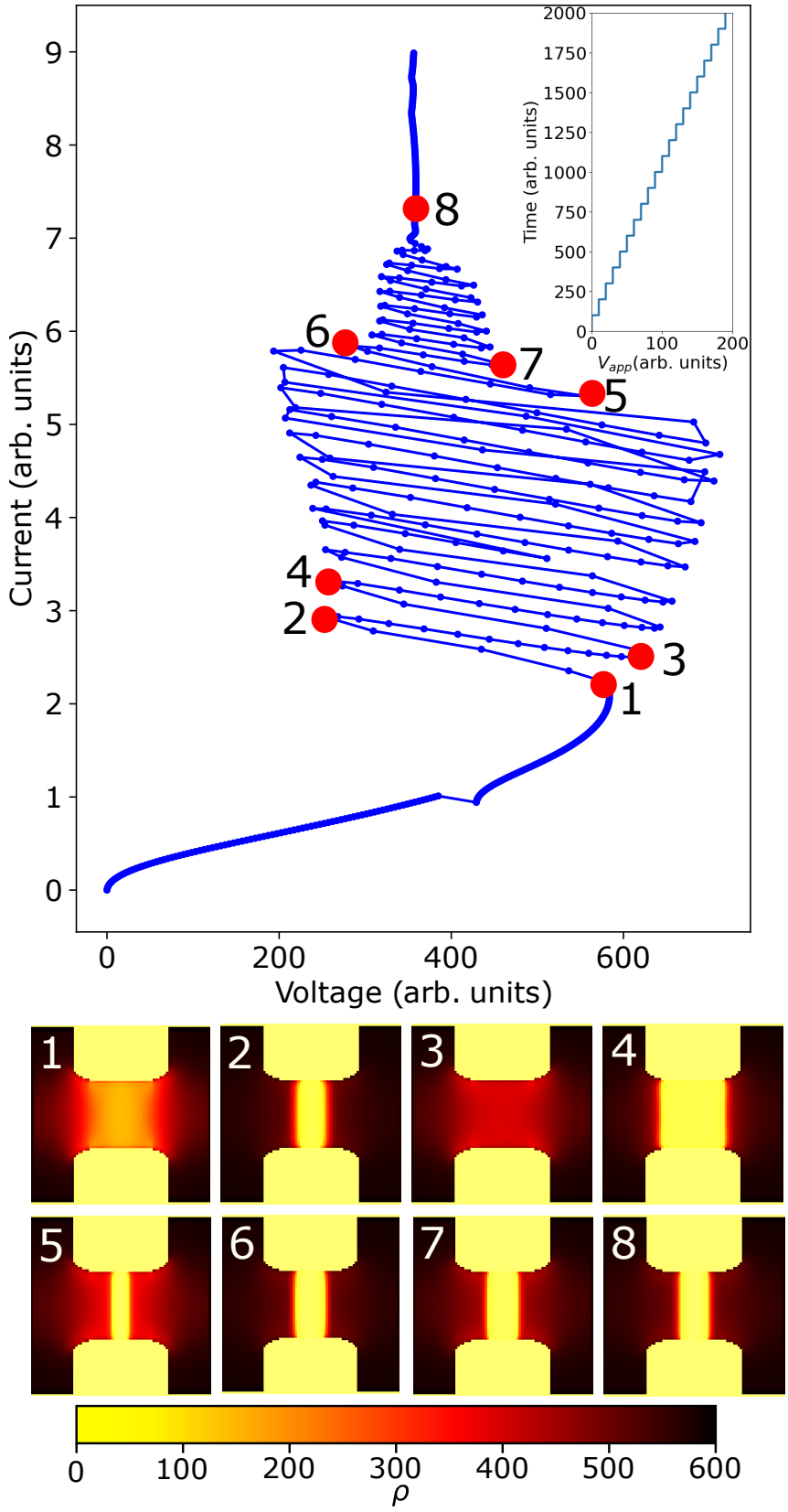

FIGURE 5.7 – Top panel : IV curve obtained by applying a voltage ramp to the simulated MRN and measuring the voltage across the sample and the total current. Inset : visualization of a subset of the voltage ramp that goes up until $V_{app} = 200$ (arb. units). For each voltage step the values of the current and voltage were captured only once at the end of the step. Bottom panels : resistivity maps captured at eight different point in times during the application of the voltage ramp.

to the circuit goes up to a value of $V_{app} = 6000$, the IV curve is cut short at around $V_{app} = 4870$ (arb. units) (when the total current reaches a value of $I = 9$ (arb. units)), since by then the oscillatory regime has clearly ended. Moreover, the resistance in series with the capacitor R_C (see Figure 5.6) has been taken out for simplicity, so now the capacitor and the sample share the same voltage, which is plotted on the x-axis of the main panel, while on the y-axis we plot the total current, i.e. the sum of the current that flows through the sample and the current of the capacitor $I = I_S + I_C$. Also, we would like to notice that each point of the IV curve was taken at the end of the corresponding step of the voltage protocol, so there are as many data points in the IV curve as steps in the voltage ramp.

Initially the capacitor is empty and the voltage starts at 0. As the applied voltage is increased, the capacitor charges and the voltage goes up. The increasing voltage makes the sample heat up and eventually the resistive collapse occurs. The sudden drop of the sample resistance makes the capacitor discharge (i.e. charge flows from the plate of the capacitor into the sample), resulting in the downward swing of the voltage. Resistivity map 1 was taken right before the resistive collapse and the discharge of the capacitor, while map 2 was taken when the filament is formed and the discharge has ended, and they are both qualitatively comparable to temperature maps 2 and 3 of Figure 5.3, where no capacitor was present. However, we notice that the voltage drop is bigger than in the IV without the capacitance (despite using the same parameters for the circuit) because the discharge of the capacitor produces an influx of extra current into the sample, which thickens the metallic filament, further lowering the resistance.

The discharge of the capacitor can't go on indefinitely, since the charge accumulated on the plate is limited, and eventually it stops, and so does the downward trend of the voltage. As the current flowing from the capacitor into the sample first decreases and then disappears, the hot metallic filament cannot be sustained and cools down, gradually relaxing to the insulating state. At the same time, the depleted capacitor begins to accumulate charge once again, raising the voltage and heating up the sample, now fully in the insulating state (resitivity map 3). Thus a new resistve collapse is triggered, which is followed by another discharge of the capacitor.

We notice that, as the applied voltage is increased, the amplitude of the oscillations also increases, due to the fact that the capacitor accumulates more charge (higher peaks) which then flows into the sample during the discharge, resulting in a thicker filament and a smaller resistance (lower peaks - see for instance resistivity map 4). However, past a certain applied voltage the amplitude starts decreasing until the oscillations disappear altogether. Since the charging time of the capacitor lowers with the increasing applied voltage, eventually the filament does not have enough time to fully relax to the insulating state (resistivity map 5) before the

capacitor charges to a high enough voltage to heat it up and expand it (resistivity map 6). If the amplitude of the oscillations decreases, so does the charge accumulated by the capacitor and the ensuing discharge current, leading to thinner filaments than before (compare maps 6 and 4). A smaller metallic domain needs less power to be sustained, while the applied voltage is actually increasing, and so the capacitor charges to the required, lower voltage faster than ever (resistivity map 7) : thus a positive feedback loop is established which ultimately leads to the stabilization of the metallic state (resistivity map 8).

5.2.1 Oscillations at fixed applied voltage

To further investigate the oscillatory regime we study the system when a constant voltage, equal to $V_{app} = 2300$ arb.units, is applied. The stimulus protocol is defined as follows : firstly a voltage ramp is applied, like before, to heat up the sample and induce the resistive collapse. Once the sample has entered the oscillatory regime and has reached the target voltage $V_{app} = 2300$ arb.units, the applied voltage is fixecd. In Figure 5.8 we plot the data produced by the simulations for two values of the capacitance, $C = 5$ and $C = 10$ arb. units. From top to bottom we plot the sample resistance, the voltage across the sample and the capacitor, the sample current and the capacitor current, all against time. The dashed lines are guidelines that indicate the moment when the metallic filament is formed and the resistance is the lowest.

Following the numbered dots of Figure 5.8 we may elucidate the relation between the resistance, the voltage and the current during the oscillations. Starting at number 1, when the resistance is the highest, we notice that, immediately after, the sample current begins to increase (blue curve) and the capacitor current to decrease (red curve). That is to say, as the filament forms and the resistance goes down, more current flows in the sample and less in the capacitor. However, since the capacitor current is still positive, the capacitor continues to charge, albeit slower than before, and the voltage to rise. Eventually though the capacitor current goes below zero (dot number 2), and the discharge begins : current flows from the capacitor into the sample, drastically lowering its resistance, while the voltage goes down. The discharge cannot continue indefinitely, and so a minimum of the resistance is reached (dot number 3), after which the discharge still continues, but at a slower pace, as less and less current flows from the capacitor into the sample. If the discharge current decreases the metallic filament cannot be sustained and so it begins to cool down, and the resistance goes up ; the discharge current ends and the capacitor begins to charge again (dot number 4), raising the voltage until it is enough to heat up the sample and induce a new resistive collapse.

Finally, we notice that, when the capacitance is smaller both the period of the oscillations and the amplitude of the current are smaller, since less time is

required to charge the capacitor, and less charge is accumulated and subsequently discharged.

5.2.2 Experimental results

We now turn to the experiments to check if the results of the simulations find confirmation. We start with optical imaging experiments conducted on a V3O5 sample in parallel to a capacitor, as shown the left panel of Figure 5.6, to which a ramp current was applied. In particular, we are interested in imaging the growth and subsequent relaxation of the metallic domain in the oscillatory regime. In Figure 5.9 we show four differential contrast reflectivity images. The first one from the left was acquired before the oscillatory regime, the second and the third during the oscillatory regime, and the last one after. Surprisingly, the two pictures taken during the oscillatory regime do not clearly show the presence of a metallic domain ; however, at the same time, the gap does not appear to be completely insulating since a light trace of the metallic phase, indicated by the color orange, is appreciable. The simulations allow us to understand this puzzling result : from the resistivity maps presented in Figure 5.7, we know that during the oscillatory regime the metallic filament shrinks and then grows, concurrently with the rise and fall of the voltage. Since the time resolution of the instrumentation used in the experiments is limited, due to an exposure time of 55 ms, we are not capable of imaging this behaviour. Instead, the differential contrast images provide a time-average of the state of the system (each image is an average of 38 to 55 oscillations, depending on the bias), therefore the light orange trace that is observed can be explained as the superimposition of two snapshots of the system, when it is fully insulating and no filament is present (like, for instance, in map 3 of Figure 5.7), and when the gap has become fully metallic (map 4).

Figure 5.10 shows the current that flows through the experimental sample when a constant bias, high enough to induce the resistive collapse, is applied. These measurements, which clearly indicate the presence of an oscillatory regime in the experimental sample, are to be compared with the simulation results of Figure 5.8. We notice that the experimental results are qualitatively comparable to those of the simulations, and that when the capacitance is increased, the amplitude and the period of the oscillations increase as predicted.

5.3 Conclusion

In this chapter we have extended the MRN model to describe the behaviour of materials presenting a second order IMT under a bias. We did so by replacing the thermally activated switching mechanism used in the previous chapter with

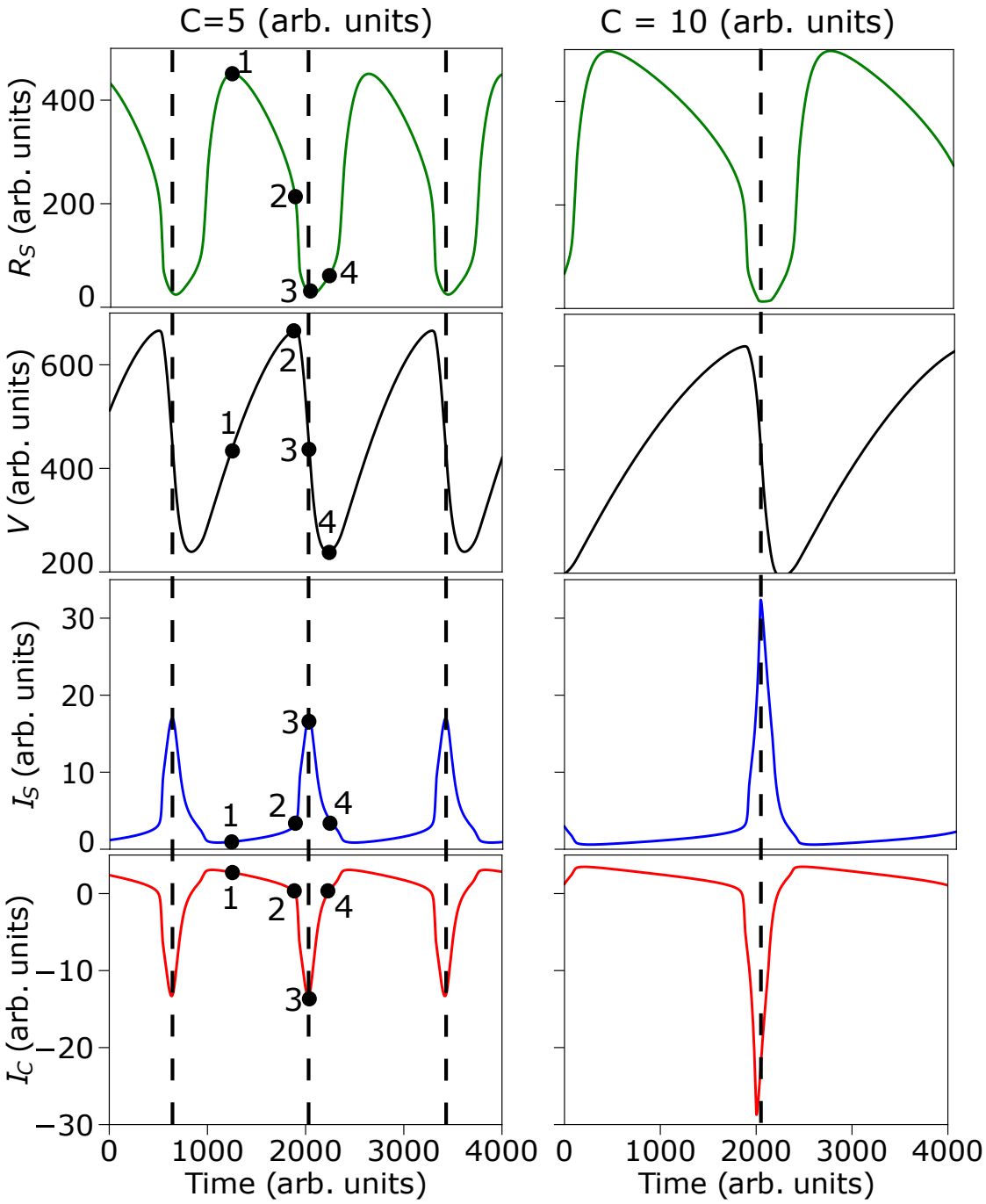

FIGURE 5.8 – From top to bottom : sample resistance, voltage of the sample and of the capacitor, current of the sample and current of the capacitor against time. Data from the simulations obtained for a fixed applied voltage of $V_{app} = 2300$ arb.units. Left column figures were obtained for a capacitance value of $C = 5$ arb. units, those on the right for $C = 10$ arb. units.

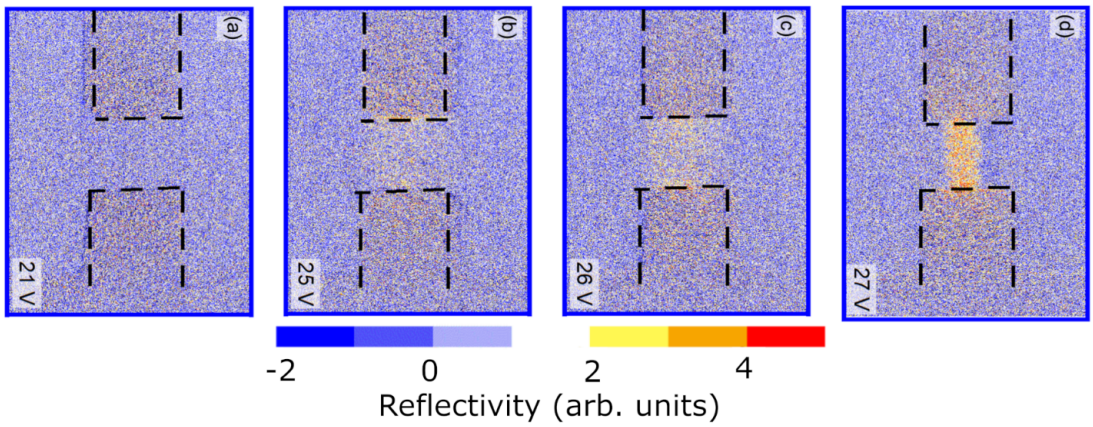

FIGURE 5.9 – Contrast differential optical reflectivity images of a V3O5 sample under a current ramp and in parallel to a capacitor. The first picture from the left was taken before the oscillatory regime, the second and third during, and the last one after. Adapted from [Add+22]

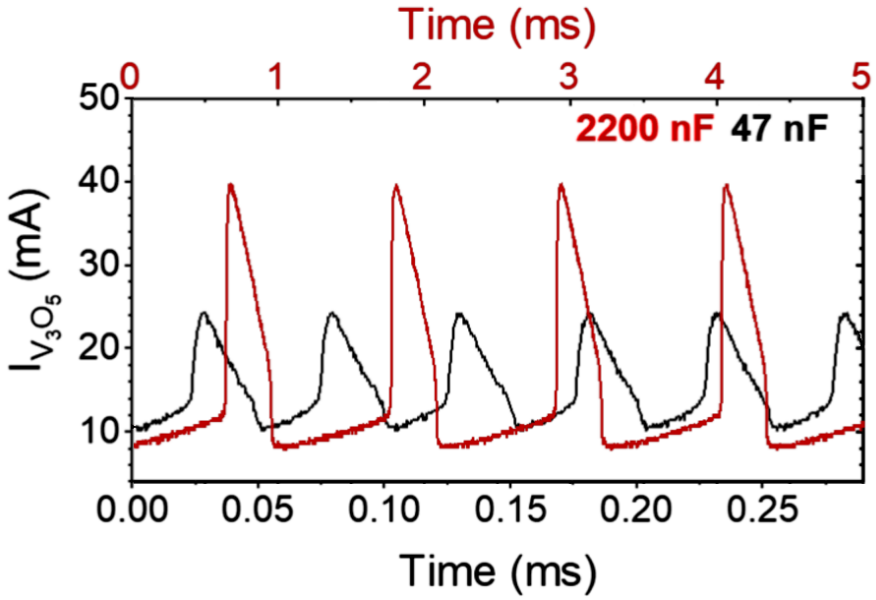

FIGURE 5.10 – Current measurements of V3O5 under a constant bias current and in parallel to a capacitor. Two different capacitance are employed : $C = 47$, and 2200 nf. The resistance of the sample, of the load resistor and the capacitance all affect the period of the oscillations. In particular, it is found that the period of the oscillations is proportional to $\tilde{R}C$, where $\tilde{R} = R_S||R_L$ is the series of the sample and load resistors. For more details see [Das+22]. Adapted from [Add+22]

a smooth resistivity vs temperature curve, which maps the temperature of a given cell of the model to its resistance. Such curve was obtained empirically by comparison with the experimental R(T) curve obtained in V3O5 experiments. We then added a capacitor in parallel to the MRN to model any capacitance that the overall circuit might have. Finally, we rounded the edges of the electrodes in order to reduce the point effect and focus the creation of the filament in the middle of the gap.

We proceeded to simulate the model under a ramp current, first in the case in which the capacitance was put to 0. We observed that the resulting IV curve was qualitatively comparable to the experimental one. The temperature maps produced by the simulations also indicated that the metallic filament, which forms during the resistive collapse, grows in width as the current is increased. This result is in agreement with the optical reflectivity maps that were produced in the V3O5 experiment. We then turned on the capacitance and repeated the previous simulations, observing that, after the voltage jump, the system enters an oscillatory regime, as evident from the IV curve. Eventually the amplitude of the oscillations start to decrease, until no oscillations are observed anymore. To better understand this oscillatory regime, we produced resistivity maps, from which we concluded that the rise and fall of the voltage coincide with the charge and discharge of the capacitor. Concurrently, the sample relaxes to the insulating state and then heats up once again, becoming metallic. As the bias is increased, the capacitor charges faster, the resistor network has less time to cool down and the metallic filament shrinks less and less at every new cycle, until eventually it stabilizes, ending the oscillatory regime. We then studied the system once a constant applied voltage, big enough to induce oscillations, was applied. This gave us the possibility to study more accurately the relation between resistance, voltage and the discharge current, and how a bigger capacitance can induce current oscillations with a bigger amplitude and a smaller frequency.

We compared the resistivity maps produced in the oscillatory regime to the optical reflectivity images of V3O5 experiments. While the temporal resolution of the experimental instrumentation is such that it was impossible to image the growth and subsequent relaxation of the metallic domain, we were able to interpret the time-averaged pictures as a superposition of the insulating and metallic states revealed by our resistivity maps. We then found further confirmation of the oscillatory regime in the experimental measurements of the sample current conducted at a constant bias current, which also confirmed our prediction that a bigger capacitance would result in oscillations with a bigger amplitude and a smaller frequency.

Chapitre 6

Coupled stochastic Mott oscillators

In the previous chapters we have studied two prominent features of Mott materials under an applied voltage : one is the stochastic nature of the resistive collapse, and the other is the oscillatory regime that is observed in the presence of a capacitance, which may be due to an external capacitor, like before, or the self capacitance of the sample, as it will be the case in this chapter. In this chapter we see how these two features can affect one another by considering the setup of Figure 6.1, in which two oscillating VO2 samples under an applied voltage, each with its own self capacitance, are coupled by an external capacitor. This configuration is of particular interest to us in that it may be considered a prototypical realization of two coupled oscillatory neurons.

If a constant voltage is applied to the circuit, the two samples will enter an oscillatory regime, as was the case for the V3O5 device of the previous chapter, the difference being that now the oscillations are induced by the self capacitance of the sample, rather than an external capacitor. If the coupling capacitor is removed from the setup, the devices will oscillate independently of one another. If the characteristics of the two samples, like the resistivity and geometry, are such that the samples have different voltage threshold values, their stochastic behaviour, as described by the probability of resistive collapse derived before (Eq. 3.13), will be different, and the one with the lower threshold will undergo faster oscillations. Therefore, while at first the two materials undergo the resistive collapse roughly at the same time, their oscillations are not synchronized and gradually grow apart (Fig. 6.2). Introducing a small coupling capacitor has the effect of synchronizing the two devices, which now switch to the metallic state in turns at regular intervals (Fig. 6.5, left panels). However, if the coupling capacitance is increased, disruption in the sequence of oscillations are observed ; in other words, the sample with lower voltage threshold will undergo the resistive collapse several consecutive times before the other sample can (Fig. 6.3 and Fig. 6.5, right panels). This is a surprising result, since intuitively one might expect that a greater coupling capacitance

would result in a stronger synchronization.

The applicability of coupled oscillators is not limited to spiking neural networks, but also extends to oscillator-based computing, which can be employed in a range of different problems and notably combinatorial tasks [CP20 ; Mal+20 ; Dut+21 ; Ahm+21]. Recently there has been a great interest in replacing CMOS oscillator circuits with devices based on quantum materials, such as Mott insulators, in order to reduce energy consumption and circuit footprint. Therefore, understanding how the stochasticity of coupled Mott oscillators can be tuned would represent an important step toward the realization of these systems.

In this chapter we use numerical simulations, that build on the theoretical results of the previous chapters, and chiefly the probability of filament percolation (Eq. 3.13), to model and understand the behaviour of the circuit of Figure 6.1. We show that, when there is no coupling capacitor, the inter-spike distributions of the two independent Mott neurons have a bell-shape. However, as the coupling capacitance is introduced and then increased, additional peaks emerge, and the distributions become multimodal. This indicates the emergence of disruptions in the sequence of oscillations, which break the regularity of the spike train. We find further confirmation of this in the voltage traces of the simulated Mott materials, which show how a big coupling capacitance induces the discharge of both samples when one of them fires, thus favouring the one with the lower voltage threshold, which will fire more frequently. Finally we compare our results with VO2 experiments, finding that they are in excellent qualitative agreement [Qiu+].

6.1 The model

We are interested in understanding the origin of the increasingly stochastic behaviour that emerges as the coupling capacitance C_0 of the circuit of Figure 6.1 is increased. When a small coupling capacitance is introduced, the two VO2 oscillators, which we represent with the colors red and black throughout the chapter, spike in turns : a spike from the red device is followed by one from the black device. However, as C_0 is gradually increased, disruptions in the sequence appear in the form of a spiking event that immediately follows a spike generated from the same device (so, for example, two consecutive spikes coming from the black device). To understand this behaviour it is not necessary to visualize the formation of the metallic filament within the insulating gap, for which reason we decided against using the MRN. However, it remains necessary to accurately predict the timings of the resistive collapse events which occur once a voltage has been applied to the devices. To do so we use the previously derived probability distribution of resistive collapse (Eq.3.13), which we report here for convenience sake.

$$P(V,t) = 1 - \frac{1}{1 + \frac{t}{\Delta t}\exp[(V - V_\theta)/\delta V]}. \tag{6.1}$$

Where V is the voltage across the sample, t is the time elapsed since the last collapse, Δt is the unit of time, so in other words the time step of the simulation, δV is the range of stochastic behaviour and V_0 the typical voltage at which the collapse occurs, i.e. the firing threshold. Therefore, since V_θ, δV and Δt are constant, one only needs to know the voltage of the sample and the time elapsed since the last spike or the beginning of the simulation to compute the probability of spiking. The rest of this section explores how the voltage of the sample may be derived by applying Kirchhoff laws.

In order to model the experimental setup the following assumptions were made. Firstly, a capacitor was put in parallel to each device in order to model the self capacitance presented by the experimental samples. Secondly, the resistance of the insulating state for both devices is assumed to be constant and equal to R_S. Finally, when the resistive collapse occurs and the current of the sample spikes, we assume that the voltage of the sample, V_S, goes to 0 and remains in that state for a fixed period of time, as to model the recovery phase of the sample during which the filament relaxes back to the insulating state. All of these considerations result in the circuit diagram that is shown in the right panel of Figure 6.1, which is to be compared with the experimental setup in the left panel.

We now move on to the issue of computing the voltage of the sample V_S by applying Kirchhoff laws. For the sake of simplicity we assume that all the constants of the circuit are the same for the left and right sides, including the load resistor R_0, the sample resistance R_S and the parallel capacitance C_P. In order to observe asynchronous oscillations the two devices should have different voltage thresholds, so we decide that the threshold of the left device should be 10% lower than that of the right device, i.e. $V_\theta^L = 90\% V_\theta^R$. All of the parameters used in the simulations are summarised in Table 6.1.

We begin by writing the current that flows though the left capacitor. From the application of KCL it follows that

$$I_{C_p}^L(t) = I_{R_0}^L(t) + I_{C_0}(t) - I_S^L(t) \tag{6.2}$$

We use the subscripts to designate a given component of the circuit, such as S for the sample, R_0 for the load resistor, C_0 for the coupling capacitor and C_p for the capacitor in parallel to the device; the superscripts are used to indicate the left or the right side of the circuit. Therefore, $I_{C_p}^L$ is the current of the left device capacitor, $I_{R_0}^L$ the current that flows through the left load resistor, I_{C_0} the current of the coupling capacitor and I_S^L that that flows through the sample. The

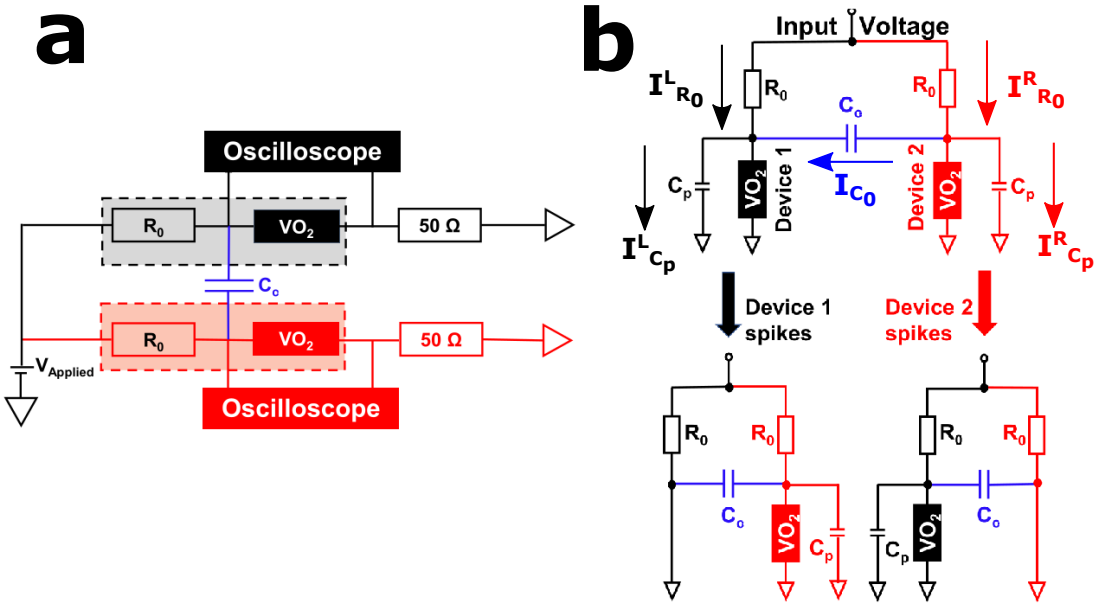

FIGURE 6.1 – Circuit diagram of the system under study. Left panel is the experimental setup, the right panel the simulated one. The only difference lies in the fact that, in order to model the oscillatory regime, an external capacitor C_P is added to the simulated circuit in parallel to each sample. When one of the devices spikes in our simulations, it's voltage is set to zero short-circuiting the coupling capacitor. Adapted from [Qiu+]

sign of the currents are conventional and the same as those of Figure 6.2 ; what is important is that they should be consistent throughout the derivation.

The current through the sample can be written as the sample voltage divided the sample resistance following Ohm's law $I_S^L(t) = V_S^L(t)/R_S$, and since the capacitor C_p and the sample are in parallel this is equal to

$$I_S^L(t) = \frac{V_{C_p}^L(t)}{R_S} \tag{6.3}$$

Inserting this expression into Equation 6.2 we obtain

$$I_{C_p}^L(t) = I_{R_0}^L(t) + I_{C_0}(t) - \frac{V_{C_p}^L(t)}{R_S} \tag{6.4}$$

From the equation of the capacitance $C = dQ/dV$ we may write the voltage of the left device capacitor as

$$V_{C_p}^L(t) = V_{C_p}^L(t - \Delta t) + \frac{I_{C_p}^L \Delta t}{C_p} \tag{6.5}$$

where Δt is the time-step of the simulation. This expression can be expanded by using the previously derived definition of the left device capacitor current Eq. 6.4

$$V_{C_p}^L(t) = V_{C_p}^L(t - \Delta t) + \left(I_{R_0}^L(t) + I_{C_0}(t) - \frac{V_{C_p}^L(t)}{R_S} \right) \frac{\Delta t}{C_p} \tag{6.6}$$

Grouping by $V_{C_p}^L(t)$ we obtain

$$V_{C_p}^L(t) = \frac{R_S C_p}{R_S C_p + \Delta t} \left[V_{C_p}^L(t - \Delta t) + \left(I_{R_0}^L(t) + I_{C_0}(t) \right) \frac{\Delta t}{C_p} \right] \tag{6.7}$$

For the right device it is possible to write a similar equation following the same steps

$$V_{C_p}^R(t) = \frac{R_S C_p}{R_S C_p + \Delta t} \left[V_{C_p}^R(t - \Delta t) + \left(I_{R_0}^R(t) - I_{C_0}(t) \right) \frac{\Delta t}{C_p} \right] \tag{6.8}$$

Our goal is computing the voltage of the sample using the above expressions so that the probability of spiking, which depends on the voltage, may be computed. We assume that the voltage at the previous time step $V_{C_p}^{L,R}(t - \Delta t)$ is known ; therefore the only unknown quantities are $I_{R_0}^L(t)$, $I_{R_0}^R(t)$ and $I_{C_0}(t)$.

Once again we focus our attention first on the left side of the circuit, and we consider the closed loop that consists of the voltage generator, the load resistor and the device capacitor. Applying KVL we obtain

$$
\begin{aligned}
I^L_{R_0}(t)R_0 + V^L_{C_p}(t) &= V_{app} \\
I^L_{R_0}(t) &= \frac{V_{app} - V^L_{C_p}(t)}{R_0}
\end{aligned} \tag{6.9}
$$

Simulations are carried in the voltage control regime and V_{app} is a known quantity. Therefore, we have expressed one of the missing variables, $I^L_{R_0}(t)$, in terms of the quantity that we want to compute, $V^L_{C_p}(t)$. If we take Equation 6.9 and we put it in Equation 6.7, we can then group by $V^L_{Cp}(t)$ arriving at

$$
\begin{aligned}
V^L_{C_p}(t)\left(1 + \frac{\Delta t R_S}{(R_S C_p + \Delta t)R_0}\right) =& \frac{R_S C_p}{R_S C_p + \Delta t}\left[V^L_{C_p}(t-\Delta t) + \frac{V_{app}/R_0 + I_{C_0}(t)}{C_p}\Delta t\right] \\
A =& \left(1 + \frac{\Delta t R_S}{(R_S C_p + \Delta t)R_0}\right) \\
B =& \frac{R_S C_p}{R_S C_p + \Delta t} \\
V^L_{C_p}(t)A =& B\left[V^L_{C_p}(t-\Delta t) + \frac{V_{app}/R_0 + I_{C_0}(t)}{C_p}\Delta t\right]
\end{aligned} \tag{6.10}
$$

Where all the constant pre-factors have been put into A and B for the sake of readability. Following similar arguments we can write for the right capacitor

$$
V^R_{C_p}(t)A = B\left[V^R_{C_p}(t-\Delta t) + \frac{V_{app}/R_0 - I_{C_0}(t)}{C_p}\Delta t\right] \tag{6.11}
$$

By looking at Equations 6.10 and 6.11 we may notice that it is possible to obtain an expression for $I_{C_0}(t)$, the last unknown quantity, by subtracting one from the other. Additionally, if we consider the closed loop made of the two device capacitors and the coupling capacitor, we can apply KVL to obtain the relation $V^R_{C_p}(t) - V^L_{C_p}(t) = V_{C_0}(t)$. It follows then that :

$$
\frac{B}{A}\left[V^R_{C_p}(t-\Delta t) - V^L_{C_p}(t-\Delta t) - 2\frac{I_{C_0}(t)\Delta t}{C_p}\right] = V_{C_0}(t) \tag{6.12}
$$

Expanding the voltage of the coupling capacitor in $V_{C_0}(t) = V_{C_0}(t-\Delta t) + I_{C_0}(t)\Delta t/C_p$ we can express the current $I_{C_0}(t)$ in terms of quantities that have been already computed at the previous time-step, and specifically

Name	Value (arb.units)	Definition
R_0	1.000	Load resistance
R_S	1.000	Sample resistance
C_p	0.500	Device capacitor
V_θ^L	0.450	Left device voltage threshold
V_θ^R	0.500	Right device voltage threshold
δ_V	0.005	Probability distribution width
V_{app}	1.000	Applied voltage
Δt	0.001	Time-step
τ_r	5.000	Relaxation time

TABLE 6.1 – Constants used in the simulations presented in this chapter. Several values for the coupling capacitance C_0 were adopted and they are reported in the appropriate figures and in the main text.

$$\frac{B}{A}\left[V_{C_p}^R(t-\Delta t) - V_{C_p}^L(t-\Delta t) - 2\frac{I_{C_0}(t)\Delta t}{C_p}\right] = V_{C_0}(t-\Delta t) + \frac{I_{C_0}(t)\Delta t}{C_0}$$
$$\frac{B}{A}\left[V_{C_p}^R(t-\Delta t) - V_{C_p}^L(t-\Delta t)\right] - V_{C_0}(t-\Delta t) = I_{C_0}(t)\Delta t\left(\frac{1}{C_0} + 2\frac{B}{AC_p}\right) \quad (6.13)$$

Equation 6.13 defines the current of the coupling capacitor in terms of constants and quantities that have been computed at the previous time step and are, therefore, known. It is the starting point to solve the system. Once the coupling current has been computed, it can be used to compute the voltage of the samples using equations 6.10 and 6.11. In turn the voltage allows us to compute the probability of observing a spiking event using Equation 6.1. If, by comparing a random number extracted from a uniform distribution between 0 and 1 to the probability of firing, we determine that one of the devices should undergo the resistive collapse, we set its voltage to zero and we keep it at that level for the duration of the relaxation time (which is fixed). No modifications other than resetting the voltage are needed in order to describe the electric breakdown and the simulation carries on according to the previously described equations.

6.2 Simulation results

The simplest case to start with is the one in which no coupling capacitor is present. In this case the devices will oscillate independently of each other. Since the two devices are characterized by the same set of parameters, except for the

firing threshold, which is lower in the left black device than in the red right one, we expect the former to feature a higher frequency of oscillations than the latter. This is indeed the case, as can be seen from Figure 6.2. In panel a) we plot the distribution of the voltage values at which the resitive collapse occurs. We notice that the black distribution has a lower mean value, as expected from the fact that the black device has a lower voltage threshold. Both distributions may be described as Poissonian, which follows from our use of Equation 6.1 to model the probability of resistive collapse. Indeed, as was already noticed in a previous chapter, the resistive collapse in Mott materials under an applied voltage is a Poissonian event whose probability can be described accurately by Equation 6.1 (see Figure 3.4). Panel b) shows the Inter Spike Intervals (ISI) distribution for the two devices. The ISI is defined as the period of time between the two most recent spikes. Faster oscillations result in smaller ISI, which explains why the distribution for the black device is centered around a lower mean value than that of the red device. The shape of the two ISI distributions closely follow that of the firing voltage. The inset shows the distributions for the experimental oscillators, which is shown and discussed in more details in the section dedicated to the experimental results. In panels c) and d) we plot the voltage traces of the two devices, from which it can be appreciated how a smaller voltage threshold in the black one results in faster oscillations with slightly smaller amplitudes, as could be expected from our analysis of the ISI and firing voltage distributions.

We now consider the case in which a coupling capacitor C_0 is introduced in the circuit, as shown in Figure 6.1. The introduction of the capacitor has the effect of synchronizing the oscillators, which now spike in turn instead of overlapping each other. However, occasionally it may occur that the sequence of alternating spikes from the black and red device is disrupted by two or more consecutive spikes generated by the same device. Interestingly, as the value of the coupling capacitance is increased, the number of disruptions also grows. This can be appreciated from Figure 6.3. In panel a) we plot the percentage of disruptions against the value of the coupling capacitance, in logarithmic scale. The inset shows the experimental results. In panel b) we show three spike trains for the following value of the coupling capacitance : from top to bottom $C_0 = 1, 5, 10$ arb. units. The color turquoise is used to mark a disruption event. Panel c) shows the spike trains of the experimental VO2 oscillators.

Plotting the ISI interval distribution also allows us to appreciate the increase in disruption events as the coupling capacitance is increased. Indeed, a disruption results in a shortened ISI for the device that spikes and a prolonged ISI for the device that could not spike and has to wait for the next turn. Therefore, we expect the simple Poissonian distribution that we observed in the absence of a coupling capacitor to become a multimodal distribution. This is precisely the case, as can

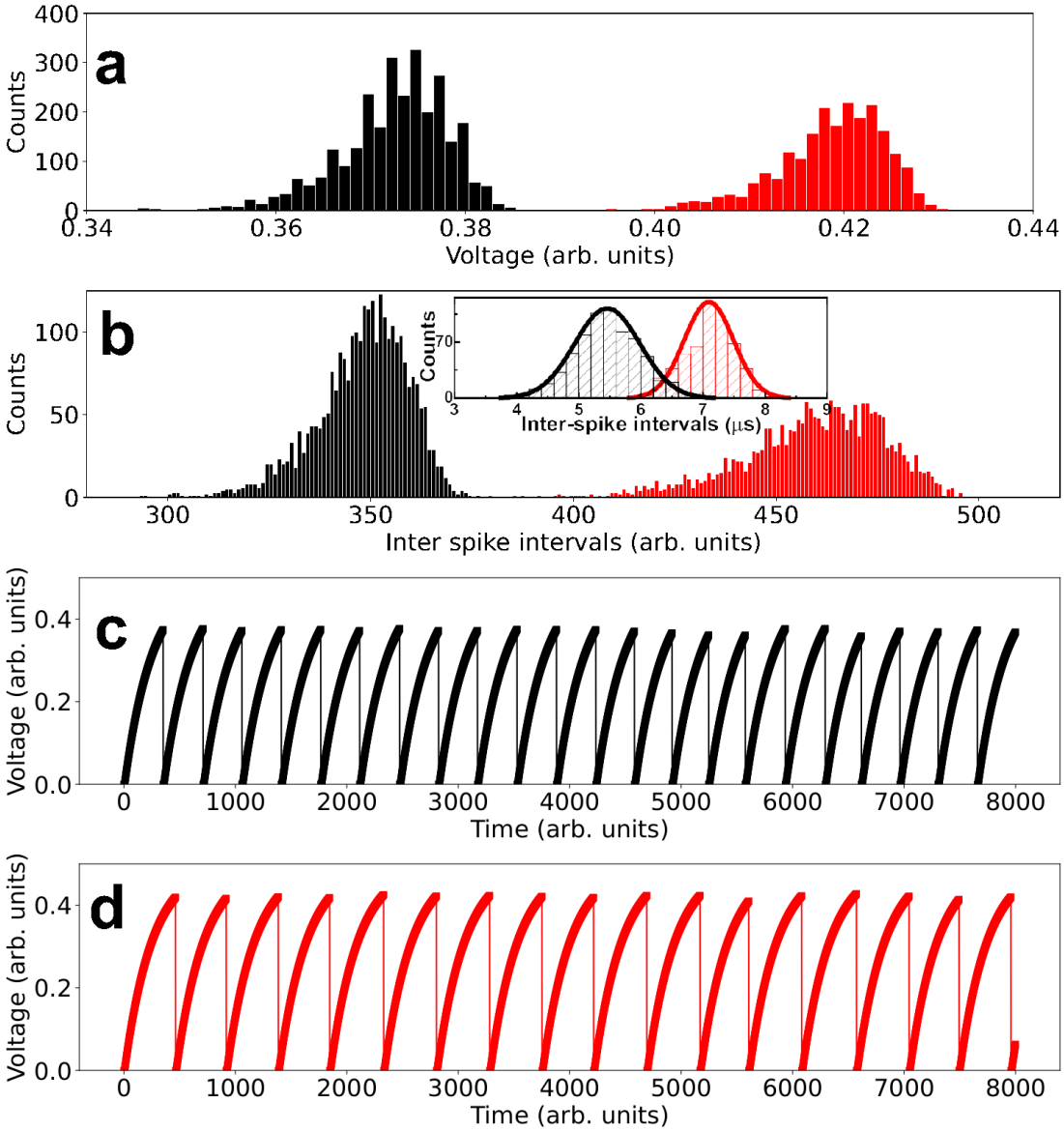

FIGURE 6.2 – Behaviour of the two simulated devices when they spike independently of one another in the absence of a coupling capacitance. a) Distribution of the voltages at which the devices undergo the resistive collpase (black for the left device, red for the right one) b) Distribution of the ISI. The inset shows the distribution of the ISI of two coupled VO2 oscillators as measured in experiments (see next section "Experimental results"). c) d) Voltage traces of the devices.

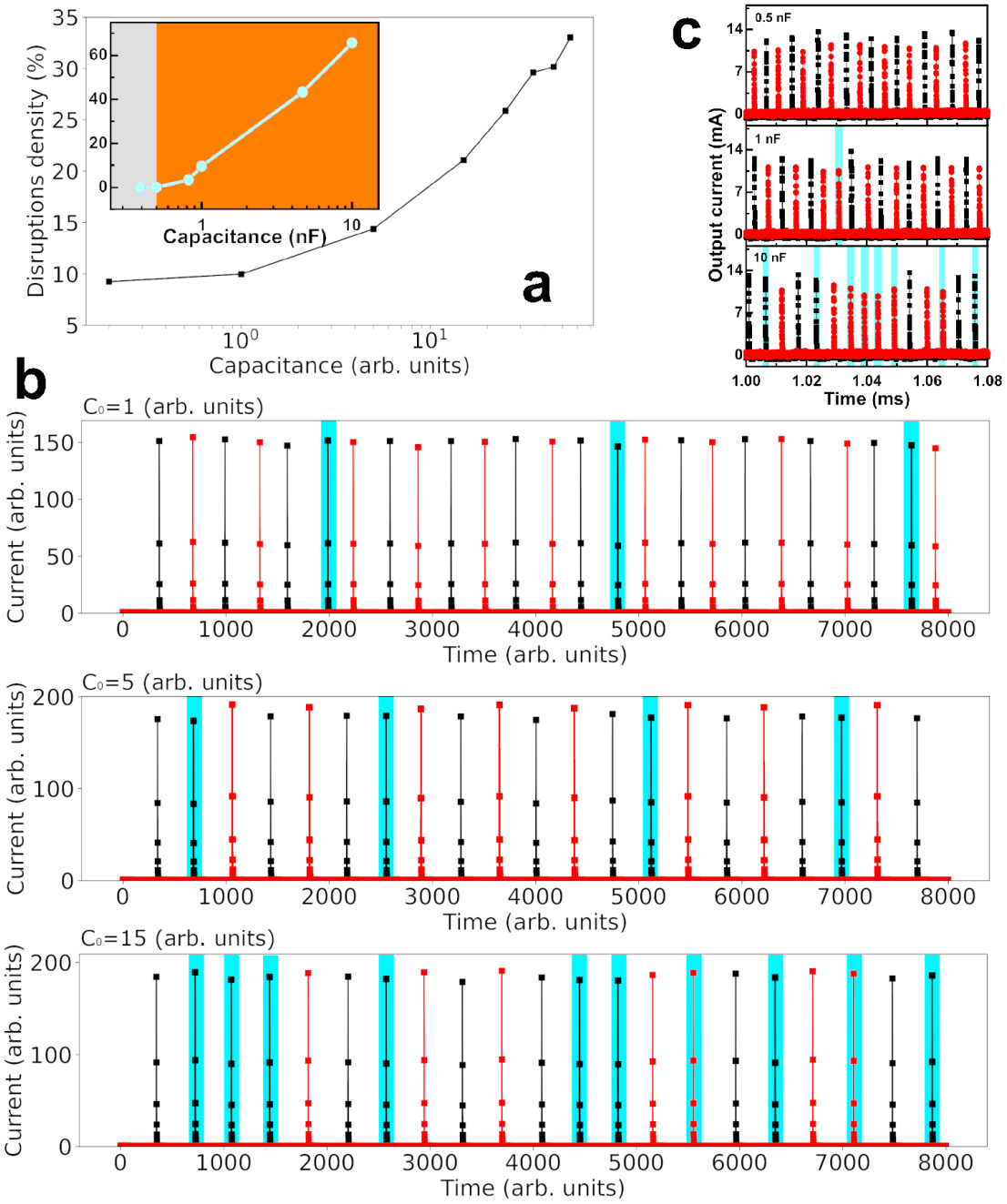

FIGURE 6.3 – Effect of the coupling capacitance on the spiking sequence of the simulated devices. Panel a) percentage of disruptions against the coupling capacitance, in logarithmic scale. The inset shows the percentage of the disruptions in a experimental setup with two coupled VO2 oscillators (see next section "Experimental results"). Panel b) output current of both samples against time for three values of the coupling capacitance (from top to bottom : $C_0 = 1, 5, 10$ arb. units). The colors red and black indicate the two samples, the color turquoise is used to emphasize the disruptions. Panel c) output currents of two coupled VO2 oscillators in an experimental setup (see next section "Experimental results").

be seen from Figure 6.4

In particular, in the top panel, in which $C_0 = 1$ arb. units, we observe that both the red and black distributions have two peaks. The highest one corresponds to the regular ISI unaffected by disruptions, whose value can be compared with the period of the current oscillations. For instance, for the black device we see from the distribution of Figure 6.4 that the average ISI is approximately $t = 600$ arb. units, which is precisely the time interval between two black spikes separated by one red spikes in panel b) of Figure 6.3. The smaller peak corresponds to an ISI approximately half the length of the regular ISI : this the case in which one disruption event occurs, and the same device spikes two consecutive times. On the other hand, for the red device we see that the smaller peaks is centered around a value which is greater than the regular ISI by roughly half its length : this is the interval between two red spikes that are separated not by one, but by two black spikes (i.e. when a disruption occurs).

As we increase the coupling capacitance in the middle and bottom panels of Figure 6.4 ($C_0 = 5$ and $C_0 = 15$ arb. units, respectively), we see the emergence of additional peaks corresponding to ISI which are either multiples or half the length of the regular ISI (the insets with magenta borders show zoomed-in sections of the graph to better appreciate them). These additional peaks are due to the increased capacitance, which result in more disruptions and occasionally sequences of three or more consecutive spikes generated by the same device.

We now turn to the problem of understanding the mechanism by which disruptions arise as the coupling capacitance is increased. To do that we may take a look at the voltage traces that are plotted in Figure 6.5, focusing on the simulation results for now. In the left panel we see the voltages traces of both devices when the coupling capacitance equals $C_0 = 0.5$ arb. units, whereas in the right panel the capacitance is equal to $C_0 = 10$ arb.units. Red and black stripes are used to indicate which device spikes, and stripes with thicker outlines correspond to disruptions events. As expected, when the coupling capacitance is higher more disruptions appear. We also notice that, when the capacitance is small, a spike produced by a certain device results only in the partial discharge of the other ; however, as the capacitance is increased, the discharge is almost complete, similarly to what happens to the device that has produced the spike. This explains why the number of disruptions increases with the coupling capacitance : if the voltage of the device that has not spiked is reset only partially, it will reach the threshold voltage faster than the device that has spiked (whose voltage is always reset to 0 regardless of the value of the coupling capacitance). This mechanism assures that the two devices will take turn in firing. However, if both devices are subjected to a near total reset of the voltage, the one to fire first will generally be the device with the lower voltage threshold (the black one in our case), possibly resulting

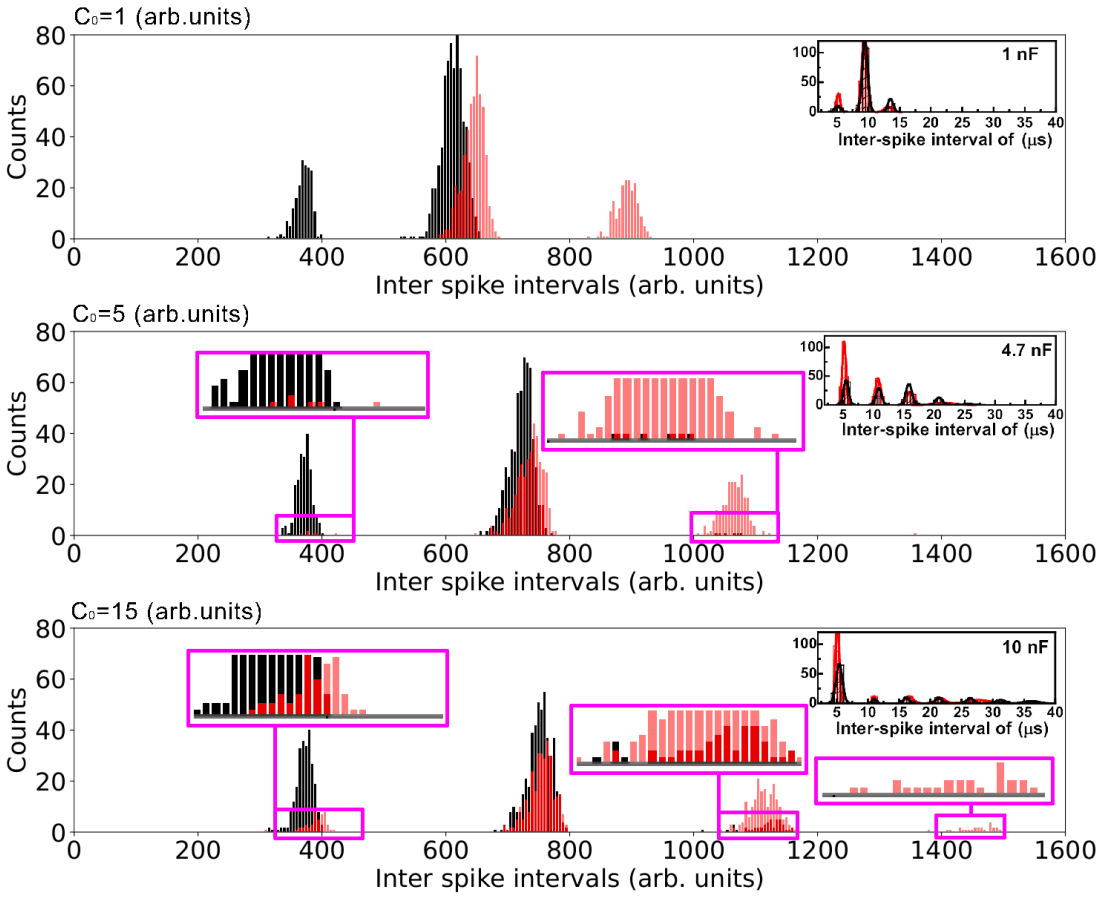

FIGURE 6.4 – Evolution of the ISI distribution of the simulated devices as the coupling capacitance is increased. From top to bottom $C_0 = 1, 5, 15$ arb. units. As the capacitance is increased additional peaks appear. The color red is semi-transparent in order to appreciate the overlap between the distributions. The insets with magenta borders in the middle and bottom panels are zoomed in visualizations. The insets in the top right corner of each panel show the ISI distributions of the coupled VO2 oscillators of an experimental setup (see next section "Experimental results").

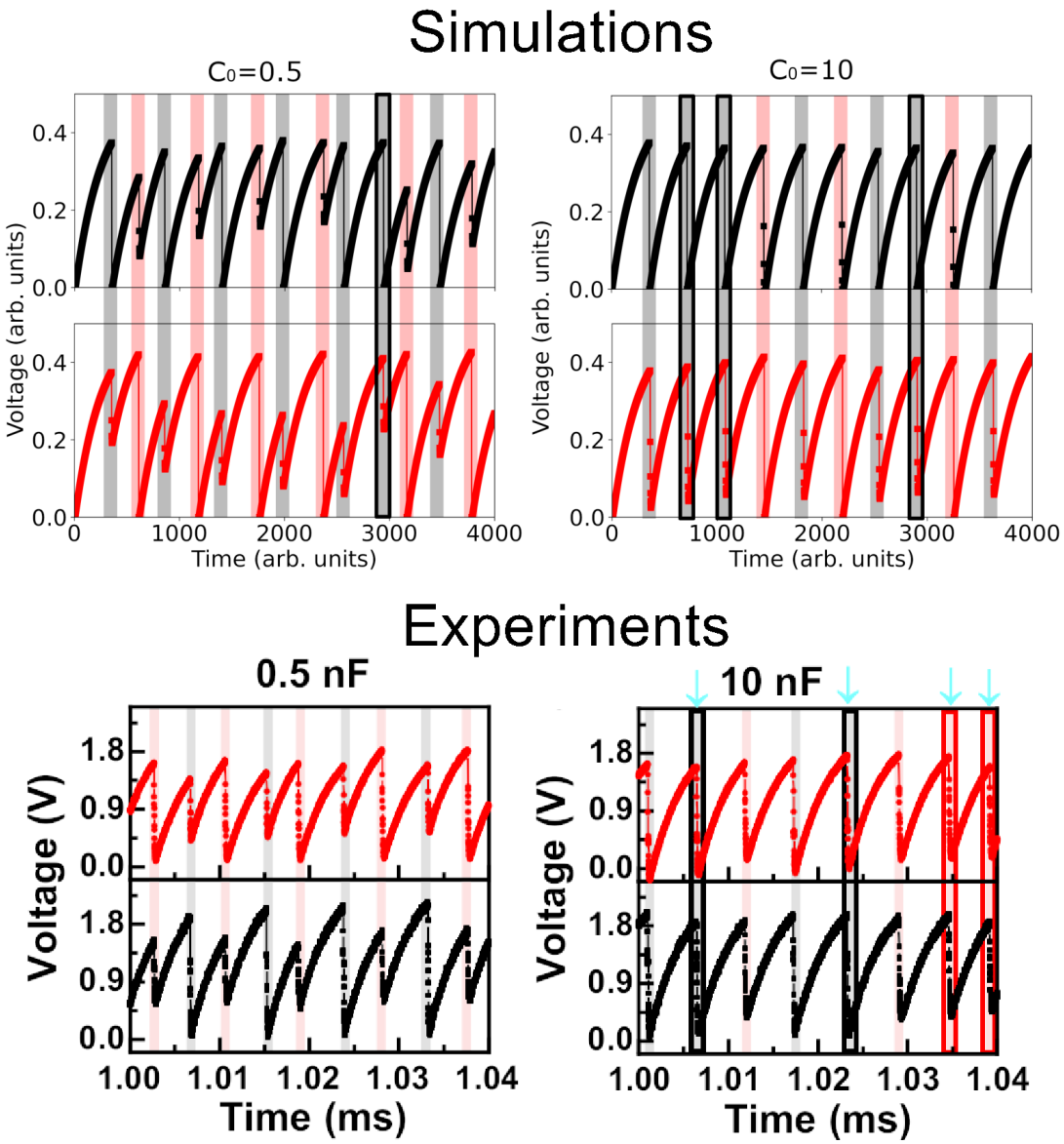

FIGURE 6.5 – Voltage traces of the two devices when a coupling capacitance is introduced. Top panels are from the simulations and bottom ones from the experiments. In both experiments and simulations, the black color is used for the device with the faster firing rate, consistently with the other figures. Looking at the simulations results, in the left panels the coupling capacitance is $C_0 = 0.5$ arb. units, in the right ones it is $C_0 = 10$ arb. units. The gray and light red bars are used to indicate which device spikes : a light red bar indicates that the device whose voltage trace is also red has reached the voltage threshold first and has produced a spike. Whenever a bar has thick borders it means that it represents a disruption in the spiking sequence. More details on the experimental results are given in the next section.

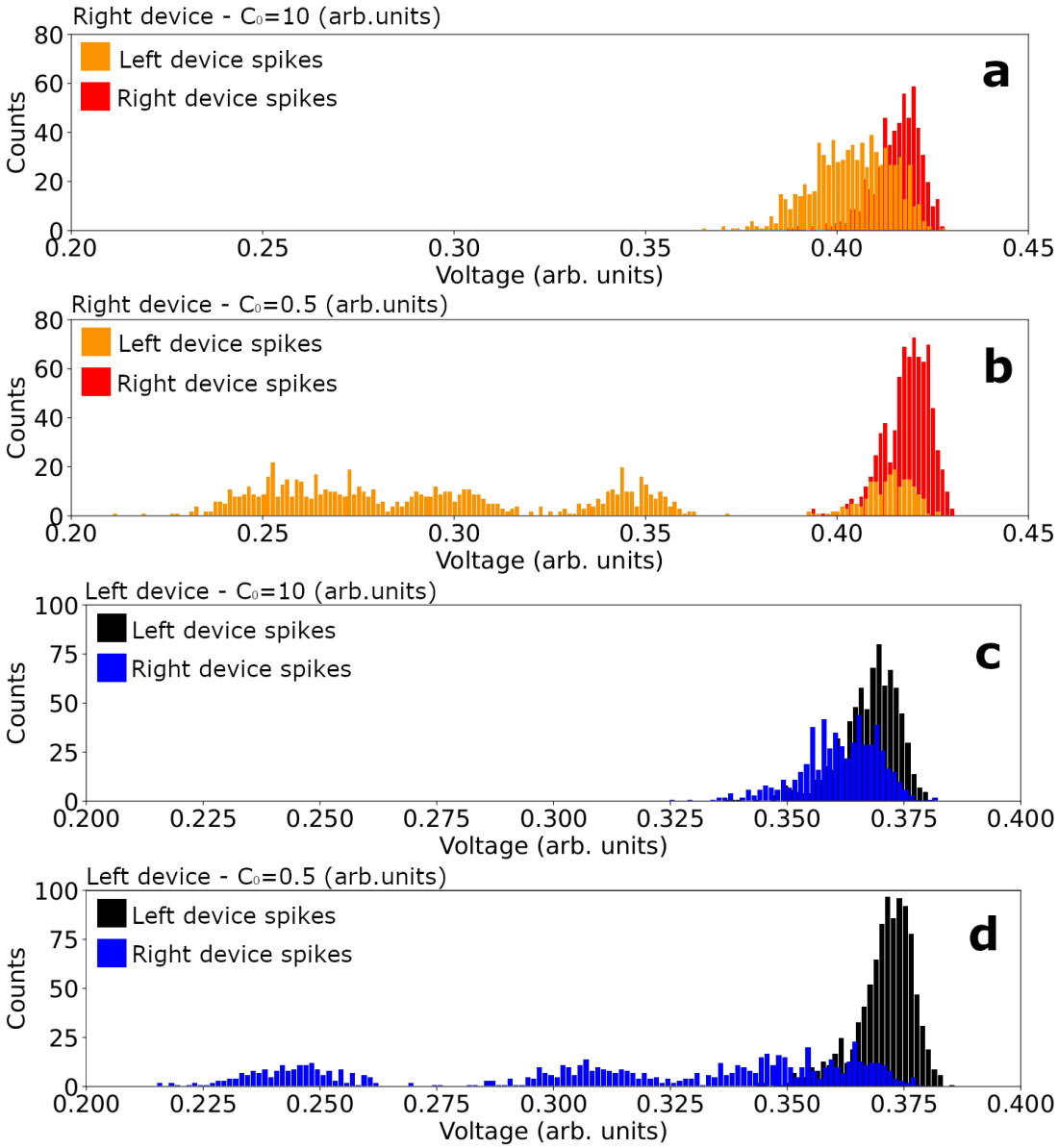

FIGURE 6.6 – Sample voltage distributions for different value of the coupling capacitance. Each panel features two distributions, both of which belong to either the left (cool colours) or the right (warm colours) device. The difference between the two is that the distribution with the stronger colour (red or black) represents the voltage of the sample when it itself spikes, while the distribution with the weaker colour (orange or blue) represents the voltage of the sample when the other sample spikes.

in sequences of multiple consecutive spikes produced by the same device. As for the reason why a bigger coupling capacitance results in a stronger discharge, by taking a look at Figure 6.1 one may notice that, after a given device has spiked, the coupling capacitor becomes in parallel to the other device capacitor. This may also be understood as the sample that has not spiked now having a capacitance equal to the sum of its own capacitance and that of the coupling capacitor, i.e. $\tilde{C_p} = C_p + C_0$. From the equation of the capacitor we know that $V = Q/C$, so the sudden increase in the capacitance parallel to the sample causes a drop of the voltage which is proportional to the capacitance itself, and specifically that of the coupling capacitor.

In Figure 6.6 we plot the voltage distributions of the two samples, when either of them spikes, for different values of the coupling capacitance. From top to bottom we have : a) right device voltage distributions when $C_0 = 10$ arb. units and b) when $C_0 = 5$ arb. units ; c) left device voltage distributions when $C_0 = 10$ arb. units and d) when $C_0 = 5$ arb. units. Each panel contains two distributions, one representing the voltage of the device when it spikes, the other the voltage of the device when the other device spikes. From this figure we can appreciate how, when the coupling capacitance is increased, the two distributions become much more similar (panel a) and c)). In other words, a near complete discharge of the sample that has not fired allows the other device to also reach near threshold voltage values. As an example, we may focus on the left device, panel c) and d). In panel d), when the coupling capacitor is small, we see that the voltage values attained by the left device when the right one spikes are generally smaller than the threshold for firing, which we identify with the mean of the black distribution. This occurs because the right device only partially discharged the last time the left one spiked, due to the small coupling capacitance, and thus was able to reach its own firing threshold in a short amount of time, not enough for the left device, whose voltage was set to 0, to charge back. On the other hand, when C_0 is increased (panel c)), the discharge of the right device is almost complete, and thus the left device has enough time to charge back and reach the firing threshold.

6.3 Experimental results

We now move on to comparing our findings with experimental results obtained from a system of coupled VO2 oscillators, depicted in panel a) of Figure 6.1. Firstly, we consider the case in which no coupling capacitor is present, and the two devices are independent. In this setup (panel a) of Figure 6.7), dc voltage produced by a function generator is applied to a 100×400 nm2 VO2 nanodevice with an estimated self capacitance of 0.2 nF that is connected in series with a load resistor. A multichannel oscilloscope is used to monitor the voltage on nanodevice

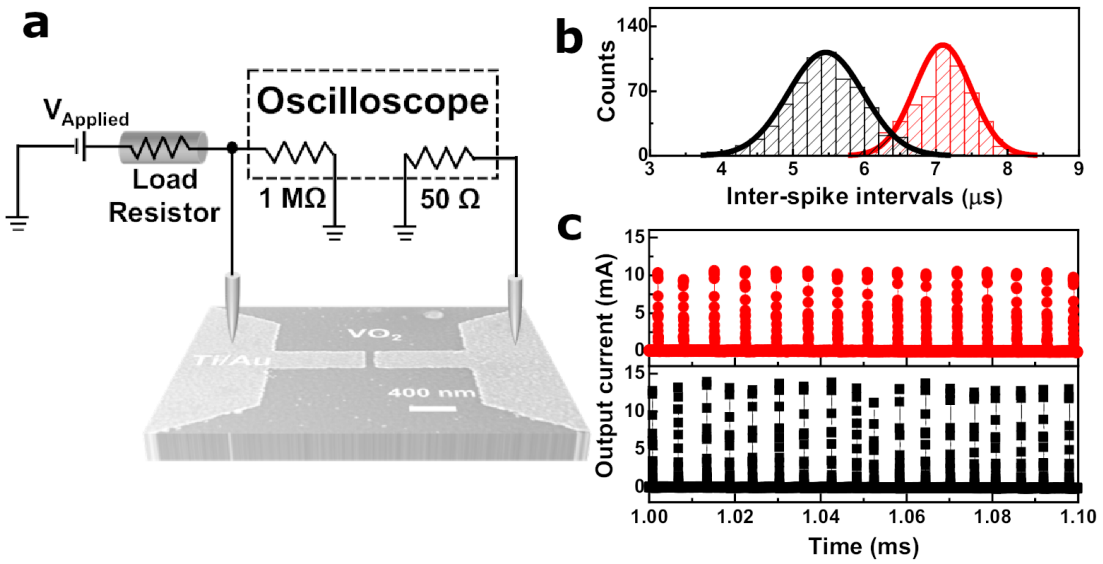

FIGURE 6.7 – Panel a) : Experimental setup. Panel b) : ISI distributions of the two uncoupled VO2 samples. Panel c) : Current readings of the uncoupled devices. Adapted from [Qiu+]

and the current flowing in the circuit. Figure 6.7 shows the current readings for the two indipendent device (panel c)), as well as the distribution of ISI (panel b)). These results are qualitatively comparable with our simulations, and specifically Figure 6.2, where we show the voltage traces and the ISI distributions of the two uncoupled devices.

We now consider the case in which the coupling capacitor is introduced. In Figure 6.8 panel a) we plot the percentage of disruption events as a function of the coupling capacitance, and in panel b) we plot the current readings for three different values of the coupling capacitance : from top to bottom $C_0 = 0.5$, $C_0 = 1$ and $C_0 = 10$ nF. Like before turquoise stripes designate disruptions. We note that the data presented in the figures were recorded in the same pair of VO2 nanodevices that were studied before independently and that the only modification needed to induce stochastic disruption events in the alternating spiking sequence was introducing the coupling capacitance. We observed similar behavior in multiple pairs of different VO2 nanodevices, therefore the emergence of disruption events in the deterministic alternating spiking sequence is not accidental, but rather a general property of these coupled spiking oscillators. These experimental results may be compared with our simulations, and in particular Figure 6.3, where we plot both the disruptions density and the currents reading for different values of the coupling capacitor.

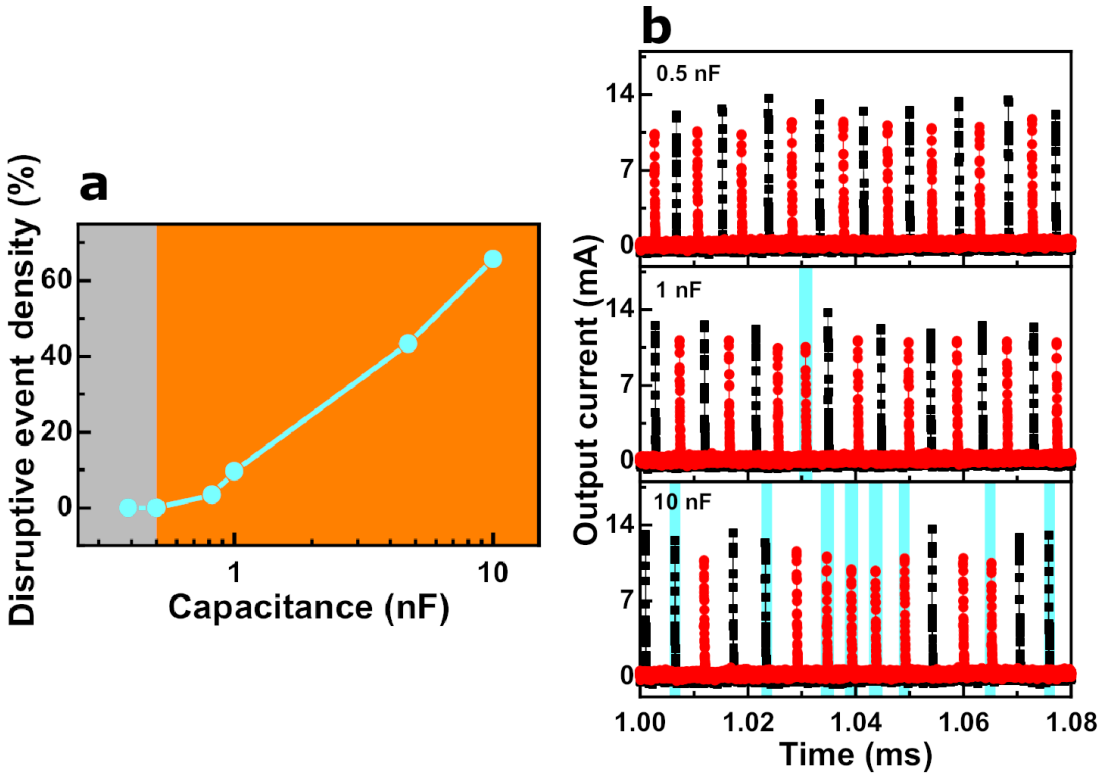

FIGURE 6.8 – Panel a) : Percentage of disruptive events plotted against the coupling capacitance in logarithmic scale. No disruptions was observed in the gray area, whereas the color orange designates the region within which disruptions start appearing. Panel b) : Output current readings of the two devices for three values of the coupling capacitance. From top to bottom $C_0 = 0.5$, $C_0 = 1$ and $C_0 = 10$ nF. The color turquoise marques disruptions in the spiking sequence.

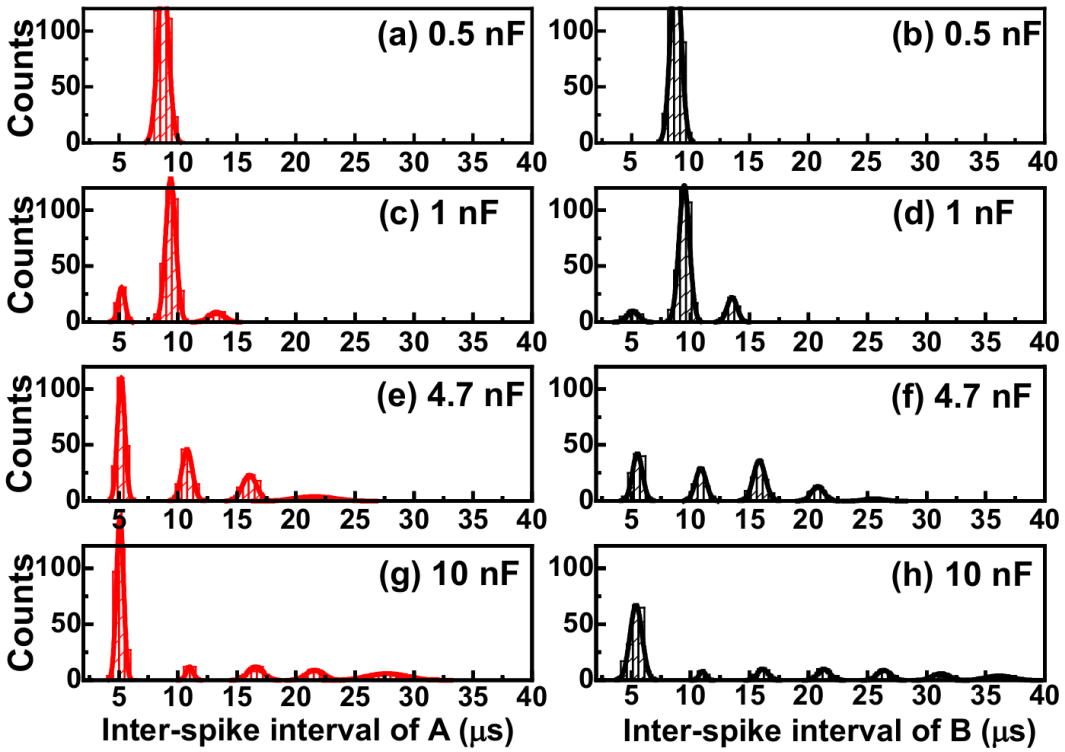

FIGURE 6.9 – ISI distribution for the two VO2 nandodevices as the strength of the coupling capacitance is increased. From top to bottom the values of the coupling capacitance are : 0.5, 1.0, 4.7, 10 nF. Adapted from [Qiu+]

In Figure 6.9 we plot the experimental ISI distribution for both devices and several values of the coupling capacitance, from which we can appreciate the emergence of additional peaks as the capacitance is increased, as was the case for our simulations (Figure 6.4).

Finally in Figure 6.10 we show the voltages traces of the two devices for two different values of the coupling capacitance. As was the case for the simulations, a small coupling capacitance results in a partial discharge of the oscillator that has not spiked, allowing it to reach the firing threshold before the other and thus ensuing the synchronized alternating sequence of black and red spikes. On other other hand when the capacitance is big even the device that does not spike discharges almost completely, resulting in a race between the two devices to reach the firing threshold and, occasionally, in disruptions due to the intrinsically different stochastic behaviours of the devices (which can be appreciated in Figure 6.7 where no coupling capacitor is present).

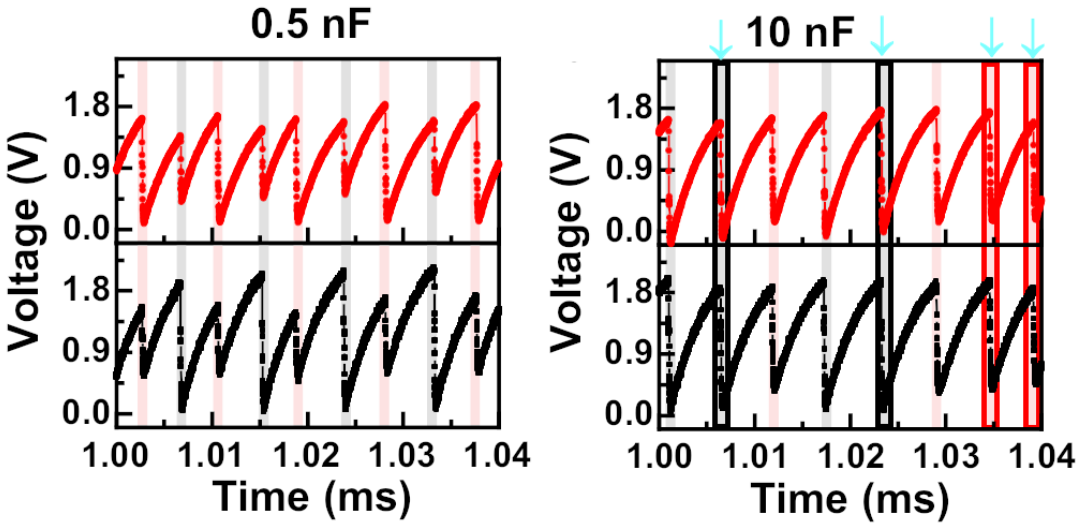

FIGURE 6.10 – Voltage traces of the experimental nanodevices when a coupling capacitor of 0.5 (left panels) and 10 nF (right panels is introduced). The arrows and the thicker outlines indicate a disruption. Adapted from [Qiu+]

6.4 Conclusion

In this chapter we have explored the effects of coupling two VO2 oscillators using a capacitor. This has given us the opportunity to further investigate two topics that we have encountered in the previous chapters : the stochastic nature of the resistive collapse of Mott materials under an applied voltage and their oscillatory regime. To do so we developed a numerical model in which a capacitor was added in parallel to each oscillator, in order to account for the self capacitance of the experimental samples, and the previously derived probability of filament percolation (Equation 6.1) was used to predict the timing of the resitive collapse. Firstly we applied this model to the simple case in which no coupling capacitor is present, and the two oscillators are independent. As expected, no synchronicity between the oscillators was observed ; we plotted the distribution of the two devices voltages at the time of firing, finding that they have a Poissonian shape, which follows from our use of (Equation 6.1), which describes the resistive collapse as a Poissonian process. We also plotted the distribution of the Inter Spike Intervals (ISI) of the two independent oscillators, whose shape closely follow that of the voltage distributions.

We then considered the case in which a coupling capacitor was introduced, which results in the synchronization of the two devices, which now take turns in firing. In other words, a spike from a certain device is followed by a spike from the

other device, an so on for the rest of the simulation. However, when the coupling capacitance is increased, disruptions in the spiking sequence emerge, in the form of one or multiple consecutive spikes produced by the same device. Interestingly, the percentage of disruptions increase with the coupling capacitance. This can be appreciated not only from the readings of the currents that flow through the devices, from which we can see that sometimes the same device undergoes the resistive collapse two or more consecutive times, but also from the ISI distribution. Indeed, while in the previous case, when no coupling capacitor was present, both devices had simple Poissonian distributions, as the coupling capacitance is increased additional peaks appear. For instance, we observe an extra peak centered around a value half that of the regular ISI. This peak corresponds to the occurrence of a single disruption event, in which the same device spikes twice with no interruption from the other one, resulting in a ISI half the length of the regular period of oscillations. We also observe peaks centered around ISIs which are multiples of the oscillations period, which we connect to the opposite scenario, in which the device is prevented by one or multiple disruption from firing when it should be, and has to wait for at least the next turn.

In order to understand this unexpected stochastic behaviour we looked at the voltage traces of the oscillators for two different values of the coupling capacitance. We observed that, in both cases, when one device undergoes the resistive collapse, and its voltage goes to zero, the other device also discharges ; however, the discharge is found to be proportional to the coupling capacitance. Therefore, while the device that spikes always has its voltage set to zero, as an effect of the switching to the metallic state, only a big coupling capacitance results in the almost complete discharge of the other device. In this case, after the spike both devices will begin the charging phase from a starting voltage close to zero, and the one with the lower voltage threshold will tend to fire first, possibly resulting in sequences of consecutive spikes produced by the same device. On the other hand, if the coupling capacitance is smaller, the discharge of the device that does not spike won't be as important, and this will allow it to fire first at the next turn even if its voltage threshold is higher. To understand why the coupling capacitance affects the discharge of the device, we may assume that, when one device spikes, its resistance momentarily goes to zero. In that case the coupling capacitor will become in parallel with that of the device that did not spike, thus increasing the total capacitance. It is this sudden increase in the capacitance that causes the sample to discharge, therefore the higher the coupling capacitance, the bigger the discharge.

Finally, we compare our numerical results with measurements conducted on a system of coupled VO2 oscillators. In particular we look at the ISI distribution with and without the coupling capacitor, as well as the current output, the voltage traces

and the percentage of disruptions for different value of the coupling capacitance. In all cases we found qualitative agreement with our simulations.

Chapitre 7

Conclusion

In today's world there is a increasingly high demand for smart devices capable of executing tasks that were once thought to be beyond the reach of computers. Neural networks have emerged as the most appropriate computational paradigm to achieve this lofty goal ; however, modern hardware implementation of neural networks often rely on the same CMOS technology that powers traditional computers, old and new alike. This comes at the expense of power efficiency, which is far below that of the human brain. In order to build a future in which the proliferation of smart devices becomes environmentally sustainable, the current trend of ever increasing computational prowess must be accompanied by an equally important reduction of the energy footprint of these devices. Therefore, in addition to the shift in design from the classic Von Neumann architecture to modern Deep Neural Networks, an equally important step must be taken toward the development of new technologies alternative to CMOS for the implementation of hardware neural networks.

Quantum materials are excellent candidates for implementing neural networks at a fraction of the energy cost of traditional CMOS implementation. This advantage comes from the neuromorphic features that some of these materials possess, which allow them to be used as both neurons and synapses in hardware neural networks, as well as their intrinsic potential for miniaturization, that could go beyond the limits of current CMOS fabrication terminology. Among these materials we studied the family of the Mott insulators, such as VO2 and V2O3, which possess several neuromorphic properties and chiefly a volatile resistive collapse that can occur under different conditions. This physical phenomenon is key to implementing the spiking functionality of biological neurons : when the resistance of the material collapses a surge in the current that flows through the sample is recorded, which may be compared with the spike that ensues the depolarization of the neuronal membrane. Interestingly, this resistive collapse may be induced by application of a voltage and at temperatures close to room temperature, thus making it possible

to integrate Mott materials with traditional electronic circuit with ease.

However, the characterization of Mott materials, which is necessary to their deployment in real world applications, is a challenging topic, since the Insulator to Metal Transition (IMT) that these materials undergo is a complex physical phenomenon that stems from the interaction of many coupled electrons under a strong electric field. Thus it becomes necessary to adopt a more phenomenological view, and to develop the appropriate numerical models, to make contact with the experiments. In this work we present the Mott Resistor Network (MRN), a mesoscopic phenomenological model of a Mott material under an applied voltage, in which the sample is described as a network of resistors with a variable resistance that depends on the temperature. Using this model we were able to investigate the field driven resistive switching in Mott materials and to further understand their neurmorphic properties. In particular, the most important contributions of our study are :

1. The understanding of the field induced resistive switching as a thermo-electronic process in which both thermal and electronic effects, in the form of Joule heating and current density concentration respectively, play an important role
2. The characterization of the metallic filament percolation, that triggers the resistive collapse, as a stochastic Poissonian process, comparable on a quantitative basis with the noisy firing of the exponential escape rate neuronal model.
3. The systematic study of how different properties of the sample, and chiefly the thermal conductivity to the underlying substrate and the ratio of its insulating to metallic resistance, can affect the stochastic behaviour.
4. The discovery that certain properties of the resistive switching, such as the effect of the resistivity ratio on the incubation times, can be generalized to materials other than VO2 and V2O3, such as the nickelates NdNiO3 and SmNiO3.
5. The characterization of the oscillatory regime that emerges when a current ramp is applied to a sample in parallel to a capacitor, which is of particular interest in the context of neuromoprhic computing due to the oscillatory nature of neuronal patterns.
6. The description of the dynamics of a system of coupled VO2 oscillators, and in particular the increasingly stochastic behaviour, in the form of disruptions of the expected sequence of alternating spikes coming from both devices, that emerges when the coupling capacitance is increased, a result whose relevance extends beyond the field of hardware neural networks to that of oscillatory computing.

In so doing we have extended the original MRN model to account for the peculiarity of the different materials that we've studied, such as VO2, V2O3, V3O5, SmNiO3 and NdNiO3, which present different transitions, of first and second order, and different physical properties, such as the presence of a self capacitance, or the lack thereof. It is our hope that our work will contribute to the development of energy efficient neural networks that can meet the needs of modern society.

Bibliographie

[Add+18] Coline Adda et al. "Mott insulators : A large class of materials for Leaky Integrate and Fire (LIF) artificial neuron". In : *Journal of Applied Physics* 124.15 (2018), p. 152124.

[Add+22] Coline Adda et al. "Direct Observation of the Electrically Triggered Insulator-Metal Transition in V 3 O 5 Far below the Transition Temperature". In : *Physical Review X* 12.1 (2022), p. 011025.

[Ahm+21] Ibrahim Ahmed et al. "A probabilistic compute fabric based on coupled ring oscillators for solving combinatorial optimization problems". In : *IEEE Journal of Solid-State Circuits* 56.9 (2021), p. 2870-2880.

[All+88] Tim Allen et al. "Orientation-selective VLSI retina". In : *Visual Communications and Image Processing'88 : Third in a Series*. T. 1001. SPIE. 1988, p. 1040-1046.

[Bro+14] Justin S Brockman et al. "Subnanosecond incubation times for electric-field-induced metallization of a correlated electron oxide". In : *Nature nanotechnology* 9.6 (2014), p. 453-458.

[Cat+18] Sara Catalano et al. "Rare-earth nickelates RNiO3 : thin films and heterostructures". In : *Reports on Progress in Physics* 81.4 (2018), p. 046501.

[CBG00] G Catalan, RM Bowman et JM Gregg. "Metal-insulator transitions in NdNiO 3 thin films". In : *Physical Review B* 62.12 (2000), p. 7892.

[CD14] David Daniel Cox et Thomas Dean. "Neural networks and neuroscience-inspired computer vision". In : *Current Biology* 24.18 (2014), R921-R929.

[CDt20] Chris73, Diberri et tiZom. *English Wikipedia*. CC BY-SA 3.0. 2020. url : `https://commons.wikimedia.org/w/index.php?curid=2241513` (visité le 23/02/2022).

[Chu71] Leon Chua. "Memristor-the missing circuit element". In : *IEEE Transactions on circuit theory* 18.5 (1971), p. 507-519.

[CP20] Gyorgy Csaba et Wolfgang Porod. “Coupled oscillators for computing : A review and perspective”. In : *Applied physics reviews* 7.1 (2020), p. 011302.

[Das+22] Sujan Kumar Das et al. “Physical Origin of Negative Differential Resistance in V3O5 and Its Application as a Solid-state Oscillator”. In : *Advanced Materials* (2022), p. 2208477.

[Dav+18] Mike Davies et al. “Loihi : A neuromorphic manycore processor with on-chip learning”. In : *Ieee Micro* 38.1 (2018), p. 82-99.

[Dav04] Timothy A Davis. “Algorithm 832 : UMFPACK V4. 3—an unsymmetric-pattern multifrontal method”. In : *ACM Transactions on Mathematical Software (TOMS)* 30.2 (2004), p. 196-199.

[Del+18] Javier Del Valle et al. “Challenges in materials and devices for resistive-switching-based neuromorphic computing”. In : *Journal of Applied Physics* 124.21 (2018), p. 211101.

[Del+21] Javier Del Valle et al. “Spatiotemporal characterization of the field-induced insulator-to-metal transition”. In : *Science* 373.6557 (2021), p. 907-911.

[Die+18] P Diener et al. “How a dc electric field drives Mott insulators out of equilibrium”. In : *Physical Review Letters* 121.1 (2018), p. 016601.

[Don+98] John P Donoghue et al. “Neural discharge and local field potential oscillations in primate motor cortex during voluntary movements”. In : *Journal of neurophysiology* 79.1 (1998), p. 159-173.

[Dut+21] Suryendy Dutta et al. “An Ising Hamiltonian solver based on coupled stochastic phase-transition nano-oscillators”. In : *Nature Electronics* 4.7 (2021), p. 502-512.

[Fri05] Pascal Fries. “A mechanism for cognitive dynamics : neuronal communication through neuronal coherence”. In : *Trends in cognitive sciences* 9.10 (2005), p. 474-480.

[Fuk75] Kunihiko Fukushima. “Cognitron : A self-organizing multilayered neural network”. In : *Biological cybernetics* 20.3 (1975), p. 121-136.

[Fur+14] Steve B Furber et al. “The spinnaker project”. In : *Proceedings of the IEEE* 102.5 (2014), p. 652-665.

[Geo+96] Antoine Georges et al. “Dynamical mean-field theory of strongly correlated fermion systems and the limit of infinite dimensions”. In : *Reviews of Modern Physics* 68.1 (1996), p. 13.

[Ger+14] Wulfram GERSTNER et al. *Neuronal dynamics : From single neurons to networks and models of cognition*. Cambridge University Press, 2014.

[GRR09] Gokul GOPALAKRISHNAN, Dmitry RUZMETOV et Shriram RAMANATHAN. "On the triggering mechanism for the metal–insulator transition in thin film VO 2 devices : electric field versus thermal effects". In : *Journal of Materials Science* 44.19 (2009), p. 5345-5353.

[Gué+13] S GUÉNON et al. "Electrical breakdown in a V2O3 device at the insulator-to-metal transition". In : *EPL (Europhysics Letters)* 101.5 (2013), p. 57003.

[Gui+13] Vincent GUIOT et al. "Avalanche breakdown in GaTa 4 Se 8- x Te x narrow-gap Mott insulators". In : *Nature Communications* 4.1 (2013), p. 1-6.

[Hoe16] Bernd HOEFFLINGER. "ITRS 2028—International roadmap of semiconductors". In : *CHIPS 2020 VOL. 2*. Springer, 2016, p. 143-148.

[Hop82] John J HOPFIELD. "Neural networks and physical systems with emergent collective computational abilities". In : *Proceedings of the national academy of sciences* 79.8 (1982), p. 2554-2558.

[Hop88] John J HOPFIELD. "Artificial neural networks". In : *IEEE Circuits and Devices Magazine* 4.5 (1988), p. 3-10.

[Hsi+14] Wen-Pin HSIEH et al. "Evidence for photo-induced monoclinic metallic VO2 under high pressure". In : *Applied Physics Letters* 104.2 (2014), p. 021917.

[IFT98] Masatoshi IMADA, Atsushi FUJIMORI et Yoshinori TOKURA. "Metal-insulator transitions". In : *Reviews of modern physics* 70.4 (1998), p. 1039.

[Ind03] Giacomo INDIVERI. "A low-power adaptive integrate-and-fire neuron circuit". In : *Proceedings of the 2003 International Symposium on Circuits and Systems, 2003. ISCAS'03.* T. 4. IEEE. 2003, p. IV-IV.

[Jan+15] Etienne JANOD et al. "Resistive switching in Mott insulators and correlated systems". In : *Advanced Functional Materials* 25.40 (2015), p. 6287-6305.

[Jol+06] Renaud JOLIVET et al. "Predicting spike timing of neocortical pyramidal neurons by simple threshold models". In : *Journal of Computational Neuroscience* 21.1 (2006), p. 35-49.

[Kal+20] Yoav KALCHEIM et al. "Non-thermal resistive switching in Mott insulator nanowires". In : *Nature Communications* 11.1 (2020), p. 1-9.

[Kim+04] Hyun-Tak KIM et al. "Mechanism and observation of Mott transition in VO2-based two-and three-terminal devices". In : *New Journal of Physics* 6.1 (2004), p. 52.

[Kim+10] Jeehoon KIM et al. "Nanoscale imaging and control of resistance switching in VO 2 at room temperature". In : *Applied Physics Letters* 96.21 (2010), p. 213106.

[Kro08] Anders KROGH. "What are artificial neural networks ?" In : *Nature biotechnology* 26.2 (2008), p. 195-197.

[KSH12] Alex KRIZHEVSKY, Ilya SUTSKEVER et Geoffrey E HINTON. "Imagenet classification with deep convolutional neural networks". In : *Advances in neural information processing systems* 25 (2012).

[KSW17] Suhas KUMAR, John Paul STRACHAN et R Stanley WILLIAMS. "Chaotic dynamics in nanoscale NbO2 Mott memristors for analogue computing". In : *Nature* 548.7667 (2017), p. 318-321.

[Lee+18] D LEE et al. "Isostructural metal-insulator transition in VO2". In : *Science* 362.6418 (2018), p. 1037-1040.

[Lee+21] Dong Kyu LEE et al. "Heterogeneous integration of single-crystalline rutile nanomembranes with steep phase transition on silicon substrates". In : *Nature communications* 12.1 (2021), p. 1-8.

[Li+17] Jiajun LI et al. "Microscopic theory of resistive switching in ordered insulators : Electronic versus thermal mechanisms". In : *Nano letters* 17.5 (2017), p. 2994-2998.

[Maa94] Wolfgang MAASS. "On the computational complexity of networks of spiking neurons". In : *Advances in neural information processing systems* 7 (1994).

[Maa97] Wolfgang MAASS. "Networks of spiking neurons : the third generation of neural network models". In : *Neural networks* 10.9 (1997), p. 1659-1671.

[Mal+20] Antik MALLICK et al. "Using synchronized oscillators to compute the maximum independent set". In : *Nature communications* 11.1 (2020), p. 1-7.

[Mea90] Carver MEAD. "Neuromorphic electronic systems". In : *Proceedings of the IEEE* 78.10 (1990), p. 1629-1636.

[Med97] Maria Luisa MEDARDE. "Structural, magnetic and electronic properties of perovskites (R= rare earth)". In : *Journal of Physics : Condensed Matter* 9.8 (1997), p. 1679.

[Mer+14] Paul A Merolla et al. "A million spiking-neuron integrated circuit with a scalable communication network and interface". In : *Science* 345.6197 (2014), p. 668-673.

[MI89] Carver Mead et Mohammed Ismail. *Analog VLSI implementation of neural systems*. T. 80. Springer Science & Business Media, 1989.

[MM88] Carver A Mead et Misha A Mahowald. "A silicon model of early visual processing". In : *Neural networks* 1.1 (1988), p. 91-97.

[Mol+10] Daniel Molka et al. "Characterizing the energy consumption of data transfers and arithmetic operations on x86- 64 processors". In : *International conference on green computing*. IEEE. 2010, p. 123-133.

[Moo95] Gordon E Moore. "Lithography and the future of Moore's law". In : *Integrated Circuit Metrology, Inspection, and Process Control IX*. T. 2439. SPIE. 1995, p. 2-17.

[MP17] Marvin Minsky et Seymour A Papert. *Perceptrons, Reissue of the 1988 Expanded Edition with a new foreword by Léon Bottou : An Introduction to Computational Geometry*. MIT press, 2017.

[MP43] Warren S McCulloch et Walter Pitts. "A logical calculus of the ideas immanent in nervous activity". In : *The bulletin of mathematical biophysics* 5.4 (1943), p. 115-133.

[MS95] Zachary F Mainen et Terrence J Sejnowski. "Reliability of spike timing in neocortical neurons". In : *Science* 268.5216 (1995), p. 1503-1506.

[Mue+05] W Mueller et al. "Challenges for the DRAM cell scaling to 40nm". In : *IEEE InternationalElectron Devices Meeting, 2005. IEDM Technical Digest*. IEEE. 2005, 4-pp.

[MW11] Mark D McDonnell et Lawrence M Ward. "The benefits of noise in neural systems : bridging theory and experiment". In : *Nature Reviews Neuroscience* 12.7 (2011), p. 415-425.

[Par15] Sung-Kye Park. "Technology scaling challenge and future prospects of DRAM and NAND flash memory". In : *2015 IEEE International Memory Workshop (IMW)*. IEEE. 2015, p. 1-4.

[Peh+22] Christian Pehle et al. "The BrainScaleS-2 Accelerated Neuromorphic System With Hybrid Plasticity". In : *Frontiers in Neuroscience* 16 (2022). issn : 1662-453X. doi : 10.3389/fnins.2022.795876.

[Pey+12] Adrien Peyrache et al. "Spatiotemporal dynamics of neocortical excitation and inhibition during human sleep". In : *Proceedings of the national academy of sciences* 109.5 (2012), p. 1731-1736.

[PG00] Hans E Plesser et Wulfram Gerstner. "Noise in integrate-and-fire neurons : from stochastic input to escape rates". In : *Neural Computation* 12.2 (2000), p. 367-384.

[PMW13] Matthew D Pickett, Gilberto Medeiros-Ribeiro et R Stanley Williams. "A scalable neuristor built with Mott memristors". In : *Nature materials* 12.2 (2013), p. 114-117.

[Qiu+] E Qiu et al. "Stochasticity in the synchronization of strongly coupled spiking oscillators". In : *forthcoming* ().

[RJP19] Kaushik Roy, Akhilesh Jaiswal et Priyadarshini Panda. "Towards spike-based machine intelligence with neuromorphic computing". In : *Nature* 575.7784 (2019), p. 607-617.

[Roc+22] Rodolfo Rocco et al. "Exponential Escape Rate of Filamentary Incubation in Mott Spiking Neurons". In : *Physical Review Applied* 17.2 (2022), p. 024028.

[Ros58] Frank Rosenblatt. "The perceptron : a probabilistic model for information storage and organization in the brain." In : *Psychological review* 65.6 (1958), p. 386.

[Roz97] Marcelo J Rozenberg. "Integer-filling metal-insulator transitions in the degenerate Hubbard model". In : *Physical Review B* 55.8 (1997), R4855.

[Sei04] Udo Seiffert. "Artificial neural networks on massively parallel computer hardware". In : *Neurocomputing* 57 (2004), p. 135-150.

[SG05] Alfons Schnitzler et Joachim Gross. "Normal and pathological oscillatory communication in the brain". In : *Nature reviews neuroscience* 6.4 (2005), p. 285-296.

[SGJ05] Richard B Stein, E Roderich Gossen et Kelvin E Jones. "Neuronal variability : noise or part of the signal ?" In : *Nature Reviews Neuroscience* 6.5 (2005), p. 389-397.

[SPS00] G Stefanovich, A Pergament et D Stefanovich. "Electrical switching and Mott transition in VO2". In : *Journal of Physics : Condensed Matter* 12.41 (2000), p. 8837.

[Sto+13] Pablo Stoliar et al. "Universal Electric-Field-Driven Resistive Transition in Narrow-Gap Mott Insulators". In : *Advanced materials* 25.23 (2013), p. 3222-3226.

[Sto+14] P Stoliar et al. "Nonthermal and purely electronic resistive switching in a Mott memory". In : *Physical Review B* 90.4 (2014), p. 045146.

[Sto+17] Pablo Stoliar et al. "A leaky-integrate-and-fire neuron analog realized with a Mott insulator". In : *Advanced Functional Materials* 27.11 (2017), p. 1604740.

[Str+08] Dmitri B Strukov et al. "The missing memristor found". In : *nature* 453.7191 (2008), p. 80-83.

[SWB03] VA Sidorov, A Waśkowska et D Badurski. "V3O5 at high pressure : a possible heavy fermion 3d-metal oxide". In : *Solid state communications* 125.7-8 (2003), p. 359-363.

[Tes+18] Federico Tesler et al. "Relaxation of a Spiking Mott Artificial Neuron". In : *Physical Review Applied* 10.5 (2018), p. 054001.

[Tha+18] Chetan Singh Thakur et al. "Large-scale neuromorphic spiking array processors : A quest to mimic the brain". In : *Frontiers In Neuroscience* 12 (2018), p. 891.

[Tor+92] JB Torrance et al. "Systematic study of insulator-metal transitions in perovskites R NiO 3 (R= Pr, Nd, Sm, Eu) due to closing of charge-transfer gap". In : *Physical Review B* 45.14 (1992), p. 8209.

[Tur48] Alan Mathison Turing. *Intelligent machinery*. 1948.

[Val+18] I Valmianski et al. "Origin of the current-driven breakdown in vanadium oxides : thermal versus electronic". In : *Physical Review B* 98.19 (2018), p. 195144.

[Val+19] Javier del Valle et al. "Subthreshold firing in Mott nanodevices". In : *Nature* 569.7756 (2019), p. 388-392.

[Val+21] Javier del Valle et al. "Dynamics of the electrically induced insulator-to-metal transition in rare-earth nickelates". In : *Physical Review B* 104.16 (2021), p. 165141.

[Von93] John Von Neumann. "First Draft of a Report on the EDVAC". In : *IEEE Annals of the History of Computing* 15.4 (1993), p. 27-75.

[Wan+20] Zhongrui Wang et al. "Resistive switching materials for information processing". In : *Nature Reviews Materials* 5.3 (2020), p. 173-195.

[War03] Lawrence M Ward. "Synchronous neural oscillations and cognitive processes". In : *Trends in cognitive sciences* 7.12 (2003), p. 553-559.

[WD08] Jayawan HB Wijekoon et Piotr Dudek. "Compact silicon neuron circuit with spiking and bursting behaviour". In : *Neural Networks* 21.2-3 (2008), p. 524-534.

[Yao+20] Peng Yao et al. "Fully hardware-implemented memristor convolutional neural network". In : *Nature* 577.7792 (2020), p. 641-646.

[Zim+13] A Zimmers et al. “Role of thermal heating on the voltage induced insulator-metal transition in VO 2”. In : *Physical Review Letters* 110.5 (2013), p. 056601.

Acronymes

ANN Artificial Neural Network. 17, 19

CCD Charged-Coupled Device. 75, 77

CMOS Complementary Metal Oxide Semiconductor. 13, 14, 16, 71, 90, 111

CPU Central Processing Unit. 19, 20

DMFT Dynamical Mean Field Theory. 20–22

DOS Density of States. 21, 22

EEG Electro Enecephalo Graph. 15, 71, 72

IMT Insulator to Metal Transition. 13, 14, 20, 22, 23, 27, 69, 73, 85, 112

ISI Inter Spike Intervals. 16, 96, 97, 99, 100, 104, 106–108

KCL Kirchhoff Current Law. 78, 91

KVL Kirchhoff Voltage Law. 27, 30, 78, 80, 93, 94

MRN Mott Resistor Network. 14, 15, 24, 25, 27, 37, 51–53, 59, 65, 71, 73–76, 78, 79, 81, 82, 85, 88, 90, 112, 113

NdNiO3 Neodymium Nickelate. 15, 52, 59, 60, 63, 65, 66, 68, 69, 112, 113

SmNiO3 Samarium Nickelate. 15, 52, 59, 60, 63, 65, 67–69, 112, 113

V2O3 Divanadium Trioxide. 15, 22, 23, 25–27, 37, 51–54, 56, 59, 63, 65, 73, 111–113

V3O5 Trivanadium Pentoxide. 3, 15, 16, 23, 25, 26, 71–73, 75, 77, 85, 87–89, 113

VO2 Vanadium Dioxide. 3, 15, 16, 22–27, 37, 51–54, 56–59, 63, 65, 73, 89, 90, 96–98, 100, 103, 104, 106–108, 111–113

université PARIS-SACLAY | ÉCOLE DOCTORALE Physique en Île-de-France (PIF)

Titre : Propriétés neuromorphiques des materiaux de Mott sous un champ électrique
Mots clés : Materiaux de Mott, systèmes neuromorphiques, collapse de la résistance

Résumé : Les isolants de Mott sous un champ électrique externe présentent une transition isolant-métal (IMT) qui leur permet de reproduire le train de «spikes» des neurones biologiques. Ces matériaux ont aussi la possibilité d'achever un niveau de miniaturisation supérieur à celui des dispositives CMOS, et donc ils pourraient être utilisé pour réaliser des réseaux des neurones numérique plus efficients. Néanmoins, la IMT est un phénomène physique complexe qui dérive de l'interaction entre beaucoup d'électrons sous un fort champ électrique et il pose des difficultés importantes concernant la description théorique de ces matériaux. Dans cette thèse nous adoptons un modèle mésoscopique et phénoménologique qui s'appelle Réseau des Résistors de Mott (MRN). Grâce à ce model nous sommes capable d'expliquer la nature de la IMT sous un champ électrique, qui est le produit des effets et thermique et électronique, et plus précisément l'effet Joule et la concentration de courent électronique dans les domaines métalliques du matériel. Nous identifions le collapse de la résistance du matériel comme un process stochastique, et plus précisément un évènement de Poisson, en analogie avec les «spikes» des modelés mathématiques des neurones avec une probabilité de type exponentielle. Nous démontrons aussi que la nature stochastique de la chute de la résistance, qui est observé dans la variabilité de délais entre l'application du champ électrique et le collapse de la résistance, peut être changée par la conductivité thermique du matériel et aussi le rapport entre la résistivité isolant et la résistivité métallique. En outre, nous étudions les oscillations qui émergent sous hauts champs électriques, et aussi la dynamique des matériaux VO2 couplés, en particulier les interruptions de la séquence régulier de spikes produits par une haute capacité électrique de couplage. Nous comparons nos résultats avec des expérimentes conduites sur les vanadates et les nickélates, en trouvant un très bon accord.

Title : Neuromorphic properties of Mott materials under an electric field
Keywords : Mott materials, neuromorphic systems, resistive switching

Abstract : Mott insulators under an applied electric field present an insulator-to-metal transition that enables them to reproduce the spiking functionality of biological neuron. These materials also have the potential of achieving greater miniaturization than conventional CMOS devices and thus could be used to create energy efficient hardware neural networks. However, the understanding of the IMT, which is a complex physical phenomenon that stems from the interaction of many correlated electrons under strong electric fields, poses important challenges to the characterization of these materials. In this work we adopt a mesoscopic phenomenological model known as the Mott Resistor Network. In so doing we are able to elucidate the nature of the field driven IMT, to which both thermal and electronic effects contribute, in the form of Joule heating and current density concentration, respectively. We characterize the resistive collapse as a stochastic process, and more exactly a Poissonian event, in analogy with the firing of noisy neurons described by the exponential escape rate model. We show how the stochastic nature of the resistive collapse, which is observed in the increased variability of the incubation times as the applied voltage is lowered, can be tuned by controlling the thermal conductivity of the sample and also the ratio of the insulating to metallic resistivity. We then study the oscillatory regime that appears at high applied voltage, as well as the dynamics of coupled VO2 oscillators, focusing on the disruptions of the regular spiking sequence that emerge as the coupling capacitance is strengthened. We compare our results with experiments conducted on vanadates and nickleates, finding an excellent agreement.